This document is downloaded from DR-NTU (https://dr.ntu.edu.sg)
Nanyang Technological University, Singapore.

Low temperature micro solid oxide fuel cells with proton-conducting ceramic electrolytes

Li, Yong

2016

Li, Y. (2016). Low temperature micro solid oxide fuel cells with proton-conducting ceramic electrolytes. Doctoral thesis, Nanyang Technological University, Singapore.

https://hdl.handle.net/10356/67012

https://doi.org/10.32657/10356/67012

Downloaded on 13 Mar 2024 16:27:22 SGT

Low Temperature Micro Solid Oxide Fuel Cells with Proton-conducting Ceramic Electrolytes

LI YONG

School of Mechanical and Aerospace Engineering

A thesis submitted to the Nanyang Technological University
in partial fulfilment of the requirements for the degree of
Doctor of Philosophy

2016

“ A lot of my research time is spent daydreaming - telling an imaginary admiring audience of laymen how to understand some difficult scientific idea.”

— Leonard Susskind

Acknowledgements

I would like to express my most sincere appreciation and gratitude to my supervisor, Prof. Su Pei-Chen, for her considerate guidance, patience and encouragement all throughout this PhD project. More than a supervisor, it is her personality, lifestyle, and working philosophy that inspire me all through this four-year wonderful journey.

I would like to extend my sincere appreciation to my co-supervisor Prof. Wang Shijie for his valuable advice and enlightenments. I also owe sincere appreciation to Prof. Chan Siew Hwa for his inspiring discussions and generous help in this work.

Special thanks go to my fellow group members: Baek Jong Dae, Xie Hanlin, Yu Chen-Chiang, Ng Chee Seng, Liu Kang Yu, Tan Hong Yi Kenneth, Choong Yu Ying Clarrisa, and Lee Tsung Han for the sleepless nights we were working together before deadlines, and for all the fun we have had in NTU.

I also wish to acknowledge Dr. Nancy Wong Lai Mun, Dr. Chai Jianwei, Mr. Wong Ten It in IMRE, Dr. Huang Huancong, Dr. Fan Liangdong, Dr. Mridula Biswas, Dr. Ha Sean Seungbum, Dr. Liu Qinglin in NTU, and all the staffs and technicians in Fuel Cell Laboratory (ERI@N), Materials Laboratory 1, and Micromachines Lab 1 for their assistance, knowledge sharing and helpful comments.

My sincere thanks also extend to Dr. Yan Xihong, Dr. Wang Zhiyong, Dr. Han Beibei, and Mr. Liu Ning for their encouragement and support.

Special thanks to Sun Wenjiao for her everlasting love and patience. Last but not least, I would like to thank my beloved family for their constant support, love and encouragement.

Contents

Acknowledgements **iii**

List of Figures **ix**

List of Tables **xiii**

Abstract **xv**

1 Introduction **1**
1.1 Overview 1
1.2 Research Motivation and Objectives 2
1.3 Thesis Outline 4

2 Literature Review **7**
2.1 Introduction 7
2.2 Solid Oxide Fuel Cells 9
2.2.1 Structure of SOFCs 9
2.2.2 Thermodynamic Principles 11
2.3 Low Temperature SOFCs 13
2.4 Thin Film SOFCs 15
2.5 Proton-conducting SOFCs 16
2.5.1 Proton-conducting Electrolyte 17
2.5.2 Proton-conducting SOFCs 20
2.6 Pulsed Laser Deposition 25
2.7 Chapter Summary 27

3 Nanoscale Doped Barium Cerate Electrolytes for Low Temperature SOFCs **29**
3.1 Introduction 29
3.2 Experimental Methods 32
3.2.1 Fabrication and Test of BCY μ-SOFCs 32
3.2.2 Electrolyte Characterizations 34
3.3 Chemical stability study of BCY electrolytes 34
3.3.1 Electrochemical Performance of BCY Cells 34

3.3.2 Microstructural Characterization 36
3.3.3 XPS Study of the Chemical Stability of BCY 38
3.4 Chemical Stable BCZY-based μ-SOFCs 47
3.5 Chapter Summary 50

4 Proton-conducting SOFCs with Improved Cathode Reactions by a Nanoscale GDC Interlayer 53
4.1 Introduction 53
4.2 Experimental Methods 58
4.2.1 Electrolyte Deposition and Fuel Cell Fabrication 58
4.2.2 Crystallinity and Morphology Characterization 59
4.2.3 Fuel Cell Performance Characterization 60
4.3 Results and Discussion 60
4.3.1 Microstructure of the GDC/BZY Electrolyte 60
4.3.2 Electrochemical Characterization 64
4.4 Chapter Summary 71

5 Nanostructured $Ba_{0.5}Sr_{0.5}Co_{0.8}Fe_{0.2}O_{3-\delta}$ (BSCF) Thin Film Cathode for Low Temperature SOFCs 73
5.1 Introduction 73
5.2 Experimental Methods 76
5.2.1 Deposition of BSCF Thin Film 76
5.2.2 Thin Film Crystallinity and Morphology Characterization . 77
5.2.3 Thin Film SOFC Fabrication and Electrochemical Characterization 78
5.3 Results and Discussion 79
5.3.1 Crystallinity and Morphologies of BSCF Thin Films 79
5.3.2 Electrochemical Characterization of Dense and Nanostructured BSCF Cathodes 83
5.3.3 Performance of μ-SOFCs using BSCF Cathodes 85
5.3.4 Chemical Stability of BSCF Thin Film 87
5.4 Chapter Summary 87

6 Conclusion 91
6.1 Summary and Contributions 91
6.2 Suggested Future Work 93

A μ-SOFC Fabrication and Characterization 97
A.1 Fuel Cell Fabrication 97
A.2 μ-SOFC Characterization 99

B Nanoporous Palladium Anode for Direct Ethanol SOFCs with Nanoscale Proton-conducting Ceramic Electrolyte 101
B.1 Introduction 101

B.2 Experimental Methods 104
B.2.1 Thin Film Deposition 104
B.2.2 Fuel Cell Fabrication and Test 105
B.2.3 Material Characterization 106
B.3 Results and Discussion 107
B.3.1 Thin Film Characterization 107
B.3.2 Electrochemical Characterization of μ-SOFC with Pd anode 110
B.4 Summary 114

Bibliography **117**

Publication **128**

List of Figures

2.1 Schematic of cross-section of a SOFC with (a) proton-conducting electrolyte [1] and (b) oxygen ion conducting electrolyte [2]. 10
2.2 Schematic of current-voltage characteristics of a SOFC. 12
2.3 Schematic drawing of a free-standing SOFC (a) and an thin film SOFC membrane on a porous substrate (b) [3]. 15
2.4 Two presentive traces of proton conduction in perovskite lattice: rotational diffusion and proton transfer [4]. 17
2.5 Comparison of the arrhenius conductivities of sintered proton-conducting pellets (BZY, BCY) with the current high performing oxygen-ion conductors, SDC, LSGMs, and YSZ [5, 6]. 19
2.6 Arrhenius plots of the proton conductivity of highly-textured BZY film grown on MgO substrate, BZY sintered pellets with varied grain size from 1 μm down to several hundred nanometers [6]. . . . 20
2.7 Schematic view of a PLD system [7] 26

3.1 Structure of free-standing μ-SOFC device. (a) Schematic of cell structure; (b) Optical microscopy image of SOFC seen from cathode side; (c) SEM image of SOFC seen from anode side. 33
3.2 Polarization curves at temperatures of 300, 350, and 400 °C. 35
3.3 Cross-sectional FE-SEM images of the BCY electrolyte before (a) and after fuel cell test at 400 °C (b). The inset figure in (a) shows a magnificent view of the porous Pt surface. 36
3.4 GIXRD patterns of BCY electrolyte before and after fuel cell test at 400 °C. 37
3.5 XPS spectra of Ba 3d for the BCY electrolyte before (top) and after fuel cell tested at 300 (middle) and 400 °C. (bottom). The original data, fitted spectra and Shirley background are shown in hollow points, colored solid lines and dotted line, respectively. 40
3.6 XPS spectra of O 1s for the BCY electrolyte before (top) and after fuel cell tested at 300 (middle) and 400 °C. (bottom). The original data, fitted spectra and Shirley background are shown in hollow points, colored solid lines and dotted line, respectively. 41
3.7 XPS spectra of C 1s for the BCY electrolyte before (top) and after fuel cell tested at 300 (middle) and 400 °C. (bottom). The original data, fitted spectra and Shirley background are shown in hollow points, colored solid lines and dotted line, respectively. 42

3.8 XPS spectra of Ce 3d for the BCY electrolyte before and after fuel cell test at 400 °C. 45
3.9 FE-SEM image of cross-sectional view of a proton-conducting μ-SOFC with BCZY electrolyte. 49
3.10 I-V-P curve of SOFC with BCZY electrolyte tested with H_2 at different temperature of 300, 350, and 400 °C. 50
3.11 XRD patterns of BCZY electrolyte before and after fuel cell test at 400 °C. 51

4.1 Schematics of μ-H-SOFCs with possible oxygen reduction reaction and water evolution reaction zone at the cathode/electrolyte interface. (a) The cell with platinum cathode in contact directly with BZY electrolyte, and (b) the cell with platinum cathode in contact with the GDC interlayer on top of the BZY electrolyte. 56
4.2 XRD patterns of BZY thin film electrolytes (a) with and (b) without GDC interlayer, with the reference peaks indices for BZY and GDC in (c). 61
4.3 FESEM cross-sectional images of the free-standing electrolyte membranes with platinum cathode and anode. (a) BZY electrolyte; (b) BZY electrolyte with GDC cathodic interlayer, and (c) magnification of (b). 63
4.4 Cross-sectional TEM characterizations near the Pt/GDC-interlayer/BZY-electrolyte at the non-freestanding region of the membrane on a SiN/Si substrate. (a)Cross-sectional view of the heterostructure of Pt/GDC/BZY/SiN; (b) High resolution TEM image of the GDC interlayer and interface. The GDC/BZY interface and grain boundaries are indicated by dashed lines; (c) A high density of dislocations is observed in the GDC interlayer, with some of them marked by the labels "⊥"; (d) The corresponding inverse FFT calculated image of the dotted region in (c). The dashed lines are guides indicating the dislocation lines and the existence of lattice distortion. 64
4.5 I-V curves of the μ-H-SOFCs (a) with only BZY electrolyte, and (b) with BZY electrolyte with GDC interlayer at 350 to 425 °C. . . 66
4.6 The Nyquist plots of EIS characterizations of μ-H-SOFCs with (a) BZY electrolyte only, (b) BZY electrolyte with GDC interlayer, and (c) bode plots for both cells. 67

5.1 XRD patterns of BSCF deposited at various (a) substrate temperature and (b) oxygen partial pressures. 79
5.2 FESEM surface morphological characterizations of BSCF thin films deposited at oxygen partial pressure of (a) 1 Pa, (b) 10 Pa, (c) 20 Pa, and (d) 50 Pa. The insets are AFM images of each samples obtained at tapping mode. (e) The RMS roughness and average particle size calculated based on AFM images in (a)-(d). 81
5.3 (a) TEM image of the cross-sectional view of BSCF thin film deposited at oxygen partial pressure of 20 Pa; (b) High-resolution TEM image of BSCF thin film. 82

5.4 (a) Cell voltages and power densities as function of current density of YSZ electrolyte supported cells with (a) dense, (b) nanostructured BSCF thin film cathodes and (c). nanoporous Pt cathode; (d) typical Nyquist impedance curves for the dense BSCF and nanostructured BSCF cathodes tested at 500°C. 84
5.5 Cross-sectional FESEM characterizations of μ-SOFC with (a) dense BSCF thin film cathode deposited at 1 Pa and (b) nanostructured BSCF thin film cathode deposited at 20 Pa. (c) and (d) shows the corresponding surface morphologies of BSCF cathode films in (a) and (b) after fuel cell test. 86
5.6 Cell voltages and power densities as function of current density of free-standing BZY electrolyte supported cells with (a) dense and (b) nanostrucutred BSCF thin film tested with H_2 fuel at temperatures of 425, and 450 °C. 88
5.7 XPS spectra of (a) Fe 2p and (b) Sr 3d, Ba 4d and Co 3p for the nanostrucutred BSCF thin film cathode before and after fuel cell test. 89

6.1 (a) Current Si_3N_4 supported μ-SOFC structure and (b) proposed epitaxial BZY μ-SOFC. 94

A.1 Fabrication flow of thin film free-standing square electrolyte μ-SOFC. 98
A.2 μ-SOFC test station: (a) schematic picture; (b) optical image of customized test setup. 100

B.1 Schematic of (a) switchable ethanol fuel feeding system and (b) custom-designed μ-SOFC test station. 106
B.2 XRD patterns of PLD films deposited at various substrate temperatures. Bare Si_3N_4 substrate together with reference peaks for BZY (PDF No. 96-720-2180) are included for comparison. 108
B.3 FESEM surface characterization of Pd thin film sputtered at Ar pressure of (a) 3 and (b) 80 mTorr. 109
B.4 XRD patterns with reference peaks for fcc-Pd (PDF No. 00-046-1043) of Pd thin film deposited at Ar pressure of 3 and 80 mTorr. . 110
B.5 I-V-P performances of μ-SOFC consisting of Pd anode test with (a) dry hydrogen fuel and (b) ethanol fuel at 350 and 400 °C; (c) OCV evolution for dry hydrogen and ethanol fuel testing after temperature stabilization at temperature of 350 and 400 °C;. 112
B.6 FESEM characterization of Pt/BZY/Pd μ-SOFC after fuel cell test. (a) Cross-sectional view of Pt/BZY/Pd heterostructure after testing with hydrogen; (b) Pd anode morphology after hydrogen fuel test; (c) Pd anode morphology after ethanol fuel test; (d) Enlarged view of Pd anode in the free-standing membrane region of (c) 114
B.7 High resolution XPS spectra of C 1s recorded from Pd anode. (a) as deposited; (b) after fuel cell test with H_2 fuel; and (c) after fuel cell test with ethanol fuel. 115

List of Tables

2.1 Summary of μ-SOFCs performances with protonic ceramic electrolytes reported in the literature. 24

3.1 Crystal structure and parameters obtained by XRD refinement . . . 38
3.2 Fitted curves and calculated concentration of the characteristic XPS lines for Ce^{4+} and Ce^{3+}. 46
3.3 Summary of BCZY SOFC performance 48

4.1 Summary of the values extracted from equivalent circuit fitting of the EIS curves at 350, 375, and 400 °C. 68

Abstract

Solid oxide fuel cells (SOFCs) are highly efficient energy conversion devices which can convert chemical energy directly into electricity without combustion. The major hurdle to SOFCs is the requirement of high operating temperature (>800 °C), which leads to a technological challenge for materials development and thermal management. Thus reducing the operating temperature of SOFCs to intermediate temperature (500-800 °C) range or even low temperature range (<500 °C) would greatly benefit the wide application of SOFC technology. Reducing the electrolyte thickness and/or utilizing proton-conducting electrolytes are two efficient approaches to reduce the operating temperature of SOFCs, as well as maintain high output power density. This work is dedicated to achieve high performance SOFCs at low operating temperature of 300-500 °C by using micro-SOFCs (μ-SOFCs) with proton-conducting thin film electrolytes.

First, the chemical stability of nanoscale Y-$BaCeO_3$ (BCY) proton-conducting electrolyte under μ-SOFCs operating environments is investigated. BCY-based SOFC shows a maximum power density of 30 mW/cm^2 and an OCV of 0.59 V at 400 °C. The OCV decreases dramatically as testing temperature increases. The low OCV value and poor fuel cell performance originated from the cracks formed during test. Y-$BaCeZrO_3$ (BCZY) electrolyte is employed to enhance the chemical stability and performance of cerium-based ceramic electrolytes. Both the OCV and fuel cell performance of BCZY-based SOFC have great improvement compared with BCY SOFC. The maximum power density has increased to 89 mW/cm^2 at 400 °C, which is nearly 3 times that of BCY-based SOFC. The OCV was maintained at around 1.0 V, showing that BCZY is a promising electrolyte candidate with essential ionic conductivity and chemical stability for low temperature SOFC application.

In order to enhance the sluggish cathodic oxygen reduction reaction (ORR) at low temperature, a cathodic modification method was introduced. High performance μ-SOFC using chemical stable Y-$BaZrO_3$ (BZY) electrolyte was obtained

by utilizing an 8 nm thin film GDC cathode interlayer. The cathodic polarization resistance was effectively reduced by the additional GDC interlayer between the Pt cathode and BZY electrolyte. A high peak power density of 445 mW/cm^2 was obtained at 425 °C from the μ-SOFC with the GDC cathodic interlayer. The mixed oxygen and proton conduction in the GDC interlayer has expanded the ORR sites from a 2-dimentional planar interface between Pt and BZY to the entire GDC interlayer.

The cathodic modification was further investigated by incorporating nanostructured $Ba_{0.5}Sr_{0.5}Co_{0.8}Fe_{0.2}O_{3-\delta}$ (BSCF) thin film cathode into μ-SOFCs. The nanostructured BSCF thin film has increased total surface area exposed to oxygen reactions compared to the previously reported dense BSCF thin film cathode, which rendered significantly enhanced cathode performances in improving the sluggish oxygen reduction reactions. μ-SOFCs using the nanostructured BSCF cathode achieved a fuel cell performance with a peak power density of 55 mW/cm^2 at 450 °C.

Finally, we explored the feasibility of direct operation of ethanol fuel with μ-SOFC at low temperature (<500 °C). μ-SOFC with highly crystallized BZY thin film electrolyte, nanoporous Pd anode and Pt cathode exhibits a peak power density of 72.4 and 15.3 mW/cm^2 with the fuels of hydrogen and ethanol at operating temperature of 400 °C.

Chapter 1

Introduction

1.1 Overview

This dissertation is mainly focus on the development of micro solid oxide fuel cells (μ-SOFCs) with thin film electrolytes to achieve high performance SOFCs at low operating temperature range (<500 °C), with an emphasis on the utilization of nanoscale proton-conducting ceramic electrolytes. The high fuel cell performance was achieved by combination of nanoscale proton-conducting electrolyte with high ionic conductivity and cathodic modification to enhance oxygen reduction reaction (ORR).

The main contribution of this dissertation are: (1) the chemical stability of thin film proton-conducting electrolytes is studied to understand the feasibility for μ-SOFC application; (2) cathodic modification methods were introduced to enhance fuel cell performance of μ-SOFC with proton-conducting ceramic electrolyte at low

temperature; (3) the promising application of μ-SOFCs as portable power sources are demonstrated with liquid alcohol fuels.

1.2 Research Motivation and Objectives

Yttria-stabilized zirconia (YSZ) is one of the most commonly used ceramic electrolytes for SOFCs due to its pure oxygen-ionic conduction and stability in operating environments [8]. However, the major hurdle to conventional SOFCs is the high operating temperature (>800 °C). The high operating temperatures pose a considerable technological challenge for materials development and thermal management. Thus reducing the operating temperature of SOFCs to intermediate temperature (500-800 °C) range or even low temperature range (<500 °C) would greatly benefit the widely application of SOFC technology.

One way to reduce the operating temperatures is to change or modify the electrolyte. A promising alternative is to use proton-conducting solid oxides that have a relatively high ionic conductivity of about 10^{-2} S/cm at the desired temperatures [9]. Compared to conventional oxygen ion conducting SOFCs with YSZ as the electrolyte layer, SOFCs with proton-conducting electrolytes are able to be run at much lower temperature. Currently, great attention and effort have been dedicated to the proton-conducting SOFC areas to explore materials with good chemical stability and higher ionic conductivity at lower operating temperature. Theoretical calculations and previous experimental works have shown that the benefits of water production on the cathode side and lower activation energy for

proton transportation, which make proton-conducting SOFCs potentially superior to oxygen-conducting SOFCs at low temperature range [9].

Another way to reduce the operating temperatures is to reduce the thickness of electrolyte layers, thus reducing electrolyte ohmic resistance. SOFCs have typically been applied to large, stationary application due to the high operating temperature and strictly materials selection. Nowadays, with the help of micro-fabrication techniques, SOFC may also be a promising technology for portable energy conversion application as thin film electrolyte and electrode can be fabricated [10]. Micro-fabricated nano-thin film SOFCs have been demonstrated that they can provide a power output larger than 1.0 W/cm^2 at 450 °C [11]. In addition to the small size and portability, a micro-fabricated SOFC has a number of advantages over the macro scale version, such as fast start-up time, low ohmic resistance, better ionic conductivity, etc.

The main objective of the dissertation is to develop and fabricate high performance micro-fabricated SOFCs with proton-conducting ceramic electrolytes working at low temperature range, addressing the primary disadvantage of conventional SOFC technology. In addition to this, fundamental understanding of the interrelationships between electrolyte structure, surface morphology and electrochemical properties will also be addressed. All these efforts and investigation are intended to reduce the operating temperature of SOFCs to low temperature range by reducing the electrolyte thickness to achieve high ionic conducting ceramic electrolytes, and enhancing the cathodic kinetics.

1.3 Thesis Outline

The dissertation is divided into following 6 chapters:

Chapter 2 provides a sufficient literature overview of SOFCs, including the structures, materials, thermodynamics. The state-of-the-art on the materials developments in SOFCs, with a particular focus on low temperature SOFCs with nanothin film elelctrolyte and high ionic conducting proton conductors are also reviewed.

Chapter 3 investigates the chemical stability of Ce-based proton-conducting electrolyte for thin film SOFCs application. The chemical unstable BCY electrolytes are systematically analyzed by structural and chemical composition characterizations. Furthermore, a chemical stable BCZY electrolyte was also incorporated into μ-SOFCs, which shows enhanced chemical stability and fuel cell performance compared to BCY electrolytes.

Chapter 4 demonstrates the concept of adding a doped ceria interlayer which is catalytically more active and is a mixed oxygen ionic and protonic conductor, to improve the chronically poor performance of μ-H-SOFCs. Significant enhancement of cathode performance and fuel cell power density in the silicon-based μ-H-SOFC was obtained with the addition of interlayer. The electrochemical impedance and fuel cell performance of the fabricated μ-H-SOFCs with and without the GDC interlayer was characterized to understand the effect of such cathode interlayer on the cathode kinetics behavior.

Chapter 5 presents the fabrication of a nanostructured BSCF thin film cathode by PLD. The deposition parameters such as oxygen partial pressure and substrate

temperatures are varied and optimized. The nanostructured BSCF thin film with higher porosity improved the oxygen gas transportation to increase active reaction sites for ORR. The functionality as a cathode at temperature below 500 °C was also characterized in fuel cell modes thin film proton-conducting μ-SOFCs.

Chapter 6 concludes this research work and provides possible future research directions related to μ-H-SOFCs.

The feasibility of operation of direct utilization of ethanol fuel for SOFC with proton-conducting ceramic electrolyte at the temperature range of 300-400 °C are also included in Appendix. Nanoporous Pd thin film is utilized as the anode catalyst toward ethanol oxidation reactions.

Chapter 2

Literature Review

2.1 Introduction

Since the early 2000s the demand for energy, especially from fossil fuels, and limits on the rate of fuel production has led to the energy crisis [12]. Most countries around the world are heavily relying on fossile energy. The ever-increasing consumption and decreased supply of these fuels will cause energy crisis for all countries around the world in the near future. When coal and natural gas are burned, greenhouse gases, such as nitrous oxides and carbon dioxide, are produced. Thus reducing atmospheric levels of greenhouse gases has arisen as an important goal for the entire resident on earth [13].

The demand for clean and renewable energy around the world has aroused great attention in the research field of clean energy alternatives [14]. One of these clean energy alternatives is the fuel cell. A fuel cell is a type of electrochemical

energy conversion device that converts fuel energy directly and efficiently into electrical energy without combustion. The main differences between various types of fuel cells are the fuels used, operating temperatures and the conducting ions. Currently, most fuel cells are utilizing polymer proton conducting electrolytes, i.e. polymer electrolyte membrane (PEM) fuel cells (PEMFC) due to the high ionic conductivity of polymer electrolyte and good manufacturability at low temperature range. Expensive catalysts such as platinum are often used in these fuel cells to enhance the catalytic activity towards fuel oxidation and oxygen reduction at room temperature. However, the high costs of these catalysts have hindered the commercialization and widely application of polymer fuel cells [15]. Excessive dependence of hydrogen fuel also limits the widely application as PEMFCs are susceptible to chemical attacks such as coking and sulfur poisoning when using hydrocarbon fuels [16].

In comparison, SOFC, which utilizes a layer of ion-conducting ceramic as the electrolyte, shows excellent chemical and thermal stability at different temperatures [17]. SOFCs also possess the advantage of fuel flexibilities because they can utilize a wide variety of fuels such as hydrocarbons, coal gas and gasified biomass with high efficient and cost-effective ways. The efficiency of chemical energy converting into electrical energy for SOFCs can reach as high as 60%, which is much higher than the combustion engine's 25% [18]. In addition, the produced thermal energy during SOFCs operation can also be used for the cell operation or other energy conversion devices to further increase the total efficiency as high as 75% [18]. Thus, SOFCs are expected to play a significant role in future energy conversion

technology.

2.2 Solid Oxide Fuel Cells

2.2.1 Structure of SOFCs

A SOFC is an electrochemical conversion device that convert fuels such as hydrogen and hydrocarbon into electricity directly without combustion [15]. Electrochemical reaction occurs between reactants (gaseous fuel) and oxidants (air). Typically, a SOFC is composed of three active components which are an electrolyte, an anode (a fuel electrode), and a cathode (an oxidant electrode) [17]. Figure 2.1 show schematic of fuel cell membrane electrode assembly (MEA) and illustrates the basic operational principle of fuel cells for proton and oxide ion conducting electrolytes. Fuel, such as hydrogen, or hydrocarbon fuel is supplied to the andoe side while at the cathode side, the oxidant such as oxygen gas is supplied.

During the operation process of SOFCs, the fuel is oxidized at the anode by the catalyst, while oxygen is catalytically reduced at the cathode. In these processes, electrons are produced and travel through the external circuit from anode side to cathode side to generate electricity. The electrolyte layer should be electrically insulating, but ionis such as oxygen ions or protons can travel though one side to

another side, where they can meet each other to complete the reaction and produce water. Take oxygen ion conducting SOFC for example, the electrochemical reactions occurring within the cell are:

Cathode: oxygen reduction reaction (ORR)

$$\frac{1}{2}O_2 + 2e^- \rightarrow O^{2-}. \tag{2.1}$$

Anode: hydrogen oxidation reaction (HOR)

$$H_2 \rightarrow 2H^+ + 2e^-. \tag{2.2}$$

Overall cell reaction

$$\frac{1}{2}O_2 + H_2 \rightarrow H_2O. \tag{2.3}$$

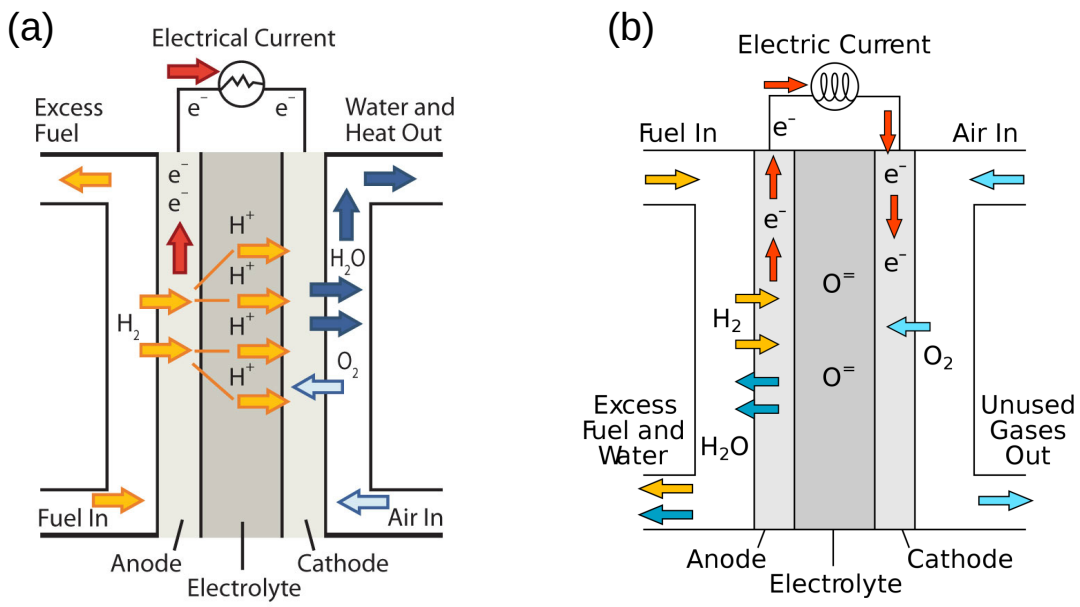

FIGURE 2.1: Schematic of cross-section of a SOFC with (a) proton-conducting electrolyte [1] and (b) oxygen ion conducting electrolyte [2].

2.2.2 Thermodynamic Principles

The maximum voltage which can be obtained for a given fuel cell can be determined by the chemical potential difference of the species. Chemical potential measures how the Gibbs free energy of a system changes when the system chemistry changes. Take hydrogen fuel cell for example, the theoretical value of the open-circuit voltage (OCV) is usually be expressed by:

$$E^0 = \frac{-\Delta\bar{g}_f}{2F}. \tag{2.4}$$

where $\Delta\bar{g}_f$ is Gibbs free energy, F is Faraday constant. The relationship between the ideal equilibrium potential (E) and the ideal potential (E^0) for the cell reaction at a different partial pressure of reactants and products are presented in the Nernst equation provided below:

$$E = E^0 + \frac{RT}{2F} \ln \frac{a_{H_2} \cdot a^{\frac{1}{2}O_2}}{a_{H_2O}}. \tag{2.5}$$

The cell voltage is related several parameters, such as partial pressure, temperature, etc. When reduce partial pressure of the products and increase the partial pressure of the reactants, the overall cell potential will increase. For instance, as the reactant pressures increases, the ideal cell voltage can also increase at given temperature for the hydrogen reaction.

In order to evaluate the fuel cell performance, a plot of current-voltage relationships is usually presented. This graph is a fuel cell polarization behavior curve,

or current-voltage (I-V) curve, showing the output voltage of a fuel cell at a given current density. A typical I-V curve of SOFCs working at low temperature range is shown in Figure 2.2. The maximum voltage is obtained by the difference between intrinsic chemical potentials (E_0) of the reactant and the oxidant. As the current is drawn from the cell, the output voltage starts to decrease from the reversible cell voltage. This drop of voltage represented the irreversible losses in a fuel cell operation.

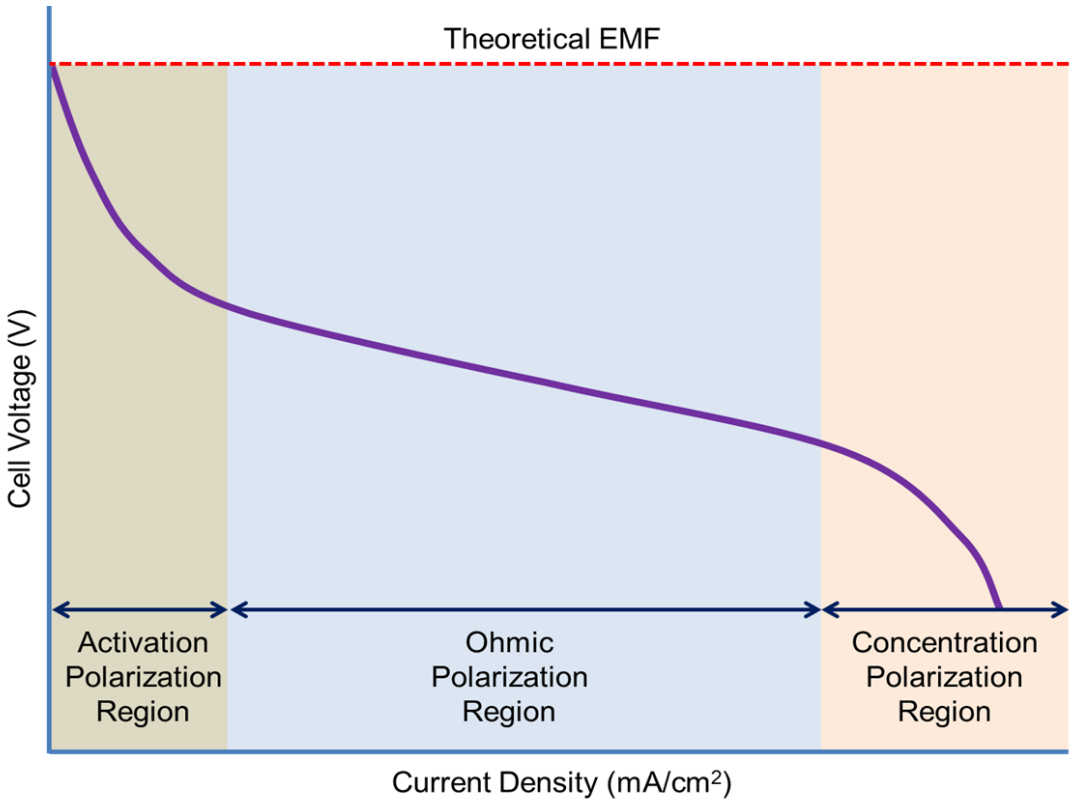

FIGURE 2.2: Schematic of current-voltage characteristics of a SOFC.

The real voltage output for a fuel cell is the reversible cell voltage minus the voltage drops due to these losses:

$$V = E_{thermo} - \eta_{act} - \eta_{ohmic} - \eta_{conc}. \tag{2.6}$$

where V is the actual voltage of fuel cell, E_{thermo} is the reversible thermodynamic voltage, η_{act} is the activation overpotential, η_{ohmic} is the ohmic overpotential, and η_{conc} is the concentration overpotential. The fuel cell characteristics can be determined by these three major types of fuel cell losses which form a I-V curve. As shown in Figure 2.2, the activation losses mostly affect the low current region of the curve. The ohmic losses are most apparent in the middle region of the curve and the concentration losses are significant when a fuel cell operated at high current region. The power density values can be calculated by simply multiplying the voltage and the current density values. The power density (P) values can be calculated by simply multiplying the voltage and the current density (i) as expressed in Equation 2.7.

$$P = i \times (E_{thermo} - \eta_{act} - \eta_{ohmic} - \eta_{conc}). \tag{2.7}$$

2.3 Low Temperature SOFCs

The main issues related to the reducing the operating temperatures of SOFCs are the increased electrolyte resistivity and sluggish electrode polarization kinetics with temperature decreases, which can be seen from Equation 2.7. The process related to ionic conduction in the electrolyte and electrochemical reactions for fuel oxidation or oxygen reduction are thermally driven process, which shows reduced performance at reduced temperature [19].

The increasing ohmic resistance in electrolyte at lower temperatures is a key issue

and has been the focus in the SOFC research area [3, 9, 20]. The ohmic losses associated with the fuel cell operation are mainly due to the resistance of ionic charge transport through the electrolyte layer. They are simply governed by Ohm's law:

$$V = iR = i(\frac{L}{A\sigma}). \tag{2.8}$$

where A is electrochemical reaction area, L is the length of the ionic transport path (electrolyte thickness), and σ is the ionic conductivity of the electrolyte material. V represents the voltage, which must applied in order to transport charge at a rate given by i. Therefore, this voltage V represents a loss. The performance of different fuel cells are generally compared on a per-unit-area basis of current density, thus it is also convenient to use area-normalized value to represent the resistance, which is area specific resistance (ASR) with units of $\Omega \cdot cm^2$. By using current density, $j = i/A$ and ASR, ohmic loss is expressed as:

$$\eta_{ohmic} = j \cdot ASR = j \cdot (\frac{L}{\sigma}). \tag{2.9}$$

Based on equation 2.9, the ohmic loss is proportional to the ion transport distance or inverse proportional to the ionic conductivity of electrolyte. Therefore, either reducing the electrolyte thickness or using an electrolyte with higher ionic conductivity can achieve a low ohmic resistance.

2.4 Thin Film SOFCs

As stated the previous sections, high performance of SOFCs at reduced temperatures can be achieved by decreasing ohmic loss across the electrolyte and the loss is directly proportional to the electrolyte thickness. For this reason, thin film SOFCs have been attracted great attention in low temperature SOFCs field.

Thin film SOFC is based on a reduced thickness electrolyte, which has lower ohmic resistance in comparison with conventional sintered ceramic pellets. The critical part related thin film SOFC is fabrication of a membrane electrolyte assemble by advanced thin film deposition techniques. The thin film electrolyte can either be assembled in a tri-layer SOFC structure in a form of free-standing membrane, or supported by a porous electrode, as illustrated in Figure 2.3.

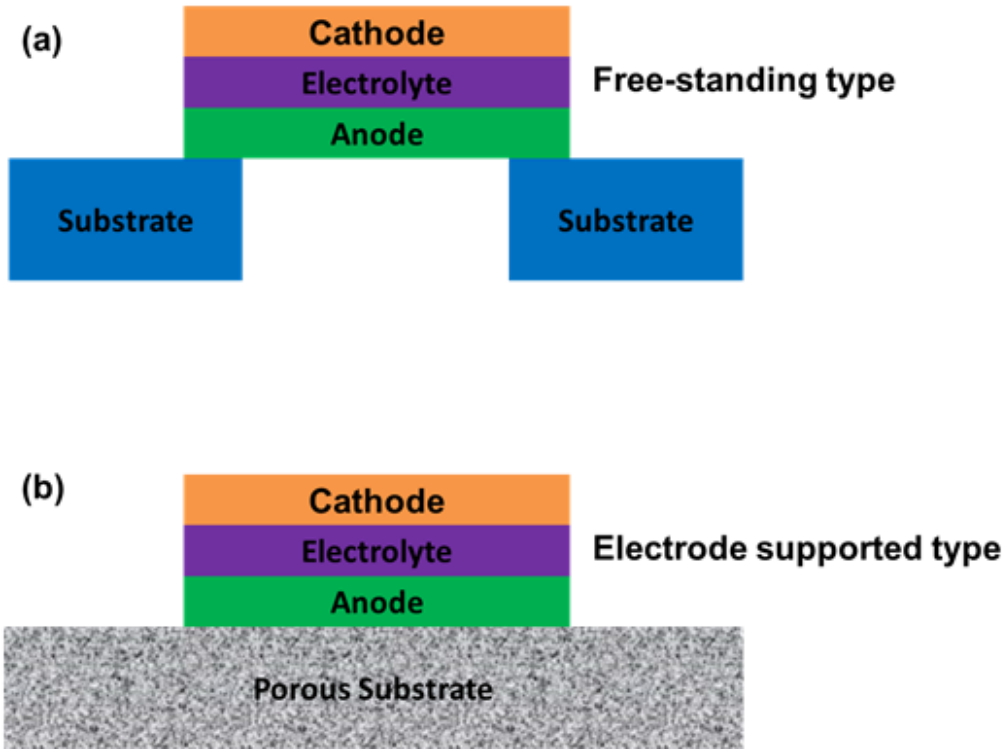

FIGURE 2.3: Schematic drawing of a free-standing SOFC (a) and an thin film SOFC membrane on a porous substrate (b) [3].

For free-standing type, usually silicon wafer is chosen as the substrate as it can be easily patterned with MEMS fabrication process. While for supported thin film SOFCs, a porous electrode is needed, which would greatly increase the electrode polarization. Thus, we will mainly focus on the free-standing micro-machined SOFCs (μ-SOFCs) in this part.

2.5 Proton-conducting SOFCs

Based on equation 2.9, another way to reduce the ohmic resistance of an electrolyte is to utilize alternative ionic conducting materials which possess higher ionic conductivity than conventional conductors such as YSZ in the reduced temperatures. Currently, fluorite ceramics such as doped-lanthanum gallate, doped-ceria, and doped-bismuth oxide materials have shown relative high oxygen ionic conductivity [19]. However, due to the high activation energy for oxygen ion conduction, these materials can still not suitable for low temperature less than 500 °C. In additional to currently developed oxygen-ion conducting ceramics, great interest has been paid in the proton-conducting electrolyte materials, in particular perovskite type ceramics [9].

Due to the high proton conductivity, acceptor-doped perovskites with the form ABO_3 have been extensively studied for protonic devices which require proton conductions [21, 22]. Recently, practical utilization of these materials has been used in various devices such as SOFC electrolyte, gas reformers and sensors [8, 21, 23–25].

Trivalent dopants are introduced into the host lattice of ABO_3 to substitute of the quadrivalent cations, which creates the formation of oxygen ion vacancies to retain the charge neutrality of the entire material. In order to achieve proton conduction, water is firstly adsorbed into the oxygen vacancies. Then one oxygen ion is dissociated in the vacancy and defective protons are formed [9]. The detailed proton migration process includes proton rotational diffusion around oxygen ion and proton transfer to the nearest oxygen ions (see Figure 2.4). This represents one of the reasons that make proton-conducting ceramics to be promising high performance electrolyte materials for low temperature SOFCs.

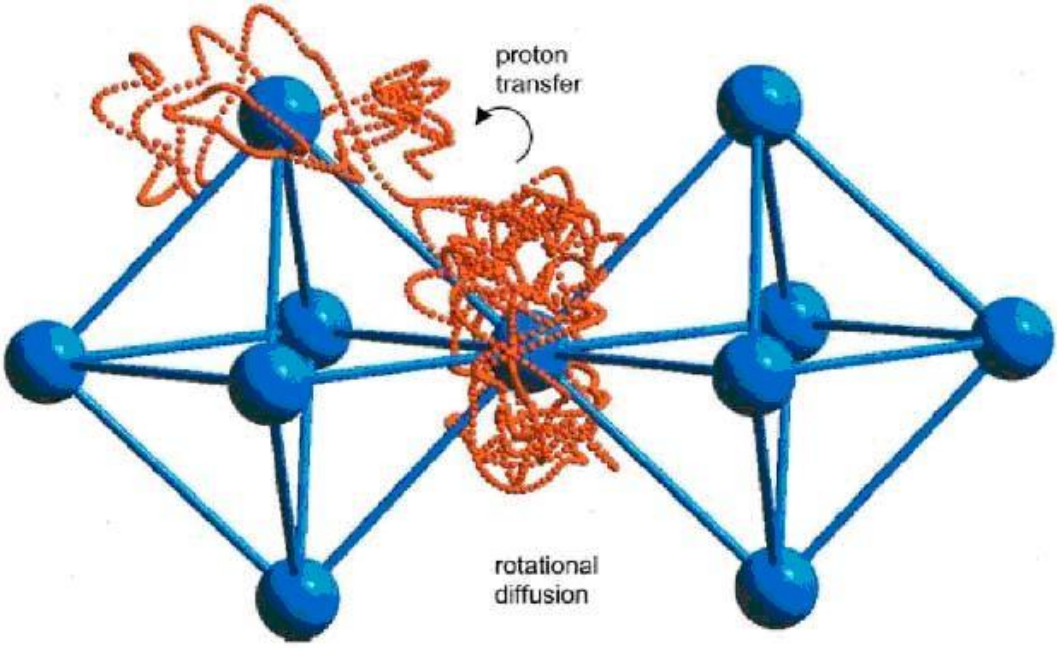

FIGURE 2.4: Two presentive traces of proton conduction in perovskite lattice: rotational diffusion and proton transfer [4].

2.5.1 Proton-conducting Electrolyte

Currently, several ABO_3 perovskites such as doped-$SrCeO_3$ and $BaCeO_3$ have been demonstrated to have high proton conductivity with the presence of water

or hydrogen-containing atmosphere in the early 1980s [23, 26, 27]. Dopants such as Y, Yb, Sc, and Nd have been used to dope these pervskites material in order to achieve high proton conductivity. $BaCeO_3$-based proton conductors are the most commonly used electrolytes for SOFCs applications [28, 29]. Nowadays the highest performance SOFC with proton-conducting Y-doped $BaCeO_3$ electrolytes has shown a peak power density of 700 mW/cm^2 at 400 °C [28]. Even though the cell shows very high fuel cell performance, the chemical instability of cerate based electrolyte has hindered the practical application of these materials for stable SOFC operation. Previous researches have founded that $SrCeO_3$ and $BaCeO_3$ electrolytes are easily turned into $SrCO_3$ and $BaCO_3$, due to the reaction with CO_2 [30]. It was also reported that $BaCeO_3$ electrolyte can also be easily reacted with water and decomposed into $Ba(OH)_2$, leading to barium deficiency formation and reducing the proton conductivity [28]. In comparison, zirconates materials such as doped-$SrZrO_3$ and $BaZrO_3$ are reported to have better chemical stability in various CO_2 and water atmosphere [4]. SOFCs with proton conducting Y-doped $BaZr_{0.5}Ce_{0.5}O_3$ (BCZY) have achieved a maximum power density of 900 mW/cm^2 at low temperature of 500 °C. In these BCZY SOFCs, the chemical stability was greatly improved as no formation of $Ba(OH)_2$ was observed in a long time test over 1100 hours in water presenting conditions[28].

Figure 2.5 reported the ionic conductivity of currently developed oxygen-ion conductors for low temperature SOFCs application and the proton conductivity of BZY electrolyte [31] and Y-doped barium cerate (BCY) [5] in low temperature of 300-600 °C. Both the the proton conductors (BZY and BCY) show significantly

smaller activation energy of 0.45-0.65 eV [9] and relative higher ionic conductivity in the low temperature range than oxygen ionic conductors such as SDC [32], LSGM [33], and YSZ electrolytes [34].

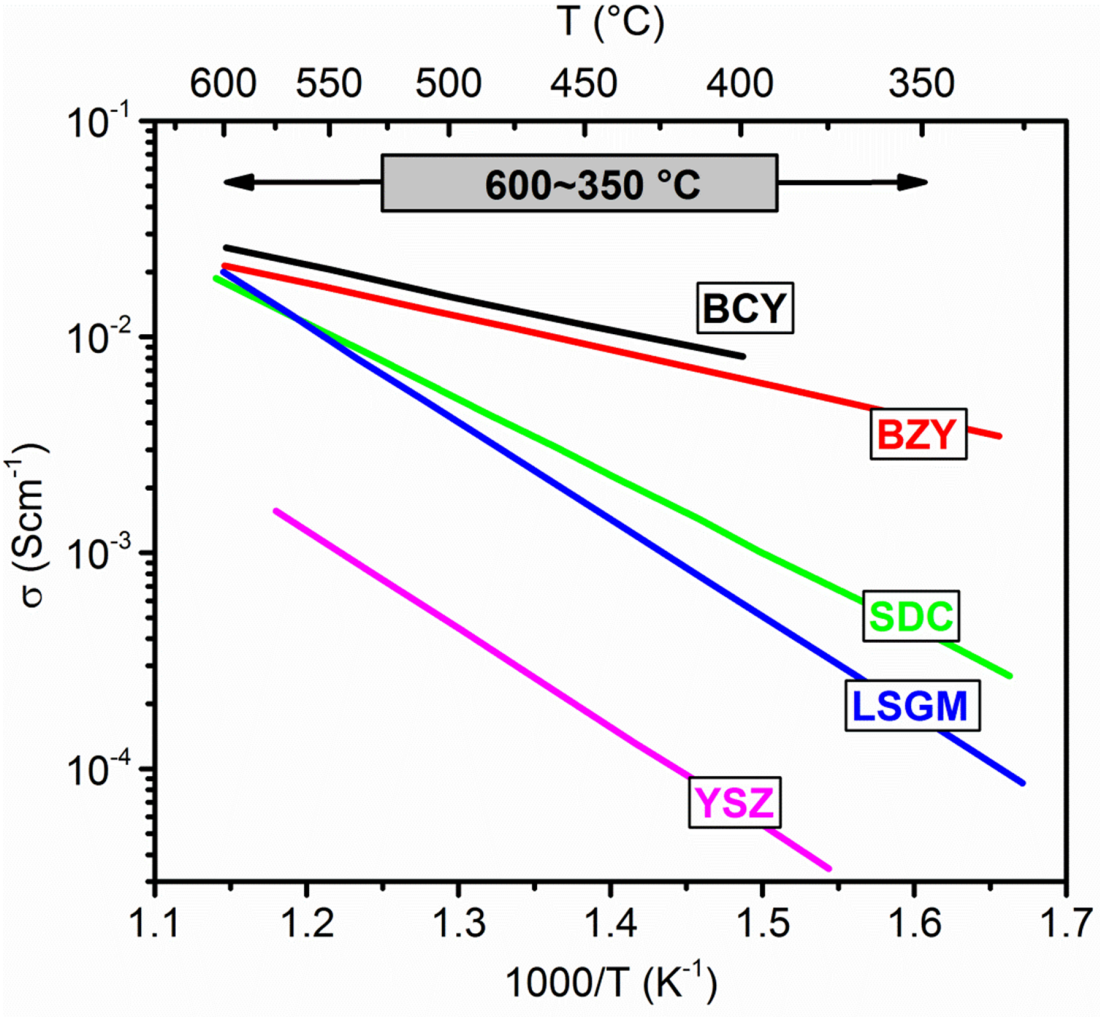

FIGURE 2.5: Comparison of the arrhenius conductivities of sintered proton-conducting pellets (BZY, BCY) with the current high performing oxygen-ion conductors, SDC, LSGMs, and YSZ [5, 6].

The crystallinity depended proton conductivity in BZY has been demonstrated in various studies recently [35–38]. Pergolesi et al. [38] reported that the highest proton conductivity for highly textured and epitaxial BZY thin film grown on single crystal MgO substrate wafer by PLD techniques. The super high bulk ionic conducting properties at low temperatures originated from the excellent crystalline

structure of epitaxial BZY thin film, which was expected to exclude the grain boundary blocking effects. Without the grain boundaries, the BZY thin film gives a high ionic conductivity of 0.01 S/cm at a low temperature of 350 °C. Figure 2.6 shows the comparison of proton conductivity of epitaxial BZY thin film deposited on single crystal MgO wafer by PLD and sintered BZY pellets with varied grain size of 0.5 and 1 μm [6]. It is shown that with the reduction of grain boundaries, the total conductivity increased significantly.

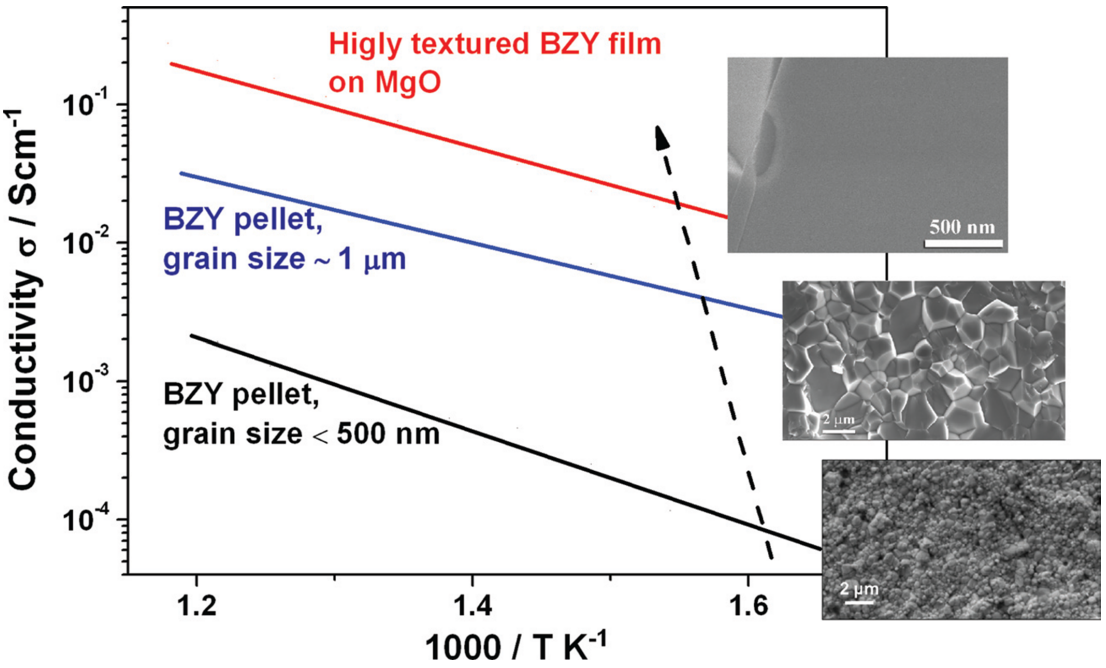

FIGURE 2.6: Arrhenius plots of the proton conductivity of highly-textured BZY film grown on MgO substrate, BZY sintered pellets with varied grain size from 1 μm down to several hundred nanometers [6].

2.5.2 Proton-conducting SOFCs

The highest performance of proton-conducting SOFCs are fabricated with a Y-doped $BaCeO_3$ (BCY) electrolyte and gained a maximum power densities of 0.9 and 1.4 W/cm^2 at 400 and 600 °C [29]. In their work, ultra-thin proton-conducting

BCY electrolytes (0.7 μm) were deposited on Pd film, which is a pure proton penetration layer. However, $BaCeO_3$ is not chemically stable and can react with CO_2 and produce carbonates, which would depress the high proton conductivity of this material. Thus, the BCY electrolyte is not suitable for long term fuel cell test.

By contrast, BZY-based proton-conducting SOFC has demonstrated superior mechanical and chemical stability in water and CO_2 environments. The sintering of dense BZY electrolyte is the critical challenging task because the sintering temperature is usually very high. The barium deficiency at high temperature is another problem related conventional sintering methods. Thus, introducing sintering aid into the electrolyte is an effective way to improve the sinterability of BZY electrolyte. Researchers have demonstrated that the sintering temperature and time can be reduced by introducing sintering aid such as Li, Ca, Pr, In, Zn, Sn, etc., which was summarized in ref [39]. Sun et al. [39] reported a novel sintered $BaZr_{0.7}Sn_{0.1}Y_{0.2}O_{3-\delta}$ (BZSY) electrolyte by partial substituting Zr^{4+} with Sn^{4+}. The cell with a 12 μm-thick BZSY electrolyte film achieved peak power densities of 360, 292, 214, and 146 mW/cm^2 at 700, 650, 600, and 550 °C, respectively. These values are relative high among the proton-conducting SOFCs with bulk sintered electrolytes. It is demonstrated that high electrochemical performance can be achieved by using chemical stable proton-conducting BZY-based electrolytes SOFCs [39, 40].

Generally, preparing ultrathin BZY-based electrolyte films is another effective approach to avert the sintering problem, as most of the thin film deposition techniques are conducted at temperature lower than 800 °C. A thin film electrolyte can also reduce the ohmic loss, which would promote the application of BZY-based thin film in low temperature SOFC applications. Thus, in this work we mainly focus on proton-conducting μ-SOFCs. Table 2.1 summarized the fuel cell structures and performance of the proton-conducting μ-SOFCs with thin film electrolytes in the open literature.

The first free-standing proton-conducting μ-SOFCs were fabricated by Shim et al. [41]. The nanoscale BZY electrolytes which were deposited by ALD and PLD techniques were integrated into micro-machining process. Electrochemical cells (H_2, Pt/BZY/Pt, air) were fabricated incorporating BZY thin film electrolytes into porous platinum electrodes which were fabricated by sputtering at high pressure. The fuel cells have gained high performance in terms of peak power densities, which reached to 136 mW/cm^2 at 400 °C for SOFC with ALD BZY electrolyte and 120 mW/cm^2 at 450 °C for PLD BZY cells. This cell shows the highest performance at these testing temperatures compared to the literature values.

Chang et al. [42] demonstrated a pinhole-free and dense BZY SOFC on AAO substrate. The deposition parameter such as oxygen partial pressure was varied to optimize the BZY electrolyte structure and surface morphology. A porous substrate-based thin film SOFC using fully dense BZY showed a high OCV value and a maximum power density of 44 mW/cm^2 at 450 °C.

Ji et al. [43] improved the fabrication of BZY electrolyte on AAO substrate and studied the effects of cathodic modification by inserting a cathodic interlayer with different porosity by PLD technique for low temperature SOFCs. With the additional electrolyte layer, the electrode reactions were enhanced and the electric short-circuit problem was reduced simultaneously. The cell with double layer electrolytes gives peak power density of 2 mW/cm^2, which is 56% higher than the cell with only one BZY electrolyte due to enhanced cathodic reaction sites and significant reduced cathodic resistance.

Su et al. [44] have successfully fabricated a cup-shaped free-standing fuel cell with BZY thin film electrolyte with PLD and silicon MEMS process. By making the flat thin film BZY electrolyte into 3D structure, the total reaction areas of BZY membrane have been greatly increased. 300 nm thick BZY electrolyte layer was deposited by PLD technique on a cup-shaped Si wafer, which has been pre-patterned with cup shape trenches. The performance of arrayed cup-shaped μ-SOFC tested at 400 °C shows increased power output and density benefiting from the additional reaction areas in the trenches.

Kim et al. [45] fabricated a 3D crater patterned proton-conducting μ-SOFCs with BZY electrolyte by using a novel nonlithographic nanospherical patterning (NSP) method. The 120 nm thick BZY thin film was deposited by PLD and thin film porous Pt layers were deposited by sputtering to sever as the cathode and anode. The 3D structured fuel cells achieved peak power densities of up to 186 mW/cm^2 at 450 °C using hydrogen as fuel, which was the highest value for BZY-based μ-SOFC in the literature.

Table 2.1: Summary of μ-SOFCs performances with protonic ceramic electrolytes reported in the literature.

Group	Reference	Cell Structure	Materials (anode-electrolyte-cathode)	Electrolyte Thickness (nm)	OCV (V)	Peak Power Density (mW/cm^2)	Temperature °C	Fuel
Nanyang Technological University	Su et al.[44]	Free-standing	Pt-BZY-Pt	300	0.56	8	400	H_2
	Ha et al.[46]	AAO supported	Pt-BZY-Pt	900	0.8	6	250	CH_4O
	Li et al.[47]	Free-standing	Pt-BCY-Pt	300	0.59	30	400	H_2
Stanford University	Shim et al.[41]	Free-standing	Pt-BZY(PLD)-Pt	130	1.12	120	450	H_2
			Pt-BZY(ALD)-Pt	110	1.09	136	400	H_2
	Kim et al.[45]	Free-standing	Pt-BZY-Pt	120	0.85	186	450	H_2
Korea University	Bae et al.[48]	Free-standing	Pt-BCY-Pt	200	0.98	145	400	H_2
			Pt-BCY/BZY-Pt	200	0.89	48	400	H_2
			Pt-BZY/BCY/BZY-Pt	200	0.78	8	400	H_2
			Pt-BZY-Pt	200	1.08	27	400	H_2
			Pt-BZY/BCY-Pt	200	1.06	40	400	H_2
			Pt-BCY/BZY/BCY-Pt	200	1.05	62	400	H_2
Seoul National University	Kang et al.[49]	AAO supported	Pd-BZY-Pt	1000	1.0	9	400	H_2
	Chang et al.[42]	AAO supported	Pt-BZY-Pt	1000	1.04	44	450	H_2
	Park et al.[50]	AAO supported	Pt-BZY-Pt	1340	1.1	21	450	H_2
Harvard University	Adam et al.[51]	Free-standing	Pt/Pd-BZY-Pt	136	0.95	40	495	H_2

BCY: Y-doped BaCeO3
ALD: Atomic layer deposition

2.6 Pulsed Laser Deposition

Like most physical vapor deposition (PVD) methods, Pulsed Laser Deposition (PLD) is also a type of PVD method under high vacuum circumstance. The desired films are formed by using a high-energy pulsed laser beam to ablate the target of the materials. PLD has gained a great attention to the research community and industrial application due to the ease of operation and the good conserve stoichiometry of deposited materials. In this work, we utilize PLD to deposit several kinds of electrolyte and electrode materials.

A typical PLD system was depicted in Figure 2.7. PLD has several specific advantages over other thin film fabrication methods. The main advantage originates from the instinctive laser ablating process to remove the materials. The pulsed laser strikes the target to form ejected plume with materials plasma. The ejected vapor or plume then is accumulated on a substrate which was placed in front of the target with a short distance. The detailed mechanisms on how PLD works are very complicated, but generally the process can be summarized into the following four stages:

(i) Plasma creation: high-energy laser ablation of the target to evaporate the material, forming high energy plasma;

(ii) Plasma movement: plasma transfer from the target to the chamber vacuum in a specific direction;

(iii) Film deposition: the ablated plasma are encountered with substrate and bonded to the substrate surface;

(iv) Film growth & nucleation with remaining kinetics and energy.

Compared to other thin film fabrication techniques, it is easier to get the desired thin film stoichiometry as almost all materials can be ablated under such high-energy density pulsed laser. The deposition process can occur in ultra-high vacuum or in the presence of a background gas, such as oxygen, which is commonly used when depositing oxides to fully oxygenate the deposited films.

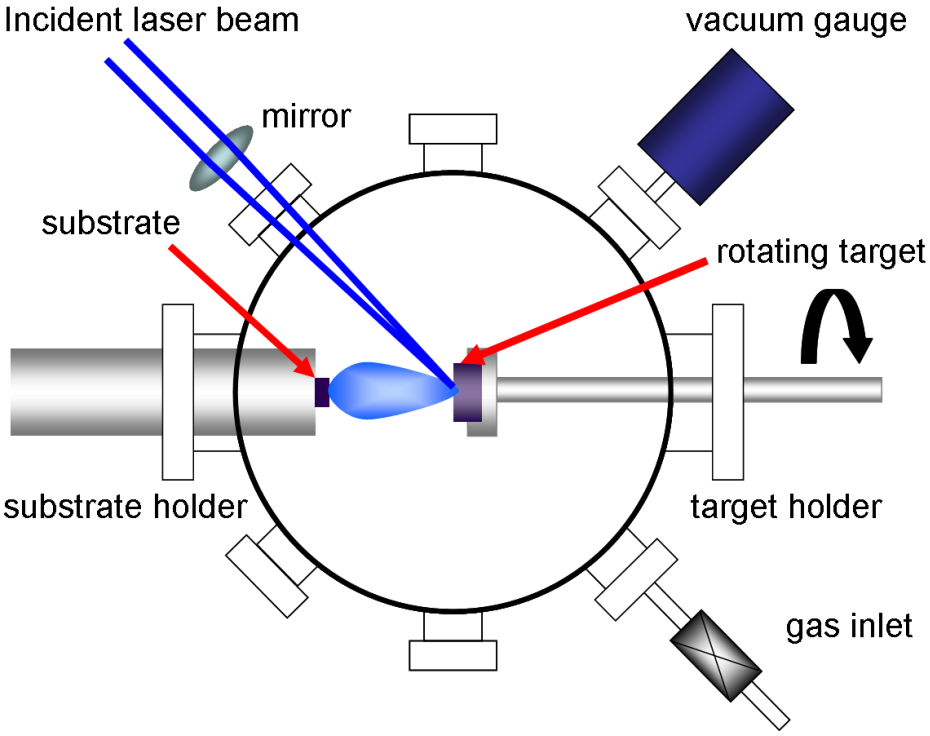

FIGURE 2.7: Schematic view of a PLD system [7]

The deposition parameters, such as oxygen partial pressure, substrate temperature, and target to substrate distance (T-S distance) have great effect on the thin film quality. For example, oxygen partial pressure can affect the surface morphology of the film, as the diffusion distance of the ablated species is related to the pressure. In high vacuum condition, the ejected species have less hindrance from the surrounding environment and can travel a long distance. However, in

higher pressure condition, the diffusion route was hindered by surrounding oxygen molecules, resulting in a short travel distance. Therefore, optimization of the deposition conditions in PLD techniques is critical to ensure a high quality thin film. In this work, we will utilize PLD to fabricate nanoscale proton-conducting electrolyte and cathode materials for low temperature SOFCs. The effects of different deposition conditions will be studied and optimized.

2.7 Chapter Summary

For low temperature SOFCs to operate at targeted temperature regime, which is usually below 500 °C, proton-conducting oxides would be promising electrolyte materials than oxygen-ion conductors due to lower activation energy of proton conduction. By combining the thin film μ-SOFCs and proton-conducting electrolytes, the impressive fuel cell performance can be achieved. Nevertheless, among the limited number of reports on μ-SOFCs using proton-conducting electrolytes, the fuel cell performance reported was still much lower than those using oxygen ion-conducting electrolytes. The yet impressive performance of μ-H-SOFCs may originate form the poor stability of electrolyte or cathodic reaction. When proton-conducting electrolytes are utilized, the water evolution reaction shifts from anode to cathode, making the already complex cathode reactions even more complicated. In this regard, chemical stability study and cathodic modification are critical issues related to μ-H-SOFCs performance enhancement, which would be the main research focus in this dissertation.

Chapter 3

Nanoscale Doped Barium Cerate Electrolytes for Low Temperature SOFCs

3.1 Introduction

In practical SOFC operation, a good chemical stability of selected electrolytes as well as a high ionic conductivity is required for long-term fuel cell operation. Currently, yttria-doped $BaZrO_3$ (BZY) and yttria-doped $BaCeO_3$ (BCY) are two of the most investigated proton-conducting ceramic electrolyte materials. BZY is known for its good proton-conductivity and excellent chemical stability under fuel cell operating conditions, but the proton conductivity in practice is still relatively

Part of this chapter is reprinted from *Journal of Power Sources*, Vol 268, Yong Li, et al., "Chemical stability study of nanoscale thin film yttria-doped barium cerate electrolyte for micro solid oxide fuel cells", Pages 804-809, Copyright (2014), with permission from Elsevier.

low due to its poor sinterability which results in high grain boundary density that blocks proton transportation [9]. On the other hand, BCY has the highest ionic conductivity among all the proton-conducting ceramics [4, 5]. Thin film BCY has been used to demonstrated the feasibility as a suitable electrolyte material for very low temperature (below 500 °C) SOFCs, and decent cell performance was obtained. Iijima et al. [28] coated a 2 μm-thick BCY thin film electrolyte by PLD on a Pd substrate and use screen-printed $La_{0.6}Sr_{0.4}CoO_3$ and Pt as the cathode and anode. A high maximum power density of 0.9 W/cm^2 with OCV of over 1.0 V was obtained at 400 °C. Bae et al. [48] reported a silicon-supported μ-SOFC using nano thin film BCY with thickness of only 200 nm deposited by PLD, and a maximum power density of 145 mW/cm^2 with an OCV of 0.98 V at 400 °C.

One major drawback of using ceria-based electrolytes is the poor chemical stability that often leads to a rapid degradation of cell performance. [28, 36, 52, 53]. The degradation originates from the high basicity of the electrolyte that facilitates $BaCO_3$ to react with CO_2 and H_2O and decompose to $BaCO_3$, CeO_2, or $Ba(OH)_2$ [30, 54, 55]:

$$\mathrm{BaCeO_3}(s) + \mathrm{H_2O}(l) - \mathrm{CeO_2}(s) + \mathrm{Ba(OH)_2}(s/l). \tag{3.1}$$

$$\mathrm{BaCeO_3}(s) + \mathrm{CO_2}(g) - \mathrm{CeO_2}(s) + \mathrm{BaCO_3}(s). \tag{3.2}$$

In an effort to avoid the electrolyte decomposition, 1 μm-thick BZY was coated on a sintered bulk BCY pellets (thickness of 1 mm) to utilize its chemical stability as a protective layer against atmospheric CO_2 and moisture, and a significant improve

of performance stability was observed [56]. Similar concept was also applied to μ-SOFCs using nano thin film BCY electrolyte (thickness of 200 nm) by depositing a 20 nm-thick BZY layer on either cathode, anode, or on both sides of BCY using PLD [48]. However, the additional BZY capping layer(s) did not improve the overall chemical stability of the composite electrolyte, and rapid degradation of cell performance was still observed, possibly due to the insufficient thickness of capping layer for the nano thin film BCY. Further investigations for the behaviors of nano thin film BCY at targeted low temperature range is necessary to optimize the performance of the μ-SOFCs using this promising material.

Although the chemical stability of bulk BCY electrolyte has been well-investigated at higher temperatures [57–60], particularly for the reactions with CO_2 and H_2O [61], studies for nanoscale thin film BCY at temperatures below 500 °C are still rare due to the interests in using BCY for very low temperature SOFCs are just growing from the recent successful demonstrations [28]. In addition, most of the chemical stability analyses of cerium based proton-conducting electrolyte were performed in H_2O/CO_2 containing atmosphere or boiled water to simulate the fuel cell operating conditions and not directly under actual fuel cell operating conditions [30, 54, 55], which may not reflect the effect of charge transport on the corrosion behaviors during fuel cell operation. Therefore, this work is dedicated as an initial thorough study on the chemical stability of nano thin film BCY as the electrolyte for μ-SOFCs operated at very low temperature range of 300 to 400 °C. The reactions of BCY with CO_2 and H_2O as well as the reduction of cerium after fuel cell test were identified to clarify the causes of cell performance degradation.

3.2 Experimental Methods

3.2.1 Fabrication and Test of BCY μ-SOFCs

Figure 3.1(a) shows the schematic of the silicon-based μ-SOFC with free-standing BCY electrolyte membrane fabricated using silicon micromaching processes, as previously reported in [10]. BCY thin films with thickness of 300 nm were deposited by PLD on a free-standing silicon nitride membrane supported by a silicon wafer [44]. A 248 nm KrF excimer laser (Lambda Physik) with laser fluence of 2.5 J/cm^2 per pulse was used to ablate a sintered $BaCe_{0.9}Y_{0.1}O_{3-\delta}$ pellet target (Able Target Limited, China) with a target to substrate distance of 50 mm. The main chamber was vacuumed to a base pressure of 1×10^{-4} Pa, and the oxygen partial pressure was fixed at 1.0 Pa. After deposition, all the samples were cooled to 400 °C with a cooling rate of 10 °C/min to avoid crack formation on the membrane caused by the difference of thermal expansion coefficient between silicon substrate and the BCY membrane. The deposited films were then continued to cool to room temperature by natural convection in the chamber with same oxygen partial pressure. After the deposition of BCY electrolyte, the Si_3N_4 supporting layer was removed by relative ion etching (RIE) with CF_4 gas to obtain the free-standing BCY electrolyte. Porous Pt thin film cathode and anode with thickness of 50 nm were deposited on both sides of the electrolyte by using DC sputtering with a DC power 250 W and pressure of 80 mTorr at room temperature.

The fuel cell performance was tested with a custom-made μ-SOFC test station as described elsewhere in [10]. The test was performed under dry hydrogen fuel at a

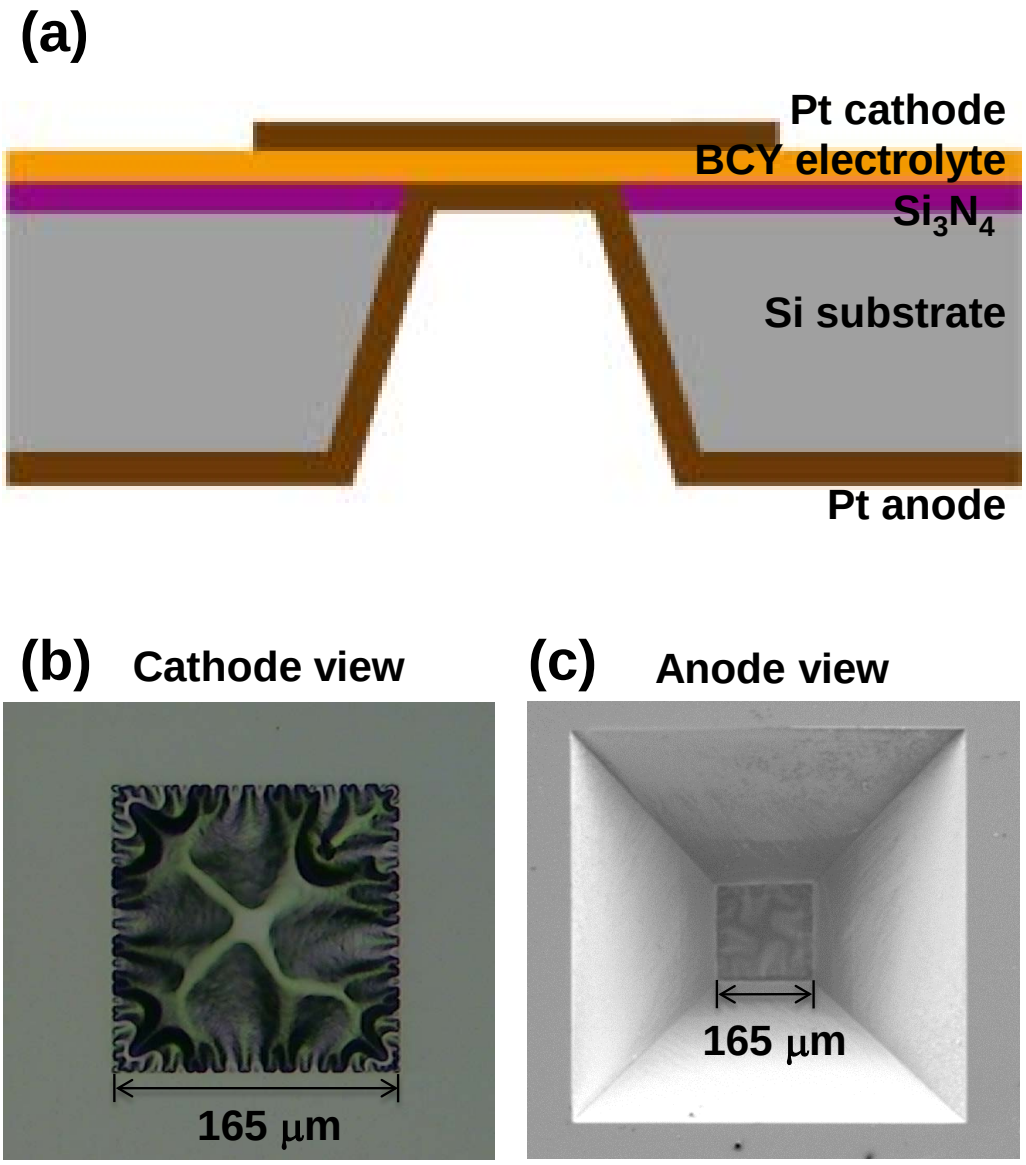

FIGURE 3.1: Structure of free-standing μ-SOFC device. (a) Schematic of cell structure; (b) Optical microscopy image of SOFC seen from cathode side; (c) SEM image of SOFC seen from anode side.

flow rate of 20 *sccm* and under ambient air as oxidant, and therefore the chemical reactions between BCY and CO_2 and H_2O were with those species contained in the ambient air. The polarization curves were measured at 300, 350, and 400 °C using a potentiostat system (Solartron 1470E) and a frequency response analyzer (FRA) (Solartron 1255B).

3.2.2 Electrolyte Characterizations

The phase and crystal structure of BZY and GDC films were characterized by grazing incidence X-ray diffraction (GIXRD) method using a PANalytical Empyrean XRD system, with the glancing incident angle being kept at 1° for all the measurements. The collected XRD patterns were refined by the Rietveld method using the X'pert HighScore software package. The substrate Si (400) peak was used as the reference to confirm a corrected zero point for subsequent characterizations. The composition of the BCY electrolyte and its chemical states were determined using X-ray photoelectron spectroscopy (XPS, Kratos AXIS Ultra) with a monochromatic Al Kα (1486.71 eV) X-ray radiation (15 kV/10 mA). The high-resolution spectra scans over different element peaks were recorded in a step of 0.1 eV under constant pass energy of 40 eV. The binding energies were calibrated with reference to the adventitious hydrocarbon contamination peak located at 284.8 eV. The morphologies of the electrolytes were characterized using a field-emission scanning electron microscopy (FE-SEM, JEOL JSM-7600F).

3.3 Chemical stability study of BCY electrolytes

3.3.1 Electrochemical Performance of BCY Cells

The fabricated μ-SOFC with BCY electrolyte is shown in Figure 3.3(b) and (c). The free-standing electrolyte membrane shows severe buckling, which reflected the compressive stress that was often observed in oxide thin films deposited at high

temperature [62–64]. In the fuel cell polarization curves (Figure 3.2), the OCVs started at a low value of 0.79 V at 300°C, and dropped to 0.68 V at 350°C, and finally down to 0.59 V at 400 °C. The maximum power densities were also at low values of 2, 5 and 30 mW/cm^2 at 300, 350 and 400 °C, respectively. As shown in the SEM images of the BCY membrane cross-sectional view (Figure 3.3), no noticeable crack was observed in the electrolyte before fuel cell test, and after tested at 400°C, several cracks initiated on the BCY surface and perforated across the electrolyte. The formation of such cracks could have caused gas leakage that resulted in the decreasing OCV values and the poor fuel cell power performance.

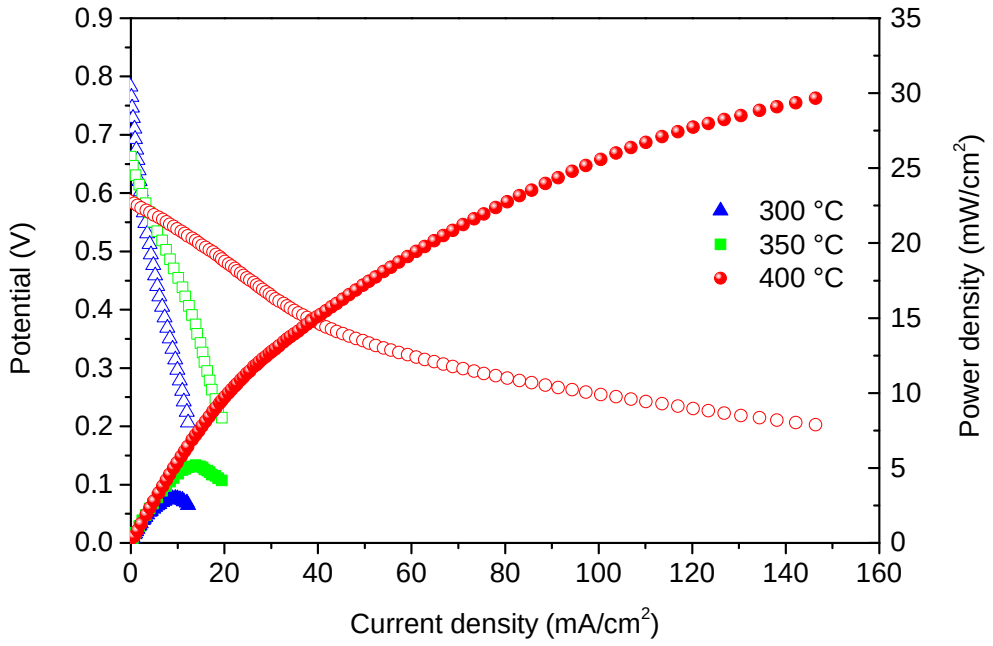

FIGURE 3.2: Polarization curves at temperatures of 300, 350, and 400 °C.

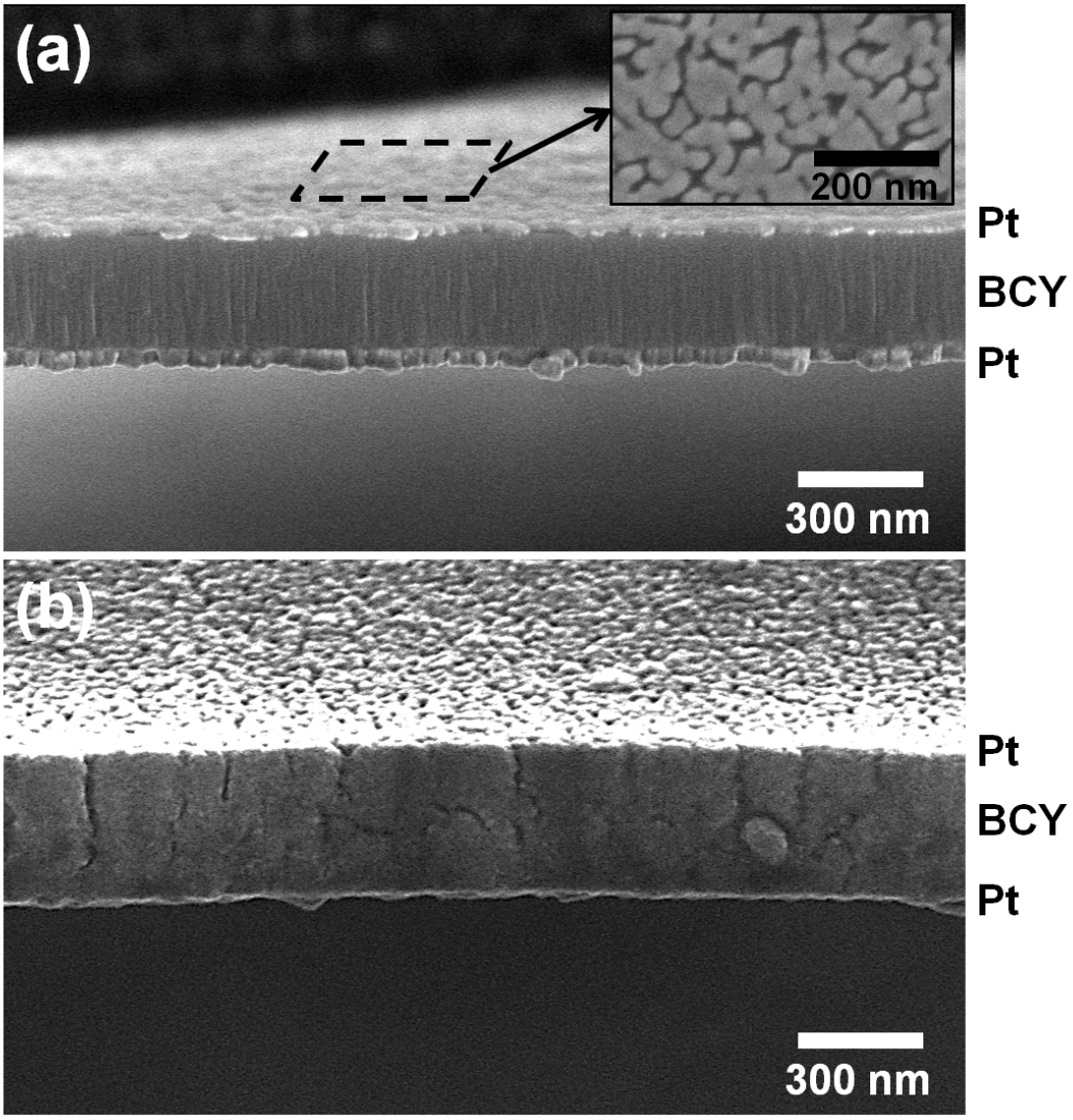

FIGURE 3.3: Cross-sectional FE-SEM images of the BCY electrolyte before (a) and after fuel cell test at 400 °C (b). The inset figure in (a) shows a magnificent view of the porous Pt surface.

3.3.2 Microstructural Characterization

The XRD characterizations were first carried out to verify the changes of lattice parameters of BCY electrolyte (Figure 3.4) before and after the fuel cell test. Both the as-deposited and tested BCY electrolytes were indexed to an orthorhombic perovskite structure (space group *Pmcn*), indicating that the BCY electrolyte has retained the same crystal structure after the fuel cell test. However, the XRD

pattern of BCY after test shows a noisier background, and several new small peaks of $BaCO_3$ appeared after exposure to CO_2 and moisture during fuel cell test. In addition, an obvious peak shift of about 0.2° to the lower angle was observed in the tested sample, indicating an increase in the plane distance. As summarized in Table 3.1, the cell volume expanded from 338.01 $\mathring{A}^3$ to 349.88 $\mathring{A}^3$ after the fuel cell test. This volume expansion could have changed the stress level of the freestanding BCY electrolyte and resulted in the cracks we observed in the electrolyte membrane.

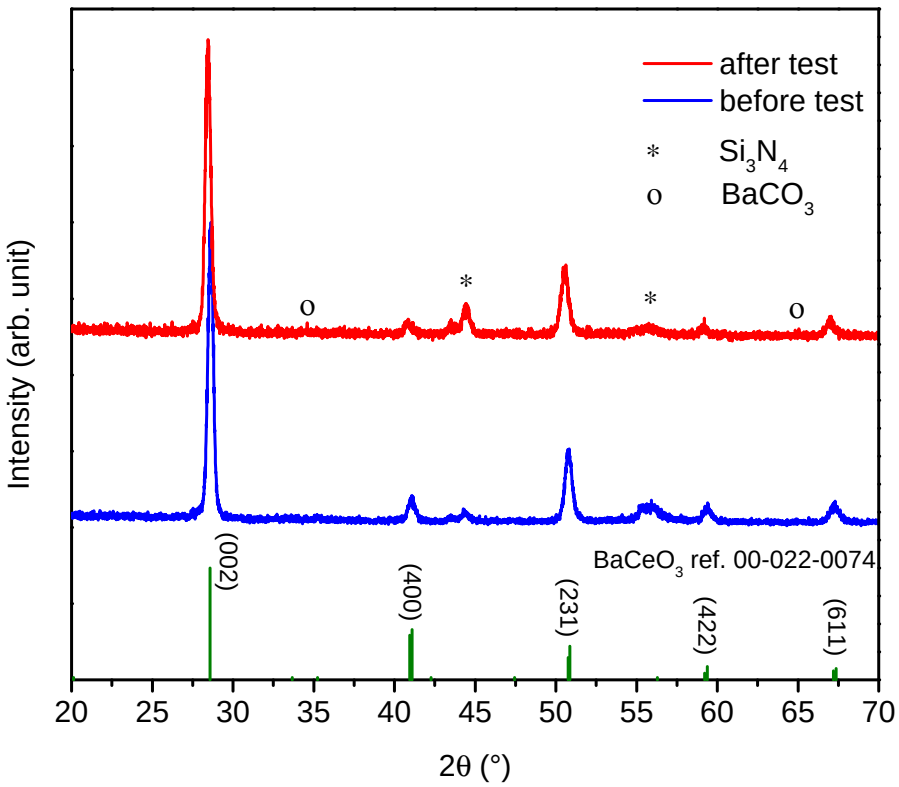

FIGURE 3.4: GIXRD patterns of BCY electrolyte before and after fuel cell test at 400 °C.

Table 3.1: Crystal structure and parameters obtained by XRD refinement

	2θ (°)	d-spacing ($\AA$)	a ($\AA$)	b ($\AA$)	c ($\AA$)	Volume ($\AA^3$)
Before	28.585	3.12023	8.7529	6.1914	6.2371	338.01
After	28.435	3.13635	8.9426	6.233	6.2767	349.88

3.3.3 XPS Study of the Chemical Stability of BCY

We further identified the chemical decomposition of BCY electrolyte by XPS. Figure 3.5-3.7 shows the high-resolution spectra of Ba 3d, O 1s, C 1s, respectively. For the as deposited sample, the Ba 3d photoelectron peaks can be resolved into a set of spin-orbit doublets of Ba 3d5/2 (779.1 eV) and 3d3/2 (797.4 eV), where the peak separation of 18.3 eV is consistent with the values reported in the literatures [65]. The perfectly symmetric Ba 3d5/2 peak was resolved into a single peak with Gaussian fitting, indicating that a pure $BaCeO_3$ chemical state is presented in the electrolyte. After fuel cell test at 300 °C, two small peaks formed beside the two original Ba 3d peaks with slightly higher binding energies of 779.6 eV and 797.9 eV but a same peak difference of 18.3 eV. These two new peaks indicate the formation of a new set of Ba 3d doublets (Ba 3d5/2 and 3d3/2), which corresponds to a different barium binding state that can be resolved to $Ba(OH)_2$ as indexed to reference [66]. As the testing temperature was increased to 400 °C, the intensities of these two additional peaks increased further. Similar trend was also observed in the O 1s spectra, as shown in Figure 3.6. The O 1s XPS spectra show broad and asymmetric peaks and can be fitted to three overlapped peaks with binding energy in the region of 528-534 eV. The fitted peaks located at 530.9, 528.8, 532.2 eV were resolved to lattice oxygen, metal oxide and absorbed oxygen, respectively. For the tested sample, another O 1s peak formed at higher binding energy (534

eV), which is also identified to associate with the formation of $Ba(OH)_2$. The C 1s spectra are also deconvoluted and shown in Figure 3.7 for comparison. The concentration of C 1s spectra almost kept constant except a slight increase at 400 °C, indicating a much more stable carbon oxidation state than Ba after fuel cell test. Therefore, we can confirm that the newly formed Ba peaks are mainly attributed to the formation of $Ba(OH)_2$ from the electrolyte reaction with moisture. Previous researches reported that barium cerate reacts more easily with CO_2 than with water vapor, and the reaction with H_2O is not significant at the fuel cell operating conditions (400-700 °C) [53, 67]. From our results, however, the analysis of Ba 3d, O 1s and C 1s XPS spectra shows the reaction with water to form $Ba(OH)_2$ is also significant and contributes to the degradation of nano thin film BCY at temperatures below 400 °C.

The oxidation state of cerium is another important indicator for the poor chemical stability of nano thin film BCY electrolyte under low temperature fuel cell operating conditions. The change in oxidation state of cerium can be observed by analyzing Ce 3d spectra, as shown in Figure 3.8. Due to shake-up, shake-down and multiplet splitting effects, the shape of the Ce 3d spectra contains contributions from many components, leading to complex fine structure curve fittings [68, 69]. Both of the Ce 3d spectra can be resolved into 11 peaks, as illustrated with different colors. Ten cerium peaks following the notation defined by Burroughs et al. [70] using (u, v)s are attributed to the two spin-orbit split components of the Ce 3d photoemission process: the Ce 3d5/2 and Ce 3d3/2. An Auger line of barium appears in this energy range, which is colored with purple. All the Ce 3d spin-orbit

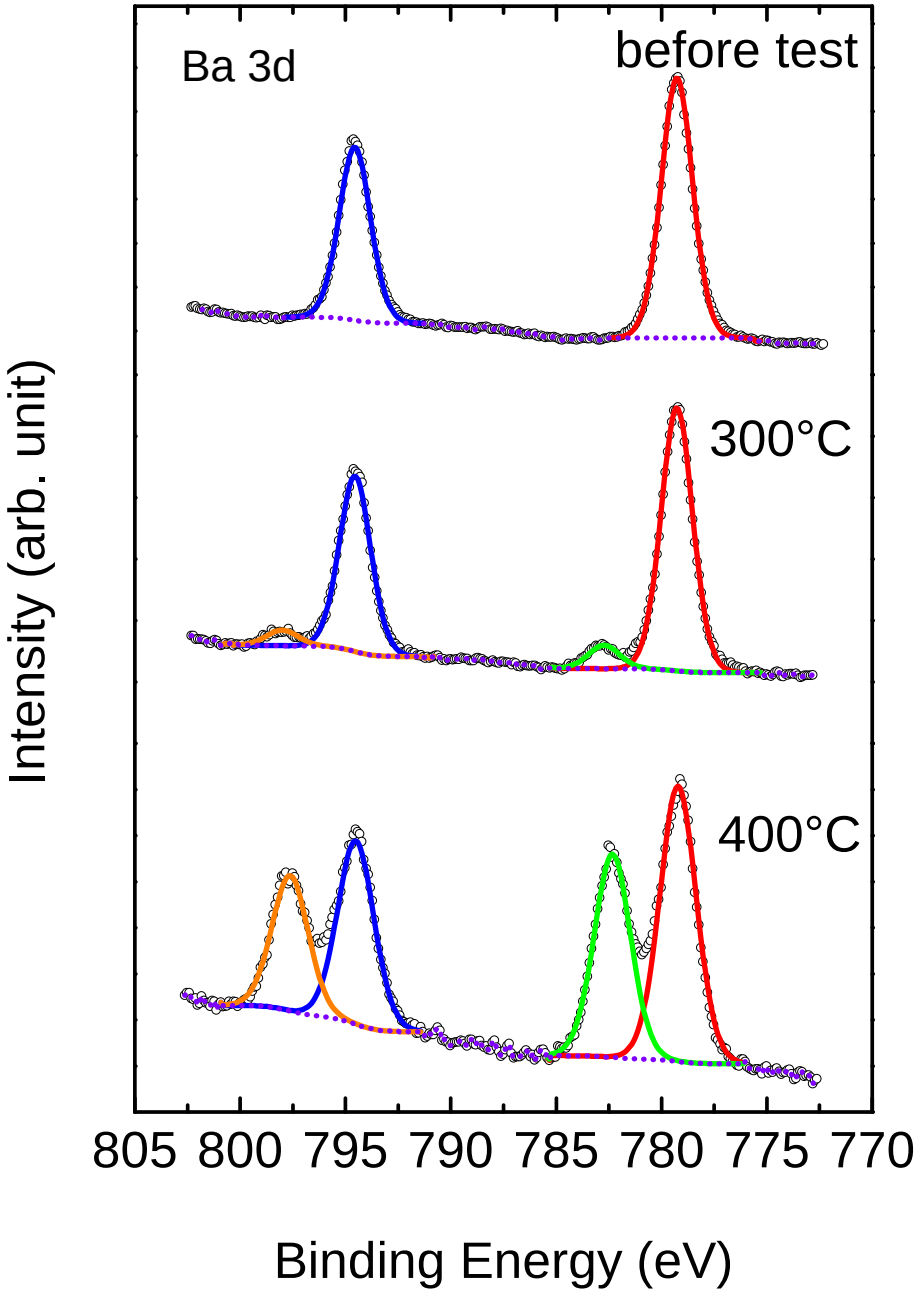

FIGURE 3.5: XPS spectra of Ba 3d for the BCY electrolyte before (top) and after fuel cell tested at 300 (middle) and 400 °C. (bottom). The original data, fitted spectra and Shirley background are shown in hollow points, colored solid lines and dotted line, respectively.

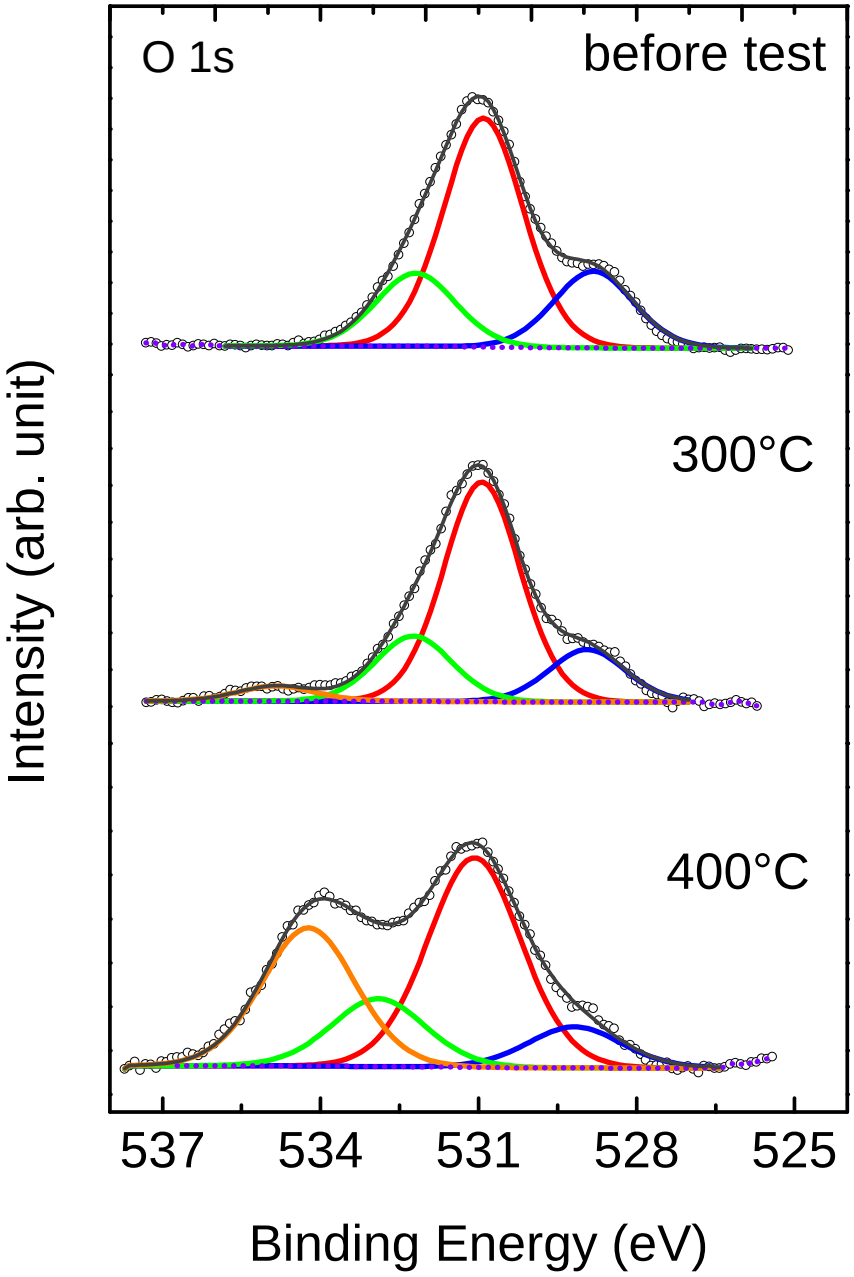

FIGURE 3.6: XPS spectra of O 1s for the BCY electrolyte before (top) and after fuel cell tested at 300 (middle) and 400 °C. (bottom). The original data, fitted spectra and Shirley background are shown in hollow points, colored solid lines and dotted line, respectively.

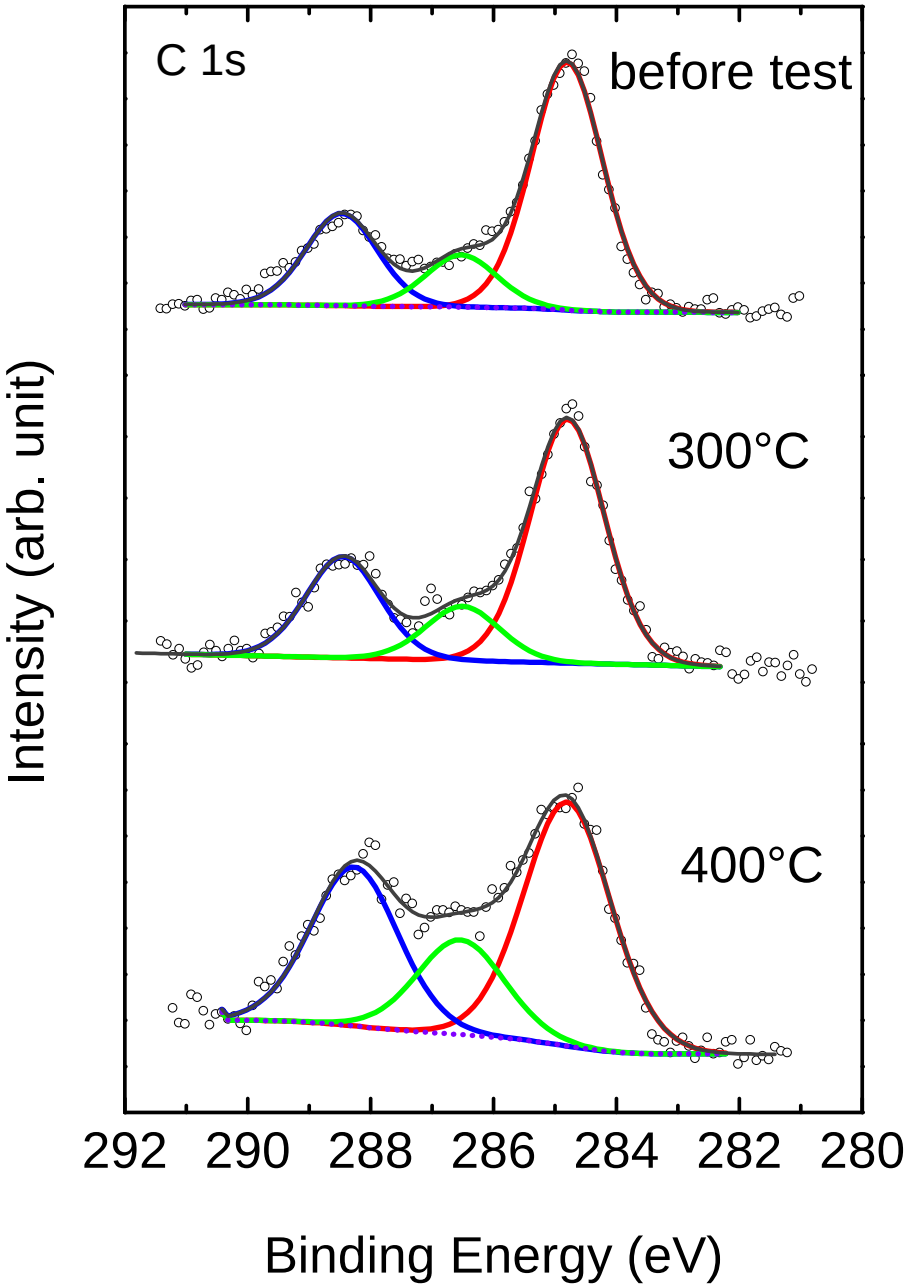

FIGURE 3.7: XPS spectra of C 1s for the BCY electrolyte before (top) and after fuel cell tested at 300 (middle) and 400 °C. (bottom). The original data, fitted spectra and Shirley background are shown in hollow points, colored solid lines and dotted line, respectively.

splitting are in the range of 18.2-18.6 eV, which is consistent with data previously reported in the literature [71]. The core level binding energies and atomic compositions of Ce 3d doublets peaks (uv)s are calculated and summarized in Table 3.2 following Romeo et al.'s method [72], which is a simple and accurate way to analyze the complexity of Ce 3d spectra. The fitted curves are classified into two different sets of Ce 3d status according to their binding energies. Previous studies have confirmed that the doublets peaks, $u'''v'''$, $u''v''$, uv are originated from Ce^{4+} oxidation state, and $u'v'$ and u^ov^o are attributed to the Ce^{3+} oxidation state [72]. As shown in Figure 3.8, peaks $u'v'$, u^ov^o are presented in both the untested and tested samples, meaning that Ce^{3+} have already existed in the BCY electrolytes before the fuel cell test, which is not expected in the fully oxidized BCY electrolyte. We speculate that the observed Ce^{3+} is present at the electrolyte surface that was exposed to ambient air that facilitates the reduction. Another possible reason may be from the X-ray induced photo reduction of cerium based samples during XPS test, though the mechanism is in principle known but not entirely understood [73]. The shape of the highest binding energy peak pair $u'''v'''$ (at 915eV and 897 eV), which can be indexed to CeO_2 spectra [68, 72], gives a larger enclosed area under the peaks as compared with the untested sample. The formation of CeO_2 during the fuel cell test gives a direct evidence of both reactions with CO_2 and water vapor. On the other hand, the components of Ce^{4+} $u''v''$ and uv have dramatically decreased compared with the fresh samples, especially for $u''v''$ peaks. This decrease is attributed to the partial reduction of Ce^{4+} into Ce^{3+} species, which can be confirmed by the noticeable increase in $u'v'$ and u^ov^o peaks in the tested sample. Particularly, for the peaks of u^ov^o, the calculated concentration has increased from

9.65% to 28.35%. Considering all the oxidation states of Ce elements in the BCY electrolyte, the ratio of Ce^{3+}/Ce^{4+} has increased from 31.25% to 47.14% after fuel cell test. The co-existence of both valence states is attributed to the partial reduction of Ce (from Ce^{4+} to Ce^{3+}) [74]. Since the transformation of Ce valence state has a strong influence on the mechanical properties of Ce-based oxides [75], the large amount of Ce reduction can be associated with the lattice expansion observed from our XRD results. Such lattice expansion in a bulk BCY may not be directly visible and the effect was reflected as impact on the mechanical property, but in nano thin film BCY the lattice expansion can have directly resulted in visible cracks as we observed. Further investigation is necessary to find out the actual correlation between the changes in Ce oxidation state and the fracture of the nanoscale thin film BCY. Earlier work has shown that the existence of mixed Ce^{4+}/Ce^{3+} valence state in the CeO_2-electrolyte can provide electronic conduction through the electron hopping-transport mechanism between Ce^{4+} and Ce^{3+} [76]. For oxygen ion conductors, the ionic conduction is dominate at lower temperature range in CeO_2-based electrolytes, and at higher SOFC operating temperature ($>$ 600 °C) the electronic conductivity becomes comparable to or eventually greater than the ionic conductivity [77, 78]. We also speculate the existence of electronic conduction due to the presence of CeO_2 and mixed Ce^{4+}/Ce^{3+}, which would result in the low OCVs.

In addition, the chemical stability of our nano-thin film BCY electrolyte can be more vulnerable to reduction to Ce^{3+} than bulk BCY under fuel cell operating conditions due to a higher surface-to-volume ratio, which increases the relative

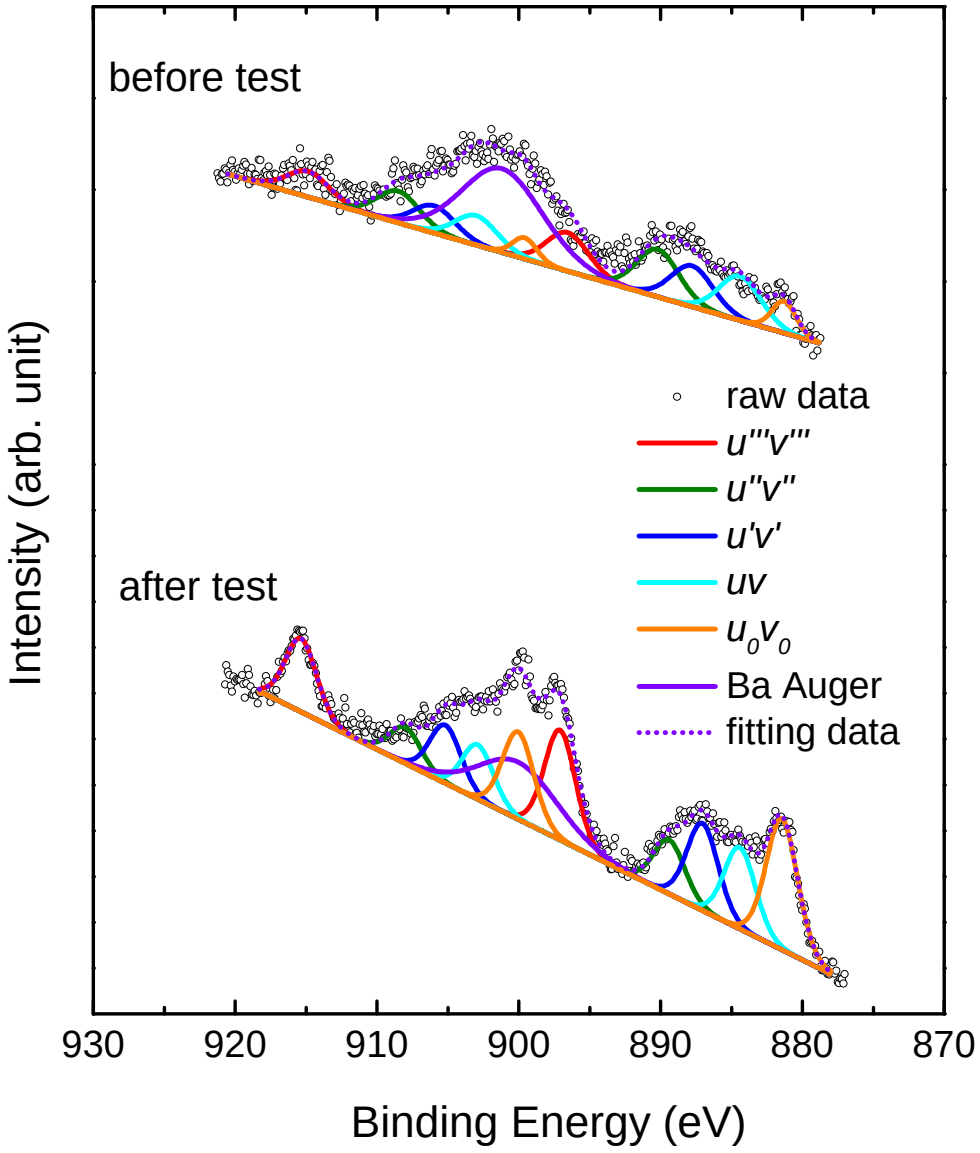

FIGURE 3.8: XPS spectra of Ce 3d for the BCY electrolyte before and after fuel cell test at 400 °C.

Table 3.2: Fitted curves and calculated concentration of the characteristic XPS lines for Ce^{4+} and Ce^{3+}.

Oxidation states	Peak	Before test			After test (400 °C)		
		Position (eV)	% Concentration		Position (eV)	% Concentration	
Ce^{4+}	u'''	914.86	9.91	68.75	915.36	11.52	52.86
	v'''	896.56	10.37		897.09	12.06	
	u''	908.50	12.26		907.99	5.70	
	v''	890.20	12.84		889.39	5.95	
	u	903.00	11.42		902.89	8.61	
	v	884.40	11.95		884.41	9.02	
Ce^{3+}	u'	905.98	10.55	31.25	905.18	9.18	47.14
	v'	887.78	11.05		887.04	9.61	
	u_0	899.59	4.71		900.04	13.85	
	v_0	881.29	4.94		881.45	14.5	

exposure to CO_2 and H_2O. We noticed that most of the cracks in the electrolyte initiated from the cathode surface (Figure 3.3(b)), possibly due to the water vapor produced at the cathode side during fuel cell operation and promoted the reaction in equation (3.1). It is reported that in the presence of moisture in the environment, the decomposition kinetic of $BaCeO_3$ is controlled by the diffusion of water into the perovskite lattice [54]. In our case of nano-thin film electrolyte, since the diffusion pathway is much shorter than that in a bulk electrolyte, the decomposition kinetics is controlled by the contact interface between the BCY electrolyte and moisture environment, as seen from SEM images that the cracks seem to propagate from the electrolyte surface to the center. The possible decomposition mechanism of thin film BCY electrolyte can be understood as an interface-controlled process: the gaseous reactants are in contact with BCY surface and the corrosion reactions (3.1) and (3.2) occur. The products, $BaCO_3$, $Ba(OH)_2$ and CeO_2 formed at electrolyte surface, changed the intrinsic stress level of the pristine free-standing BCY thin film (shown in XRD analysis, Figure 3.4 and Table 3.1), resulting in

cracks formation at the surface. The decomposition of BCY did not occur over the entire surface but only at certain spots to form the cracks due to the partial coverage of surface by porous Pt electrode to block the exposure to water and CO_2. The nanoscale thickness of BCY electrolyte could have accelerated the corrosion processes. Thus, the intrinsic instability of ceria-based BCY electrolyte, together with the higher relative exposed surface area of a nano-thin film, has rapidly deteriorated the fuel cell performance of BCY μ-SOFCs.

3.4 Chemical Stable BCZY-based μ-SOFCs

Based on the chemical stability study of BCY based proton-conducting electrolytes, it is founded that the chemical stability of electrolyte is critical to the μ-SOFCs. Even though BCY has a higher conductivity over BZY electrolyte, poor chemical stability made it not qualify to be a potential electrolyte candidate for μ-SOFCs. In order to make a compromise between the high chemical stability of BZY and high conductivity of BCY, researchers has found a co-doped electrolyte BCZY with Zr and Ce showing promising chemical stability and ionic conductivity [32, 42, 46]. Thus this section will present the fabrication and testing of BCZY-based μ-SOFCs.

The proton conducting μ-SOFC with BCZY electrolyte has the same structure as previous described BZY and BCY-based SOFC. Figure 3.9 shows the cross-sectional structure of BCZY μ-SOFC after fabrication. The BCZY electrolyte,

which was sandwiched between two porous Pt electrodes, can be clearly identified from the image. Nanoscale BCZY electrolyte was deposited by PLD while the porous Pt electrodes were deposited on both sides of the BCZY electrolyte by sputtering. The thickness of BCZY electrolyte was around 100 nm, while the Pt electrodes were about 50 nm thick. The porous structure ensures a higher triple phase boundary (TPB) density when compared with dense electrode. The electrolyte layer was dense enough to be gas tight, as there are no notable cracks or pinholes formed. Similar to BZY and BCY ceramic membranes, BCZY electrolyte also shows a columnar structure along the vertical structure. The columnar electrolyte would reduce the resistance when ionic transporting through the grain boundaries, as the grain boundary density was minimized across the electrolyte membrane.

Fuel cell performance of BCZY μ-SOFC was conducted in a temperature controlled μ-SOFC test chamber with dry H_2 (20 *sccm*) as the fuel and ambient air as oxidant. The measuring temperature was set from 300 to 400 °C. Representative *I-V-P* curves are plotted in Figure 3.10 and the OCV and peak power density are summarized in Table 3.3. The minimum testing voltage was set into 0.1 and 0.2 V in order to avoid the possible Pt degradation in high current density region. The smooth curves indicate that the fuel cell was chemical stable and the testing environment was constant.

Table 3.3: Summary of BCZY SOFC performance

Temperature (°C)	OCV (V)	Power density (mW/cm^2)
300	0.969	27.4
350	0.969	53.9
400	0.983	88.3

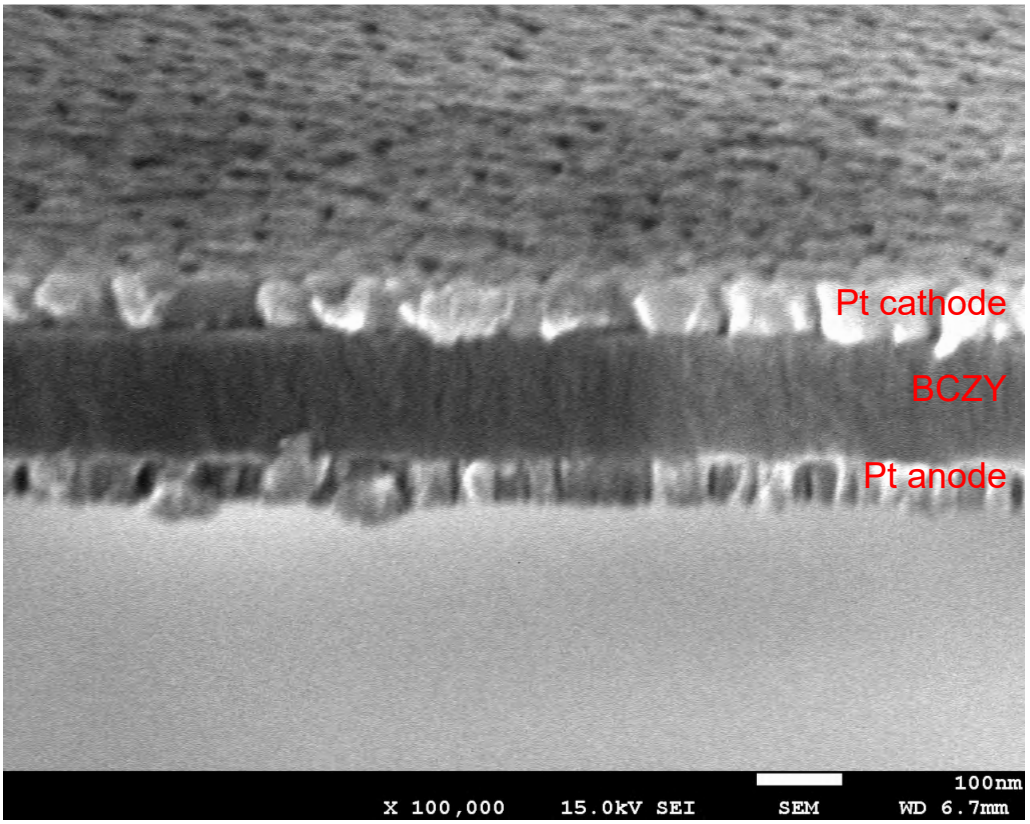

FIGURE 3.9: FE-SEM image of cross-sectional view of a proton-conducting μ-SOFC with BCZY electrolyte.

Unlike BCY μ-SOFC, the OCV of BCZY cells was maintained around 1.0 V at various testing temperatures. It means that the BCZY electrolyte was sufficiently dense enough and no electron leakage was appeared. Peak power densities were 27.4, 53.9, and 88.3 mW/cm^2 at 300, 350 and 400 °C, respectively. The output power densities are greatly enhanced compared with BCY-based μ-SOFC. At 400 °C, the peak power density is nearly 3 times of BCY μ-SOFC. Both increased OCV and power density indicated that by introducing Zr into BCY electrolyte, the fuel cell performance would have great improvement. However, the maximum power density is still lower than BZY μ-SOFC due to the un-optimized depositions of BCZY electrolyte. The chemical stability of BCZY electrolyte was further confirmed by XRD patterns (Figure 3.11). Although the performance characteristics

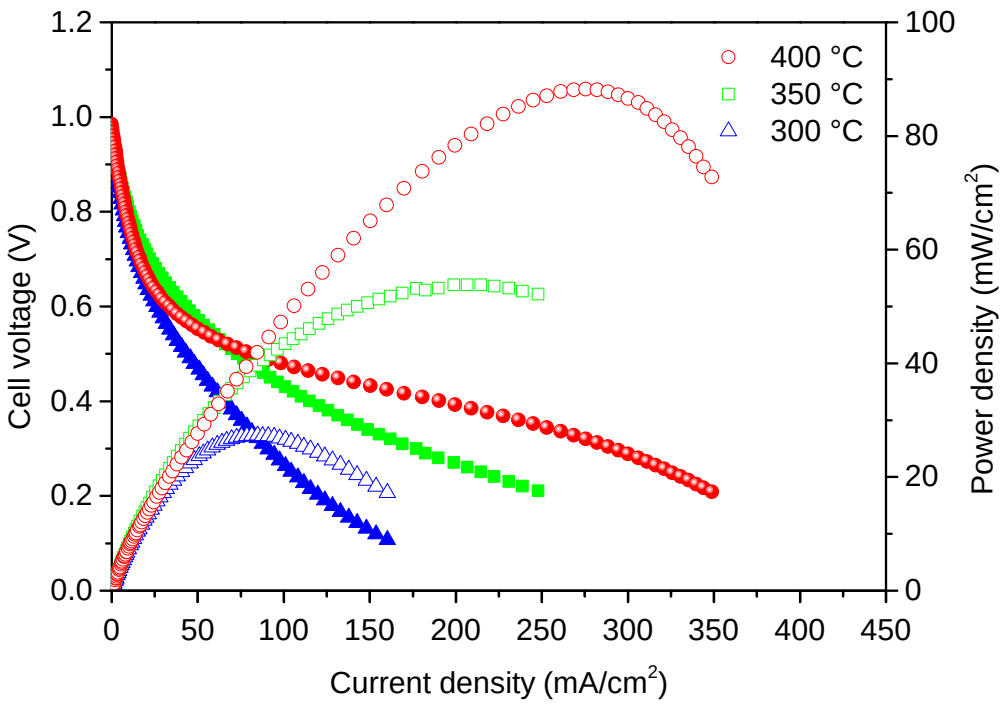

FIGURE 3.10: I-V-P curve of SOFC with BCZY electrolyte tested with H_2 at different temperature of 300, 350, and 400 °C.

of BCZY-based fuel cells are still not as high as expected, the high conductivity and chemical stability of BCZY are very encouraging and imply that cerium-based proton conducting electrolyte is promising for low temperature SOFCs.

3.5 Chapter Summary

In this chapter, we have gained direct evidence of the chemical instability of nanoscale BCY thin film as an electrolyte for micro SOFCs. The μ-SOFC showed a decreasing OCV with increasing operating temperature due to the chemical instability in fuel cell operating environments. Visible vertical cracks were induced from reactions with CO_2 and H_2O vapor that expanded the BCY lattice, leading

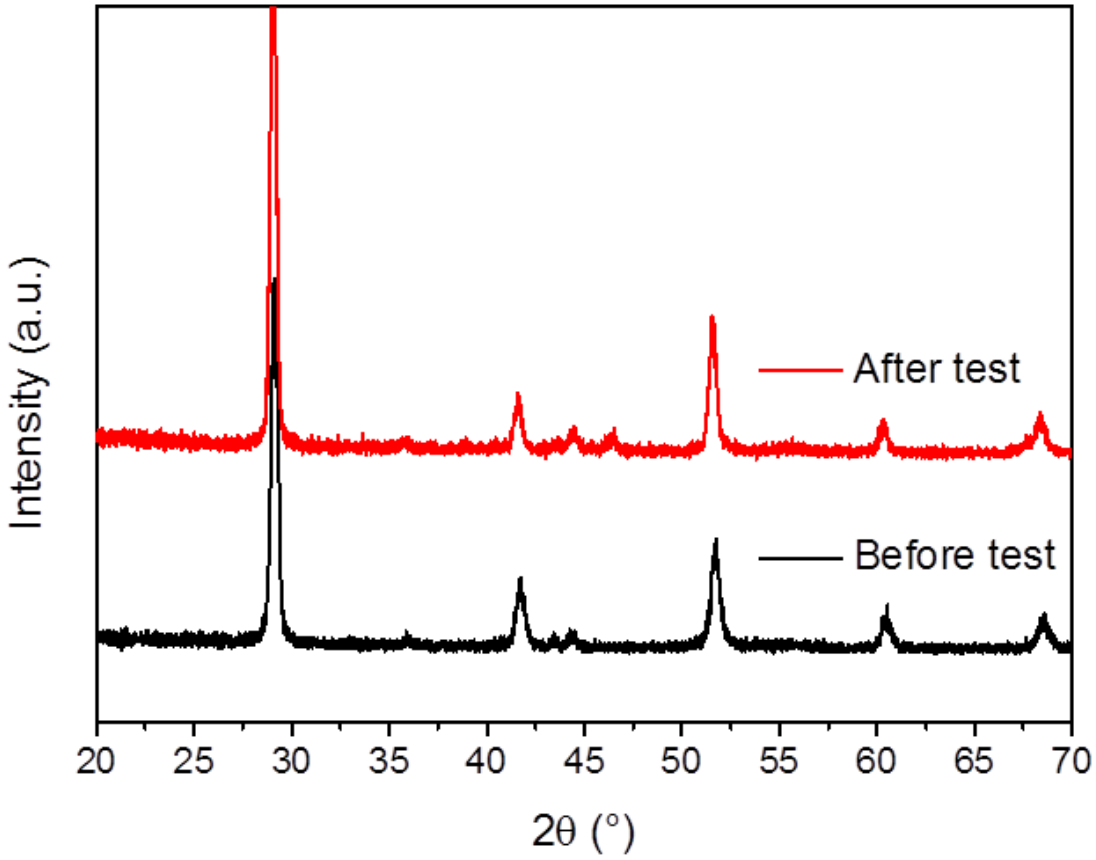

FIGURE 3.11: XRD patterns of BCZY electrolyte before and after fuel cell test at 400 °C.

to an insufficient gas separation of fuels and air. Unlike bulk BCY at high temperatures where only the reaction with CO_2 is significant, the reactions of nano thin film BCY with CO_2 and H_2O are both active at temperature between 300 to 400 °C. The reduction of Ce^{4+} into Ce^{3+} in BCY induced the electronic conduction that also resulted in the decrease of OCV.

In order to enhance the performance of cerium-based ceramic electrolyte, zirconium was added to BCY target. Both the OCV and fuel cell performance of BCZY SOFC have great improvement compared with BCY μ-SOFC. The maximum power density has increased to 89 mW/cm^2 at 400 °C, which is nearly 3 times of BCY result. The OCV was maintained at around 1.0 V, showing that a

chemical stable and dense electrolyte has been successfully fabricated by PLD. Zr stabilized cerium-based electrolyte would be an effective way to enhance the chemical stability of BCY, leading to a promising fuel cell performance enhancement for low temperature SOFCs.

Chapter 4

Proton-conducting SOFCs with Improved Cathode Reactions by a Nanoscale GDC Interlayer

4.1 Introduction

μ-SOFCs using nanoscale thin film electrolytes have shown great promise as portable power sources because of their high performance at drastically reduced operating temperatures [3]. By minimizing the electrolyte thickness from tens of micrometers scale down to sub-micrometer scale, the Ohmic resistance of conventional oxygen ion-conducting electrolytes such as yttria-stabilized zirconia (YSZ) decreased proportionally with thickness, which enabled the high cell performance

Part of this chapter is reprinted from *Scientific Reports*, Vol 6, Yong Li, et al., "Proton-conducting micro solid oxide fuel cells with improved cathode reactions by a nanoscale thin film gadolinium-doped ceria interlayer". DOI: 10.1038/srep22369

at temperatures lower than 500 °C [10, 11, 44, 79–81]. As the Ohmic resistance was minimized, the most rate-limiting process among the entire cell reactions has shifted to the cathode polarization, since the thermally-driven oxygen reduction reaction (ORR) kinetics at the cathode become much more sluggish at such low temperature range [19]. Therefore, improving the kinetics of cathodic reactions or the selection of catalytically more active cathode materials is currently the most critical issue in further enhancing the performance of such promising devices.

Among the reported μ-SOFCs, quite a few works have shown the impressive performance using oxygen ion-conducting electrolytes such as YSZ, gadolinium-doped ceria (GDC), or with multiple-layer configurations like GDC/YSZ bilayer electrolyte [10, 11]. However, for μ-SOFCs to operate at their targeted temperature regime, which is usually below 500 °C, proton-conducting oxides can be more suitable choices as electrolyte materials since they usually possess better ionic conductivity than oxygen-ion conductors at low temperature due to lower activation energy of proton conduction [4]. It should be expected that the already impressive performance of μ-SOFCs reported can be further improved if the oxygen ion-conducting electrolyte is replaced by proton-conducting electrolyte while remaining the other cell components such as porous metal catalytic electrodes unchanged. Nevertheless, to date, among the limited number of reports on μ-SOFCs using the most common proton-conducting electrolytes (μ-H-SOFCs hereafter) like yttrium-doped barium zirconate (BZY), the peak power densities reported were still much lower than those using zirconia- or ceria-based oxygen ion-conducting electrolytes (μ-O-SOFCs hereafter). As summarized in Table 2.1, the highest peak

power densities attainable for μ-H-SOFCs were only 140 mW/cm^2 at 400 °C [48] and 186 mW/cm^2 at 450 °C [37]. For the reported high performance μ-O-SOFCs, the highest peak power densities reported were closer to or over 1 W/cm^2 at 450 °C [11, 80, 81].

The yet impressive performance of μ-H-SOFCs may originate from the poor cathode configuration that provides insufficient reaction sites on such type of nano thin film fuel cells. Figure 4.1a shows the typical cathode/electrolyte/anode cross-sectional schematics of the μ-H-SOFC, which has a nano thin film BZY electrolyte sandwiched by two porous thin film Pt electrodes. Unlike conventional SOFCs, the cathode/electrolyte interface of a μ-SOFC is only connected two-dimensionally, which means the triple phase boundaries for the ORR is only limited to the planar interface between Pt cathode and oxide electrolyte. When the electrolyte is changed from an oxygen ion conductor to a proton conductor, in addition to the existing ORR, the water evolution reaction also shifts from anode to cathode, making the already complex cathode reactions even more complicated. In BZY μ-H-SOFCs, the reduced oxygen ion may only meet the proton transported from the anode through BZY near the triple-phase boundary lines at the interface between Pt cathode and BZY (red line in Figure 4.1a), and these are likely only where the water evolution reaction can take place. Therefore, it is likely that the performance of μ-H-SOFCs has been limited by the confined reaction zone that resulted in high cathodic polarization resistance. In this regard, modifying the interface between Pt and BZY to allow the cathodic reactions to take place over an extended zone is expected to effectively improve the cathode kinetics and increase

the cell power performance. Among studies of regular proton-conducting electrolyte SOFCs (H-SOFCs) that operate at intermediate temperature range (500 to 650 °C), the search of suitable cathode materials to accommodate the complex cathode reactions is also a prevailing topic [82–85]. One of the most promising categories of cathode is the triple-conducting materials, which are materials having simultaneous electronic, oxygen ionic, and protonic conduction properties [86]. A triple-conducting cathode provides more reaction sites for both the ORR and water evolution reaction to take place that is believed to effectively decrease the cathode polarization resistance, and the cell performances using such cathode material are indeed impressive [83]. To apply such concept to μ-H-SOFCs, adding an interlayer between the cathode and electrolyte, or the so-called bi-layered electrolyte, can be an effective method.

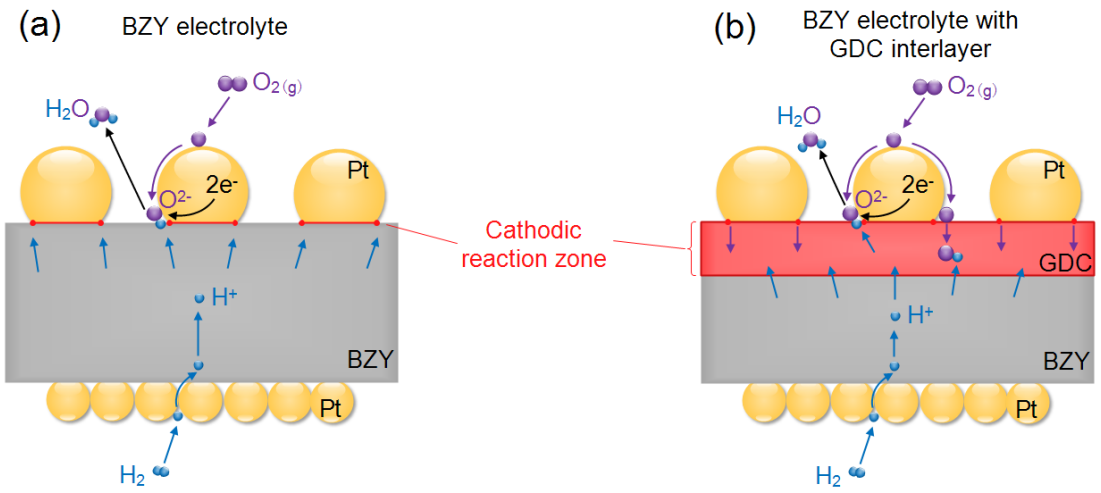

FIGURE 4.1: Schematics of μ-H-SOFCs with possible oxygen reduction reaction and water evolution reaction zone at the cathode/electrolyte interface. (a) The cell with platinum cathode in contact directly with BZY electrolyte, and (b) the cell with platinum cathode in contact with the GDC interlayer on top of the BZY electrolyte.

For μ-O-SOFC, the concept of bi-layered electrolytes or the cathode/electrolyte

interface modifications have been demonstrated to effectively improve the cathode kinetics. A catalytically superior material for ORR, such as doped-ceria [10, 11, 87], can be inserted between the porous metallic cathode and the main electrolyte, which serves as a good cation diffusion barrier [88] and improves the ORR reaction kinetics [89, 90]. Results from quantum mechanical simulation also show the very low oxygen incorporation energetics for doped ceria at cathode/-electrolyte interface to be 0.07 eV, which is much lower than the 0.38 eV of YSZ [91].

To apply the bi-layer electrolyte concept to μ-H-SOFCs for better cathode reaction kinetics, GDC can still be a good choice to accommodate the complex cathode reactions. The Ga doping in ceria gives the highest oxygen diffusion coefficient than ceria doped with other dopants such as Y, Sm, and La [92]. More importantly, evident proton conductivity at temperatures lower than 400 °C was also demonstrated [93–96]. The mixed oxygen ion and proton-conducting property allows both the oxygen ions and protons to transfer into the GDC layer, and therefore it is likely to extend the water formation and evolution zone from the confined TPB lines (Figure 4.1a) into part of or the entire GDC layer (Figure 4.1b).

Therefore, the purpose of this work is to demonstrate the concept of adding a GDC interlayer which is catalytically more active and is a mixed oxygen ionic and protonic conductor, in order to improve the chronically poor performance of μ-H-SOFCs. An 8 nm thin GDC layer was deposited on top of BZY proton-conducting

electrolyte to serve as a cathode interlayer for μ-H-SOFCs. Significant enhancement of cathode performance and fuel cell power density in the silicon-based μ-H-SOFC was obtained with the addition of GDC interlayer. The electrochemical impedance and fuel cell performance of the fabricated μ-H-SOFCs with and without the GDC interlayer was characterized to understand the effect of such cathode interlayer on the cathode kinetics behavior.

4.2 Experimental Methods

4.2.1 Electrolyte Deposition and Fuel Cell Fabrication

BZY electrolyte and the GDC cathodic interlayer were both deposited by an ultra-high vacuum PLD/MBE system (PVD Products, USA) equipped with a 248 nm KrF excimer laser (Lambda Physik, Germany). Before the deposition, the chamber was evacuated to ultra-high vacuum of $< 10^{-8}$ Torr and then the free-standing substrates were heated up to desired deposition temperature of 800 °C with a heating rate of 25 °C/min. The distance between the target and substrate was kept at 80 mm. When reaching the set deposition temperature, pure oxygen gas was introduced into the chamber to maintain a deposition pressure of 1 mTorr, which would ensure oxygen stoichiometry of the deposited sample. Sintered $BaZr_{0.8}Y_{0.2}O_{3-\delta}$ pellet target was ablated by a pulsed laser with a fluence of 3.0 J/cm^2 at a repetition rate of 10 Hz for 30 minutes to fabricate BZY electrolyte thin film. The GDC cathodic interlayer was deposited subsequently by ablating a sintered $Ce_{0.9}Gd_{0.1}O_{1.95-\delta}$ for 4 minutes with the same deposition

parameters. After thin film deposition, samples were cooled down to room temperature with a cooling rate of 25 °C/min. The μ-SOFCs are fabricated through a typical Si-based micro-machining process as previously reported [10, 47]. The patterned Si_3N_4/Si with free-standing Si_3N_4 membrane ($150\mu m \times 150\mu m$) was fabricated as the supporting layer for electrolyte deposition. After the deposition of BZY electrolyte and GDC interlayer by PLD, the Si_3N_4 supporting layer was removed by relative ion etching (RIE) with CF_4 gas, resulting in a free-standing nanoscale electrolyte. Porous platinum thin films are deposited on both sides of the BZY/GDC electrolyte via RF sputtering technique with Ar pressure of 30 mTorr at room temperature to achieve porous anode and cathode.

4.2.2 Crystallinity and Morphology Characterization

The phase and crystal structure of BZY and GDC films were characterized by GIXRD system equipped with a CuKα X-ray source (PANalytical Empyrean XRD, Netherlands) operating at beam intensity of 40 kV and 40 mA. The glancing angle X-ray was incident at an angle of 0.5°. Cross-sectional micro-structure of the fuel cell was characterized by field-emission scanning electron microscopy (FESEM, JSM-7600F, JEOL, Ltd., Japan) and transmission electron microscopy (TEM, JEM-2100, JEOL, Ltd., Japan).

4.2.3 Fuel Cell Performance Characterization

Fuel cell performance was tested with a customized test station for the measurement of silicon-based μ-SOFCs. The μ-SOFC chip was fixed on a stainless steel chamber with gold gasket for sealing. The furnace temperature was elevated to the set testing temperature with a heating rate of 10 °C/min. An Au coated tungsten probe, which was connected to a micro-positioner, was put in contact with the porous platinum cathode for current collection. Dry hydrogen fuel with a flow rate of 20 sccm was supplied to the anode side, and the cathode side was exposed to the ambient air. The fuel cell performance was measured by obtaining the current-voltage (I-V) polarization curves at temperatures from 350 to 425 °C. For the data collection of both the polarization curves and electrochemical impedance spectroscopy (EIS), a Solartron 1470E potentiostats system and a 1255B Frequency Response Analyzer (FRA) were connected to the anode and cathode sides. The obtained EIS curves were fitted with equivalent circuit models using Zview software (Scribner Associates).

4.3 Results and Discussion

4.3.1 Microstructure of the GDC/BZY Electrolyte

Figure 4.2 shows the XRD patterns of BZY electrolyte with and without GDC cathodic interlayer. The BZY electrolyte layer has a polycrystalline structure with a preferred orientation of (011). All of the peaks were indexed to the standard BZY

PDF card 96-720-2180, meaning a well-crystallized BZY film at the deposition temperature of 800 °C. For the electrolyte with GDC interlayer, additional GDC peaks were clearly observed and well-matched with the standard GDC pattern of PDF 00-046-0508. The relatively low intensity of GDC peaks was due to the much smaller thickness of GDC interlayer (8 nm) than BZY (75 nm). No additional phase was observed from the bi-layer electrolyte, meaning no reaction between BZY and GDC occurred during the deposition at 800 °C.

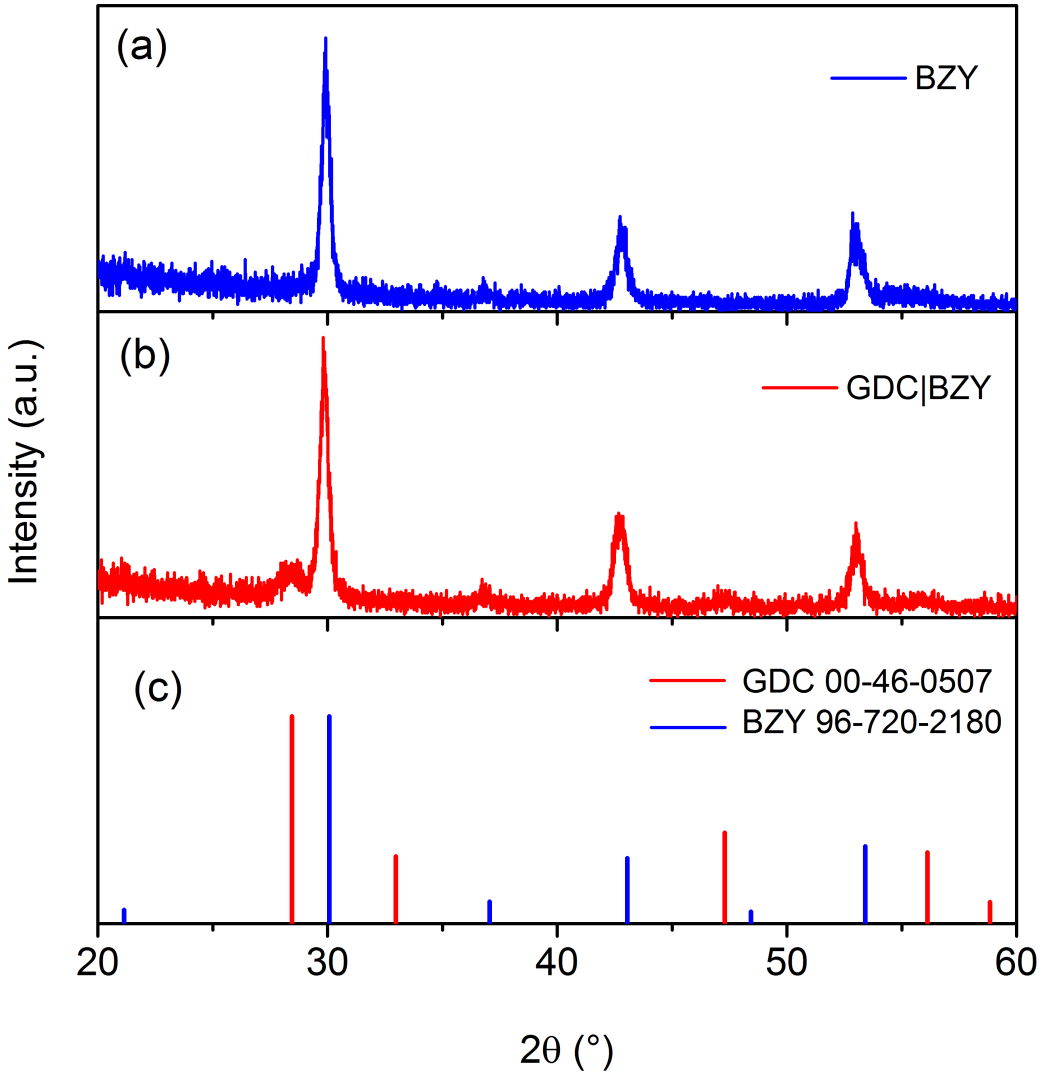

FIGURE 4.2: XRD patterns of BZY thin film electrolytes (a) with and (b) without GDC interlayer, with the reference peaks indices for BZY and GDC in (c).

The FESEM cross-sectional images of both the μ-H-SOFCs having the BZY electrolytes with and without GDC interlayer are shown in Figure 4.3. The dense BZY electrolytes in both cases were 75 nm in thickness and sandwiched by the porous Pt cathode and anode of 100 nm and 60 nm in thickness, respectively.

The cross-sectional TEM characterizations were performed for the GDC/BZY bilayer electrolyte to verify the crystallinity and the microstructures (Figure 4.4). Fully crystallized BZY electrolyte and GDC interlayer both had columnar grains with vertical grain boundaries parallel to the ion transportation direction (Figure 4.4a), which minimizes the cross grain boundary resistance during proton conduction [38]. The thickness of BZY electrolyte and GDC interlayer were confirmed to be 75 nm and 8 nm, respectively (Figure 4.4b). No additional phase was visible in between the BZY and GDC layers, meaning a good chemical compatibility and stability between these two layers at the 800 °C deposition temperature, which is in agreement with the XRD results. Therefore, no reaction is expected to occur during the μ-H-SOFC operation because of the much lower operating temperature (below 500 °C) than the deposition temperature. Although a large mismatch of lattice constant exists between BZY (0.42 nm) and GDC (0.54 nm), the grain boundaries of the GDC interlayer were aligned to the grain boundaries of the underneath BZY during the grain growth from PLD deposition. The grain alignment introduced a compressive stress to the GDC interlayer, which resulted in a high density of dislocations and lattice distortion, as shown in Figure 4.4c. The dislocations not only presented at the vicinity of GDC/BZY interface, but also extended through the GDC grains. The inversed fast Fourier transform (FFT) image in

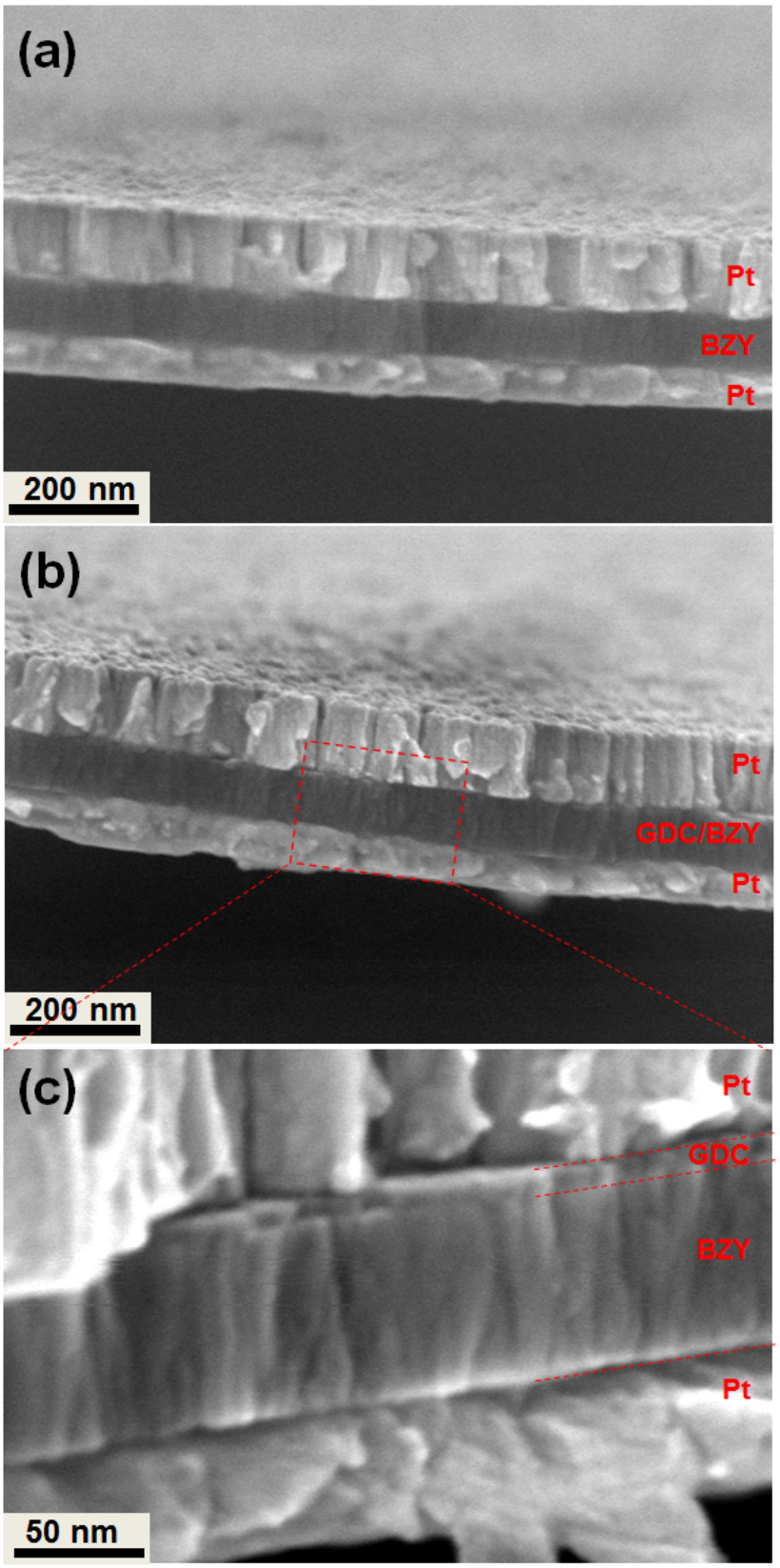

FIGURE 4.3: FESEM cross-sectional images of the free-standing electrolyte membranes with platinum cathode and anode. (a) BZY electrolyte; (b) BZY electrolyte with GDC cathodic interlayer, and (c) magnification of (b).

Figure 4.4d clearly shows the existence of dislocations and lattice distortion by the compressive strain between BZY and GDC layers.

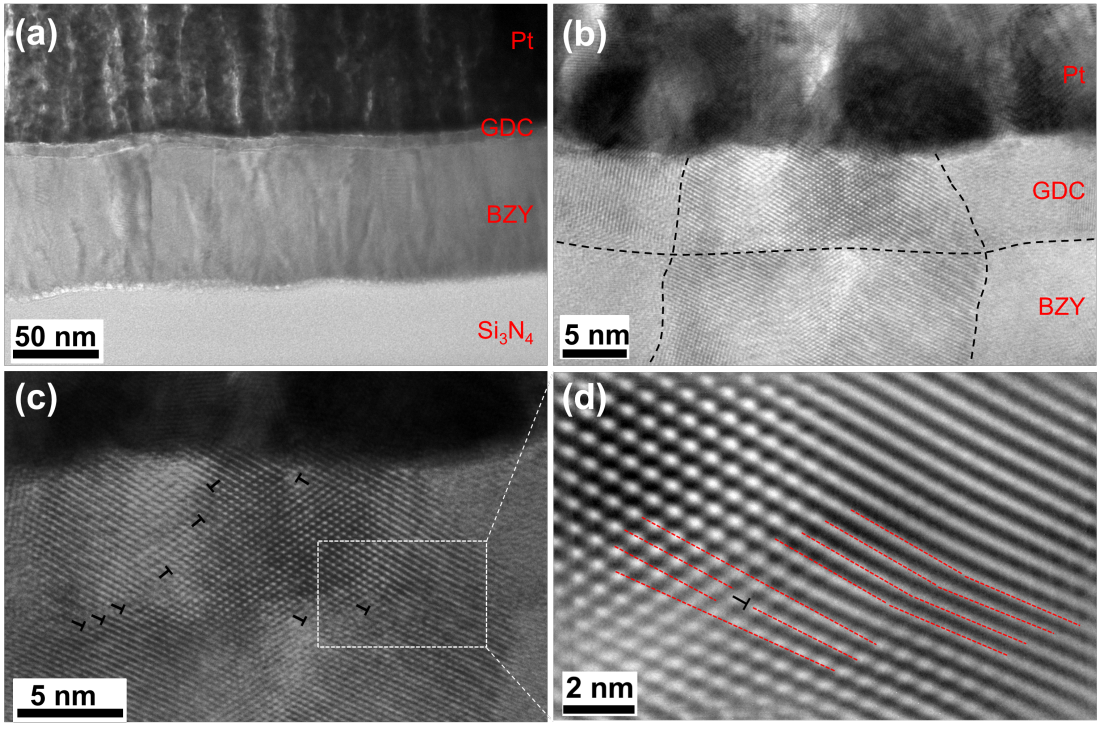

FIGURE 4.4: Cross-sectional TEM characterizations near the Pt/GDC-interlayer/BZY-electrolyte at the non-freestanding region of the membrane on a SiN/Si substrate. (a)Cross-sectional view of the heterostructure of Pt/GDC/BZY/SiN; (b) High resolution TEM image of the GDC interlayer and interface. The GDC/BZY interface and grain boundaries are indicated by dashed lines; (c) A high density of dislocations is observed in the GDC interlayer, with some of them marked by the labels "⊥"; (d) The corresponding inverse FFT calculated image of the dotted region in (c). The dashed lines are guides indicating the dislocation lines and the existence of lattice distortion.

4.3.2 Electrochemical Characterization

Figure 4.5 shows the polarization curves for the μ-H-SOFCs using BZY electrolytes with and without the GDC cathode interlayer. Both fuel cells showed stable and high OCVs in the range of 0.98 to 1.07V close to the theoretical thermodynamic value of 1.1V, indicating that dense and pinhole-free electrolytes remained intact during the cell operation. The maximum power densities for the cell using BZY

electrolyte were 51, 93 and 206 mW/cm^2 at 350, 375, and 400 °C, respectively. For the cell with GDC interlayer, the maximum peak power densities further increased up to 106, 187, 274 mW/cm^2 at 350, 375, 400 °C, and reached 446 mW/cm^2 at 425 °C. The peak power density values of both the cells with and without GDC interlayer were all higher than the reported values of μ-H-SOFCs at the same testing temperatures, as summarized in Table 2.1.

To confirm the improved reaction kinetics at the cathode side, the EIS curves of both the cells with and without the GDC interlayer were studied at 350 to 400 °C (Figure 4.6). The first intercept on the real axis at high frequencies represents the Ohmic resistance R_Ω, and the second intercept on the real axis at low frequencies corresponds to the total resistance of the cell [97]. For the polarization resistance Rp, two distinguished arcs can be identified, where one has the characteristic frequency at the high frequency range (HF, 10^5 Hz) and the other at medium frequency range (MF, $10^2 - 10^3$ Hz). The EIS curves were fitted using the equivalent circuit model of two parallel R and CPE (constant phase element) and one resistor connected in series, as shown in the inset of Figure 4.6. The values extracted from the curve fitting were summarized in Table 4.1. The values of (R1, CPE1) and (R2, CPE2) corresponded to the HF and MF arcs, respectively. Each CPE has a CPE-T, which is related to the relaxation capacitance, and a CPE-P, which reflects the displacement of the center of the arc from the real axis [98].

As summarized in Table 4.1, the total polarization resistances R_p of the cell without GDC interlayer were 11.899, 7.045, and 3.660 Ωcm^2 at 350, 400, and 450 °C, respectively, and the cell with GDC interlayer decreased to 4.136, 3.346, and

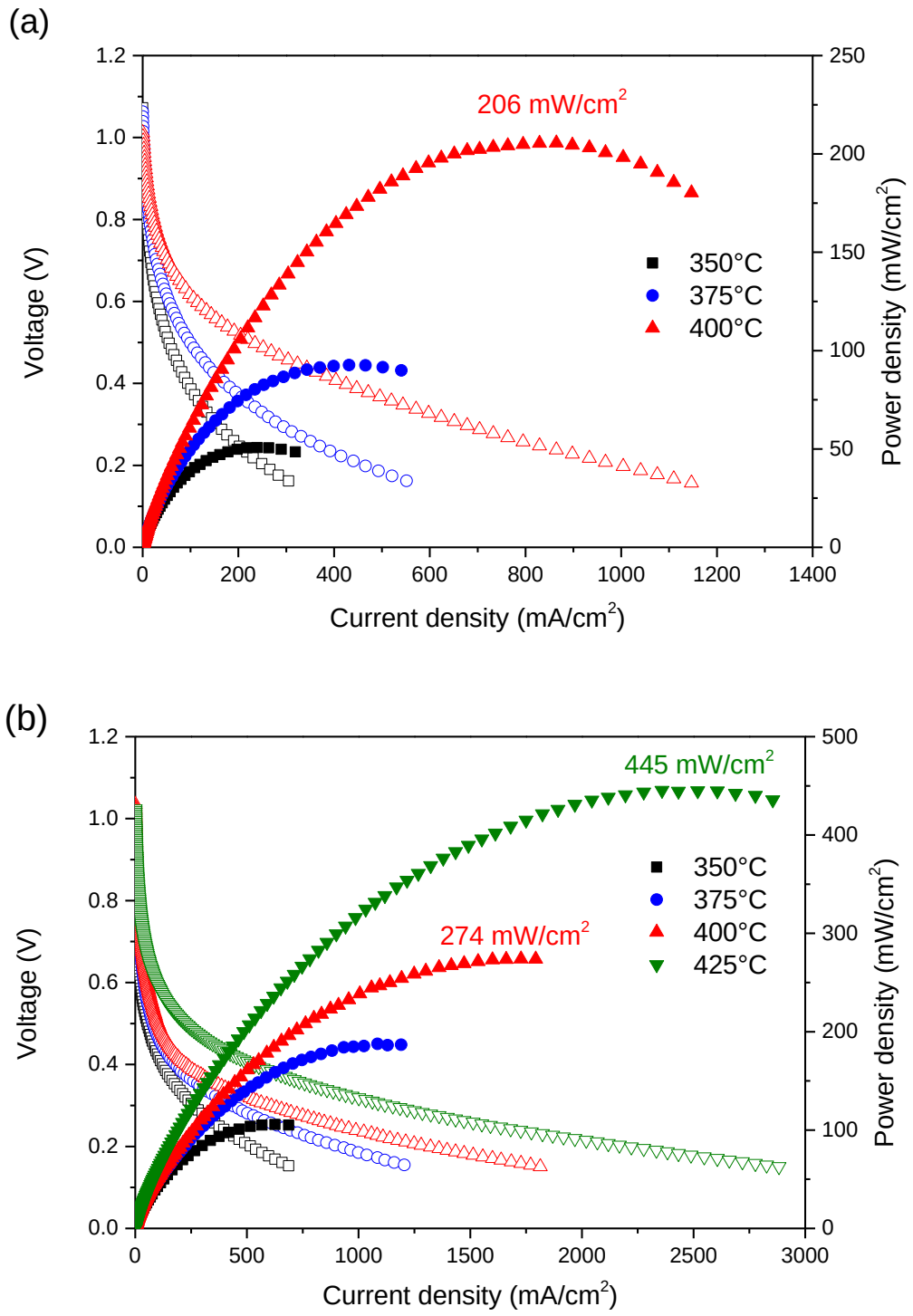

FIGURE 4.5: I-V curves of the μ-H-SOFCs (a) with only BZY electrolyte, and (b) with BZY electrolyte with GDC interlayer at 350 to 425 °C.

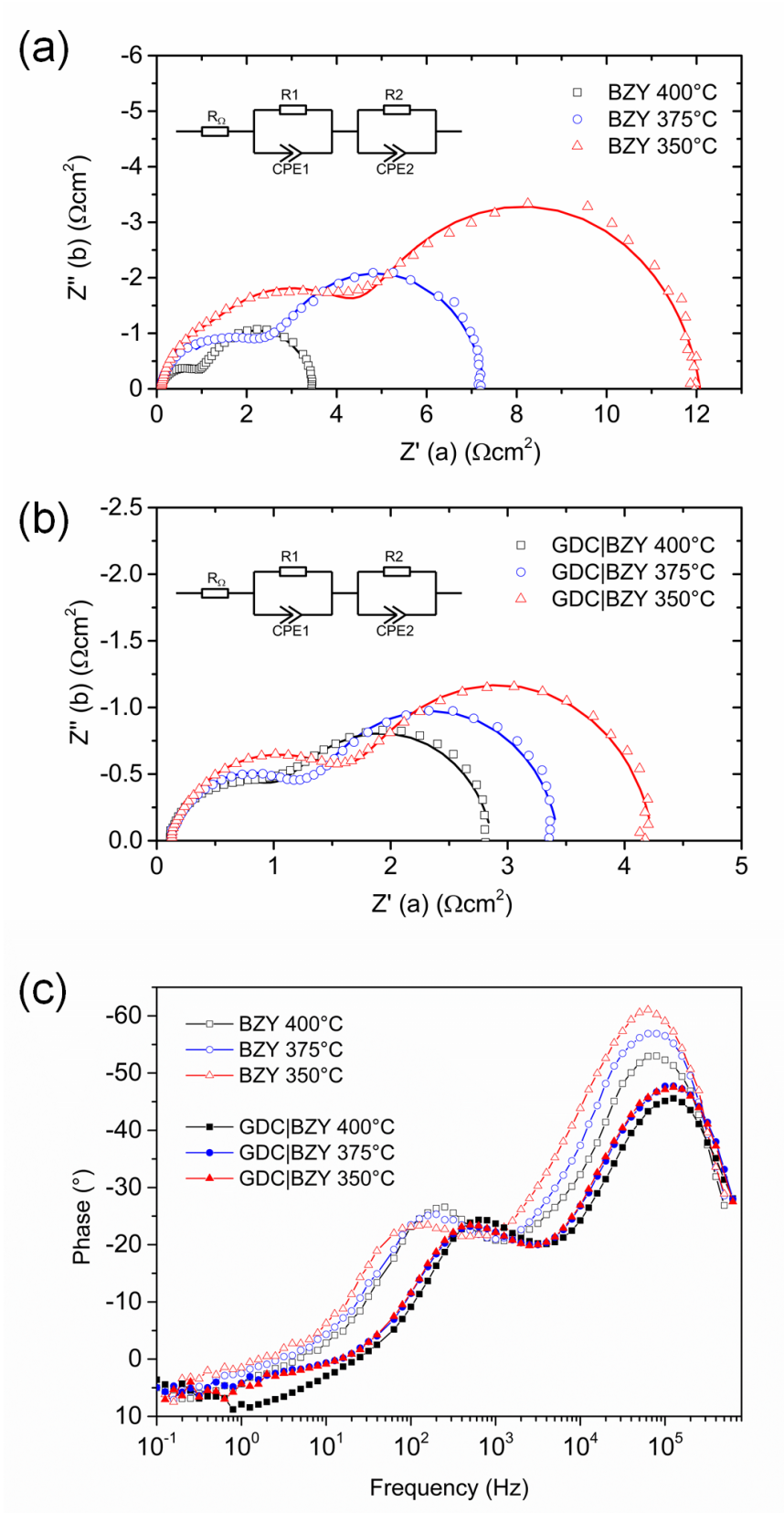

FIGURE 4.6: The Nyquist plots of EIS characterizations of μ-H-SOFCs with (a) BZY electrolyte only, (b) BZY electrolyte with GDC interlayer, and (c) bode plots for both cells.

Table 4.1: Summary of the values extracted from equivalent circuit fitting of the EIS curves at 350, 375, and 400 °C.

Fuel Cell Electrolyte	Temperature (°C)	R_Ω (Ωcm^2)	$R_p = R_1 + R_2$ (Ωcm^2)	HF Semicircle			MF Semicircle		
				R_1(Ωcm^2)	CPE1-T (F)	CPE1-P	R_2(Ωcm^2)	CPE2-T (F)	CPE2-P
BZY	350	0.099	11.899	4.720	7.09E-09	0.872	7.179	2.24E-07	0.779
	375	0.089	7.045	2.463	8.33E-09	0.864	4.582	2.18E-07	0.818
	400	0.085	3.660	1.103	9.06E-09	0.869	2.557	2.07E-07	0.855
GDC/BZY	350	0.131	4.136	1.651	1.57E-08	0.789	2.485	9.83E-08	0.928
	375	0.129	3.346	1.276	1.33E-08	0.809	2.070	8.66E-08	0.933
	400	0.115	2.443	0.997	1.27E-08	0.820	1.776	7.70E-08	0.902

2.443 Ωcm^2 at 350, 400, and 450 °C, respectively. The decreases in R_p means the cathodic reaction was promoted by the additional GDC interlayer. Since the electrolyte and both electrodes were identical for both cells in all of the experiments, the changes in R_p should be due to the presence of GDC interlayer. The Ohmic resistances of the BZY electrolyte cell were 0.085, 0.089, and 0.099 Ωcm^2, and for the GDC/BZY cell the resistances increased slightly to 0.115, 0.129, and 0.131 Ωcm^2 at 350, 375, and 400 °C, respectively, likely due to the additional thickness from GDC and the interface between GDC and BZY. The variations in the Ohmic resistance between these two cells can be negligible since they are relatively small as compared to the value of polarization resistance R_p.

The improved cathode kinetics by the GDC interlayer was furthered identified in the corresponding bode plot of each EIS curve (Figure 4.6c). Two rate limiting steps were observed for both cells with and without GDC interlayer: the proton migration from the electrolyte to the TPBs, which corresponds to the HF resistance, and the oxygen dissociative adsorption and diffusion, which is related to the MF resistance [86]. With the GDC interlayer, the MF resistances were decreased from 7.179, 4.582, and 2.557 Ωcm^2 to 2.485, 2.070, and 1.776 Ωcm^2 at 350, 375, and 400 °C, respectively, corresponding to the slightly depressed MF arc in the bode plot with a frequency shift from 10^2 Hz to 10^3 Hz. The reduced MF resistance means an enhanced oxygen dissociative adsorption process on the GDC surface, which may originate from the high density of grain boundaries and dislocations in the GDC interlayer that provide preferential oxygen incorporation sites for lower interface resistance faster surface exchange kinetics [99–101].

The HF peaks in the bode plot of the cell with GDC interlayer showed more apparent depression than that of the cell with only BZY electrolyte at all the testing temperatures, showing the enhancement of charge transfer process across the cathode/electrolyte interface at the presence of the GDC interlayer. The HF polarization resistances of the cell without GDC interlayer were 4.720, 2.463, and 1.103 Ωcm^2 at 350, 400, and 450 °C, respectively, and the cell with GDC interlayer decreased to 1.651, 1.276, and 0.997 Ωcm^2 at 350, 400, and 450 °C, respectively. The enhanced charge transfer process was originated from the mixed conduction of proton and oxygen ion in the GDC layer, which extended the reactions sites for water formation and evolution process. As depicted in Figure 4.1b, the dissociative adsorbed oxygen ions can transfer from TPBs and surface grain boundaries to the GDC interlayer through oxygen vacancies. When proton reaches to the GDC/BZY interface, it can migrate to the GDC interlayer and react with the oxygen ions presented within the GDC interlayer. Thus, the active regions to facilitate the water formation and evolution are not limited to the interface between Pt cathode and electrolyte, but extend to the GDC interlayer such that the HF resistance was decreased. Although the exact ORR and water evolution reaction mechanisms and pathways within the interlayer are still unclear, it is evident that the combined conduction of both O^{2-} and H^+ has effectively improved the cathodic kinetics, leading to a enhance fuel cell performance at low temperature range for proton-conducting SOFCs.

4.4 Chapter Summary

The complex cathodic reactions in a μ-H-SOFC using BZY as electrolyte were studied by an interface modification with the addition of an 8 nm thin film GDC cathode interlayer. The cathodic polarization resistance was effectively decreased by the additional GDC interlayer between the Pt cathode and BZY electrolyte. A record high peak power density of 445 mW/cm^2 was obtained at 425 °C from the μ-H-SOFC with GDC/BZY bi-layer electrolyte. The EIS analysis of cathodic impedance of the fuel cells showed the enhanced cathodic charge transfer process across the cathode/electrolyte interface with the help of GDC interlayer, suggesting the effective promotion of proton and oxygen ion charge transfer as well as ORR and water evolution reaction between Pt cathode and BZY electrolyte through the GDC interlayer. The mixed oxygen and proton conduction in the GDC interlayer has expanded the ORR sites from a 2-dimentional planar interface between Pt and BZY to the entire GDC interlayer. The findings in this work show that cathodic interfacial modification with GDC interlayer has greatly effects on the performance of μ-H-SOFCs. Further study on fundamental mechanisms into the protonic and oxygen ionic conduction pathways and reaction mechanism within the cathodic interlayer deserves an extensive exploration.

Chapter 5

Nanostructured $Ba_{0.5}Sr_{0.5}Co_{0.8}Fe_{0.2}O_{3-\delta}$ (BSCF) Thin Film Cathode for Low Temperature SOFCs

5.1 Introduction

Proton-conducting ceramic electrolytes have been demonstrated to be promising candidate for low temperature SOFCs due to its lower activation energy and higher ionic conductivity compared to conventional oxygen ion electrolyte such as YSZ [6]. Exceptional fuel cell performances have been achieved with chemical stable protonic conductors such as BZY, BCZY at reduced temperature of 500 °C [85, 102].

In order to further reduce the operating temperature, μ-SOFCs using nanoscale thin film electrolyte would be an efficient way [3, 10, 103, 104]. By thinning the electrolyte thickness from typically micrometers down to tens of nanometers, the charge transport resistance through the electrolyte was significantly minimized, which compensates the loss caused by slow electrolyte kinetics at low temperature (<500 °C).

As operating temperature reduced to lower than 500 °C, the thermally-driven cathode polarization kinetic has become the most rate-limiting process for μ-SOFCs [3]. This is due to the complex oxygen reduction reaction (ORR) process that becomes even more sluggish at lower temperatures. Therefore, in most reported μ-SOFCs using nanoscale electrolyte thin films operating at temperatures below 450 °C, noble metal catalytic cathodes such as sputtered nano-porous platinum or palladium were often adopted to utilize their superior catalytic activities for cathode ORR [3, 11, 44, 105, 106]. The issues of using noble metals are not only the high cost of the raw material, but the high density nanoscale pores within the sputtered porous electrode were also vulnerable to thermally-driven agglomeration, and therefore the high cell performance suffered from poor thermal stability after a short term operation [47, 103, 106]. Therefore, the search for alternative cathode materials that with both thermally stable and catalytically satisfactory is necessary to bring forward the practical application of μ-SOFCs.

In terms of thermal stability of the cathode, a good pool of alternative material choices can be from the conventional oxide cathode materials that are well-studied

for intermediate temperature SOFCs (IT-SOFCs), since oxides usually possess better thermal-morphological stability than metals. Among them, the mixed ionic-electronic conductors (MIEC) cathode, $Ba_xSr_{1-x}Co_yFe_{1-y}O_{3-\delta}$ (BSCF), also often regarded as the benchmark cathode material for IT-SOFCs, can be a good alternative to platinum as a μ-SOFCs cathode material. Unlike platinum, which is a pure electronic conductor and has only effective ORR sites at the gas-electrode-electrolyte TPB interfaces, the BSCF as an MIEC cathode has the effective ORR sites over the entire cathode [107], which allows the application at reduced temperatures with satisfactory ORR catalytic activity.

Although BSCF has been a benchmark cathode material for IT-SOFCs, the application as a cathode for μ-SOFCs operating at temperatures below 450 °C has yet been studied, likely due to the operating temperature for conventional IT-SOFCs is rarely so low. In addition, the cathode activity and chemical stability at temperatures below 500 °C can be poor [108]. So far, the only demonstration of using BSCF cathode in μ-SOFCs was done by Kerman et al [63], where they sputtered a dense BSCF thin film cathode on a free-standing YSZ electrolyte, and obtained a maximum power density of 35 mW/cm^2 at 520 °C. The low cell performance in their work is originated from limiting reaction sites for oxygen reduction to the surface of dense BSCF because the polarization resistance of BSCF cathode at such low temperature depends very much on the surface reaction with oxygen [109]. In other words, a higher surface area exposed to gaseous oxygen ambient can decrease the polarization resistance of the cathode ORR effectively.

In order to improve the performance of BSCF cathode at temperatures below 500

°C, a nanostructured BSCF cathode thin film with increased total surface area exposed to gaseous oxygen was fabricated for the application of low temperature SOFCs. The BSCF thin film cathodes were fabricated by PLD, which is preferred over the previously reported RF sputtering in the control of thin film composition, crystallinity, and morphology. The microstructure and crystallinity of the nanostructured BSCF were characterized with various PLD deposition parameters. The BSCF cathode polarization resistance and its functionality as a cathode for μ-SOFCs at temperature below 500 °C were also characterized under fuel cell operating conditions.

5.2 Experimental Methods

5.2.1 Deposition of BSCF Thin Film

BSCF thin film cathode was deposited by PLD, which is known for being able to preserve the composition between the target material and the deposited film among popular thin film deposition methods. All depositions were performed in a PLD system equipped with a 248 nm KrF excimer laser (Lambda Physik) and a vacuum chamber (KYKY Technology Co., LTD., China) pumped to a base pressure of 110^{-4} Pa. The laser fluence of 3.0 J/cm^2 per pulse was utilized to strike a sintered $Ba_{0.5}Sr_{0.5}Co_{0.8}Fe_{0.2}O_{3-\delta}$ pellet target (Able Targets, Beijing) with a repetition rate of 3 Hz at a target-to-substrate distance of 40 mm. BSCF films were deposited on a silicon substrate coated with a 200 nm-thick insulating Si_3N_4 layer by low-pressure chemical vapor deposition. The silicon substrate was heated

to targeted deposition temperatures (400, 500, 600, and 700 °C) with a heating rate of 20 °C/min, with the chamber being continuously purged with pure oxygen to maintain the desired oxygen partial pressure (1, 10, 20 and 50 Pa). After thin film deposition, the films were cooled to 300 °C with a controlled cooling rate of 10 °C/min, and then naturally cooled to room temperature in the same oxygen environment.

5.2.2 Thin Film Crystallinity and Morphology Characterization

The phase and crystal structure of BSCF films deposited under various parameters were analyzed by GIXRD system equipped with a CuKα X-ray source (PANalytical Empyrean XRD, Netherlands). The surface topographic images were scanned in air by an atomic force microscopy (AFM, Asylum Research MFP3D system, USA) under tapping mode, and the surface morphology was observed by field-emission scanning electron microscopy (FESEM, JSM-7600F, JEOL, Ltd., Japan). Cross-sectional transmission electron microscopy (TEM, JEM-2100, JEOL, Ltd., Japan) observations were carried out to check the grain size and crystallization. The composition and chemical states of deposited films before and after fuel cell test were determined using X-ray photoelectron spectroscopy (XPS, Kratos AXIS Ultra) with a monochromatic AlKα (1486.71 eV) X-ray radiation (15 kV/10 mA).

5.2.3 Thin Film SOFC Fabrication and Electrochemical Characterization

To test the functionality of the nanostructured BSCF thin film as a SOFC cathode at temperatures below 500 °C, BSCF thin film was deposition on a 200 μm-thick (100) single crystal YSZ, with the typical nanoporous Pt thin film deposited by RF sputtering as an anode [110]. A reference sample with nanoporous Pt cathode is fabricated and tested with the same condition. μ-SOFCs with nanostructured BSCF cathodes were also fabricated follow a typical free-standing SOFC process, as described in [10, 47]. The BZY thin film electrolyte and BSCF cathode were deposited by PLD on a free-standing micro-machined Si_3N_4/Si wafer consequently in the same chamber. Porous Pt anode was sputtered after removing the Si_3N_4 supporting layer by dry etching with CF_4 gas. The EIS and fuel cell polarization curves were tested with dry pure hydrogen as fuel and ambient air as oxidant at 425-450 °C using a custom-designed SOFC test station connected to a potentiostat system (Solartron 1470E, UK) and a frequency response analyzer (Solartron FRA 1255B, UK).

5.3 Results and Discussion

5.3.1 Crystallinity and Morphologies of BSCF Thin Films

The deposited BSCF films at substrate temperatures of 500, 600, 700, 800 °C and at different oxygen partial pressures of 1, 10, 20, and 50 Pa but fixed substrate temperature of 700 °C were characterized by XRD, as shown in Figure 5.1. All BSCF thin films had polycrystalline structures well-matched to BSCF standard XRD card JCPDS 055-0563 [63] with partially amorphous features. The crystallinity of BSCF thin film increased with temperature as seen from the sharpened peak shape and increasing heights. The full width at half maximum (FWHM) of the main peak also increased with the oxygen partial pressure during deposition, indicating an increasing grain size.

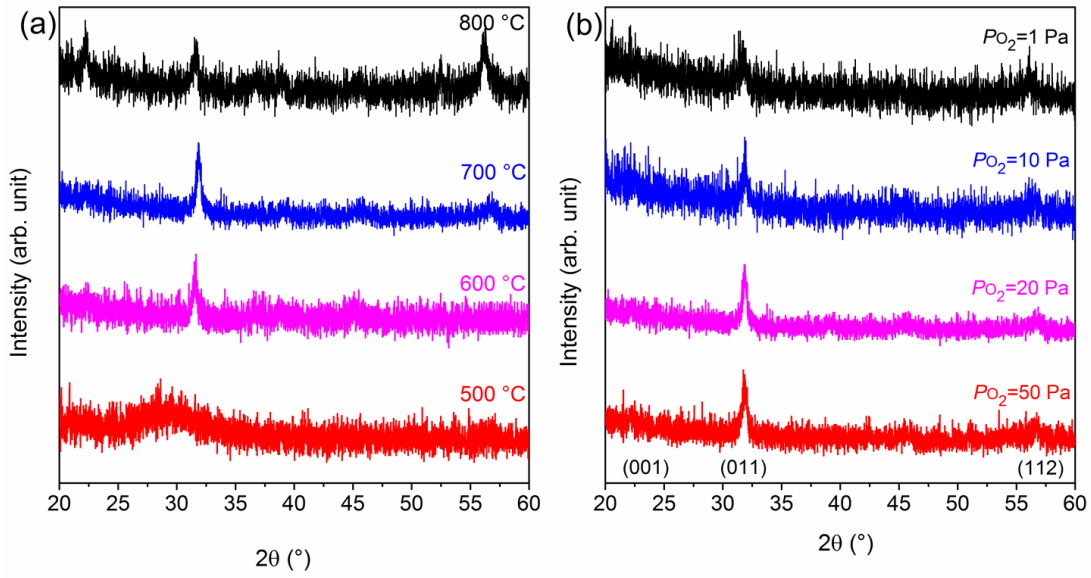

FIGURE 5.1: XRD patterns of BSCF deposited at various (a) substrate temperature and (b) oxygen partial pressures.

Figure 5.2 shows the surface FESEM images of the BSCF thin films deposited at oxygen pressures of 1, 10, 20, and 50 Pa at 700 °C. Since higher chamber pressure gives more collision events that shorten the mean free path, the laser-ablated BSCF particles would deposit less energetically on the substrate and result in loose stacking of the particles [111], i.e. more porosities at higher oxygen pressure. As expected, BSCF film deposited at 1 Pa (Figure 5.2a) shows a relatively smoother surface, while for films deposited at 10, 20, and 50 Pa (Figure 5.2b, c, and d, respectively), the surface showed stacks of flaky BSCF particles with visible pores between them. Moreover, the particle size of deposited films increased with increasing oxygen pressure, with an average size of 82 nm at 1 Pa, 119 nm at 10 Pa, 151 nm at 20 Pa, and 149 nm at 50 Pa, as was characterized by AFM measurement. The increasing particle size with chamber pressure was also reflected in the surface roughness by AFM surface scan, where root mean squared (RMS) roughness increased from 4.6 for 1 Pa to 6.7 for 50 Pa. As the chamber pressure increased to 50 Pa, the flake-like particles started to merge and part of the surface porosity was lost (the area enclosed by dashed line in Figure 5.2d). Therefore, BSCF films deposited at 20 Pa of oxygen chamber pressure at 700 °C was selected for the subsequent μ-SOFCs application.

The cross-sectional TEM image of the BSCF film deposited under 20 Pa oxygen pressure at 700 °C is shown in Figure 5.3. The BSCF thin film with thickness of around 150 nm was clearly seen on the Si_3N_4 insulating layer, which gives the deposition rate of 0.278 $\AA$/pulse. Figure 5.3b shows the high resolution cross-sectional TEM image near the surface of BSCF thin film. The film showed a polycrystalline

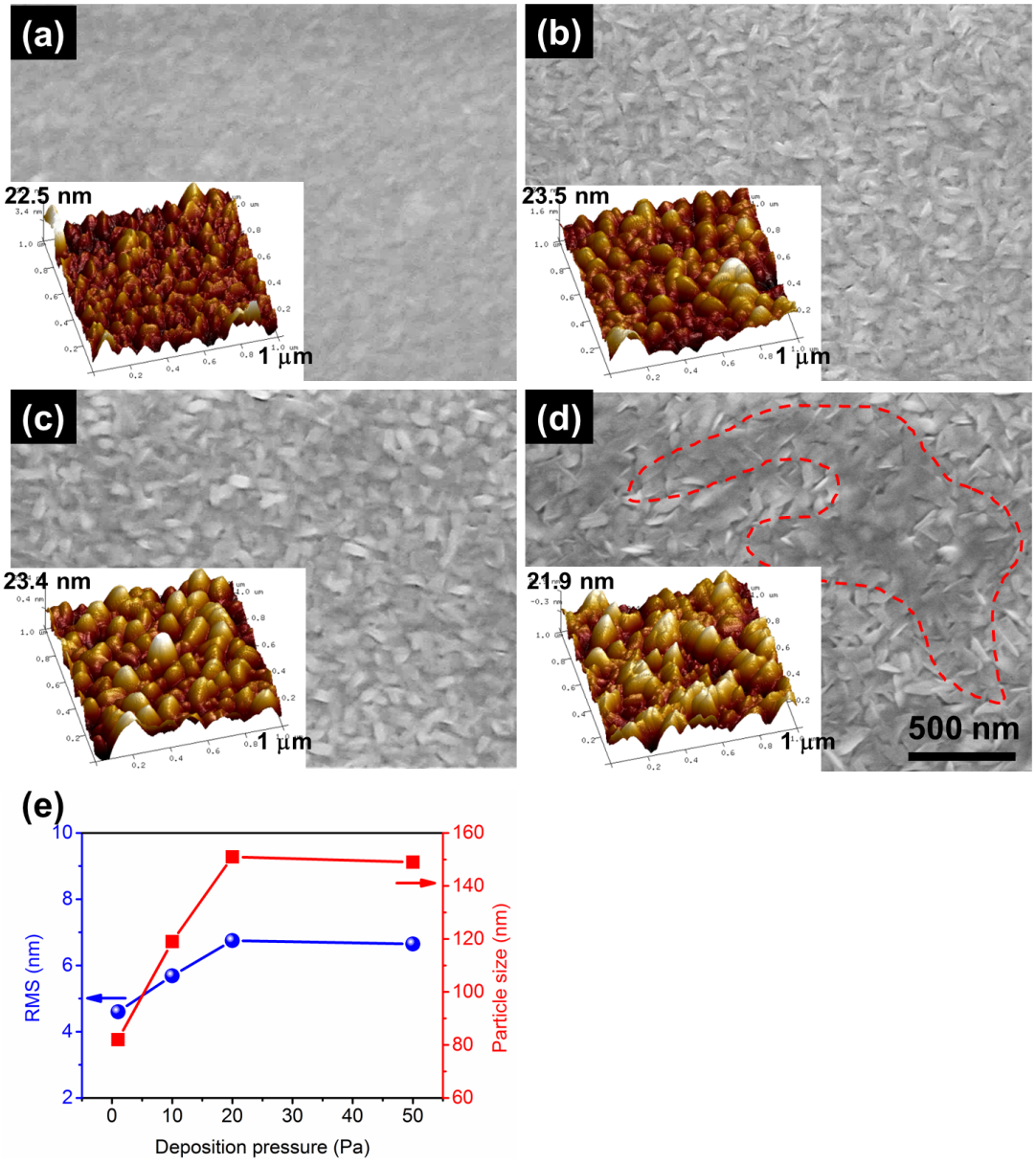

FIGURE 5.2: FESEM surface morphological characterizations of BSCF thin films deposited at oxygen partial pressure of (a) 1 Pa, (b) 10 Pa, (c) 20 Pa, and (d) 50 Pa. The insets are AFM images of each samples obtained at tapping mode. (e) The RMS roughness and average particle size calculated based on AFM images in (a)-(d).

structure with partially amorphous regions, which confirms our XRD observation and partially amorphous MIECs can likely give higher performance than Pt as a cathode for μ-SOFCs [112].

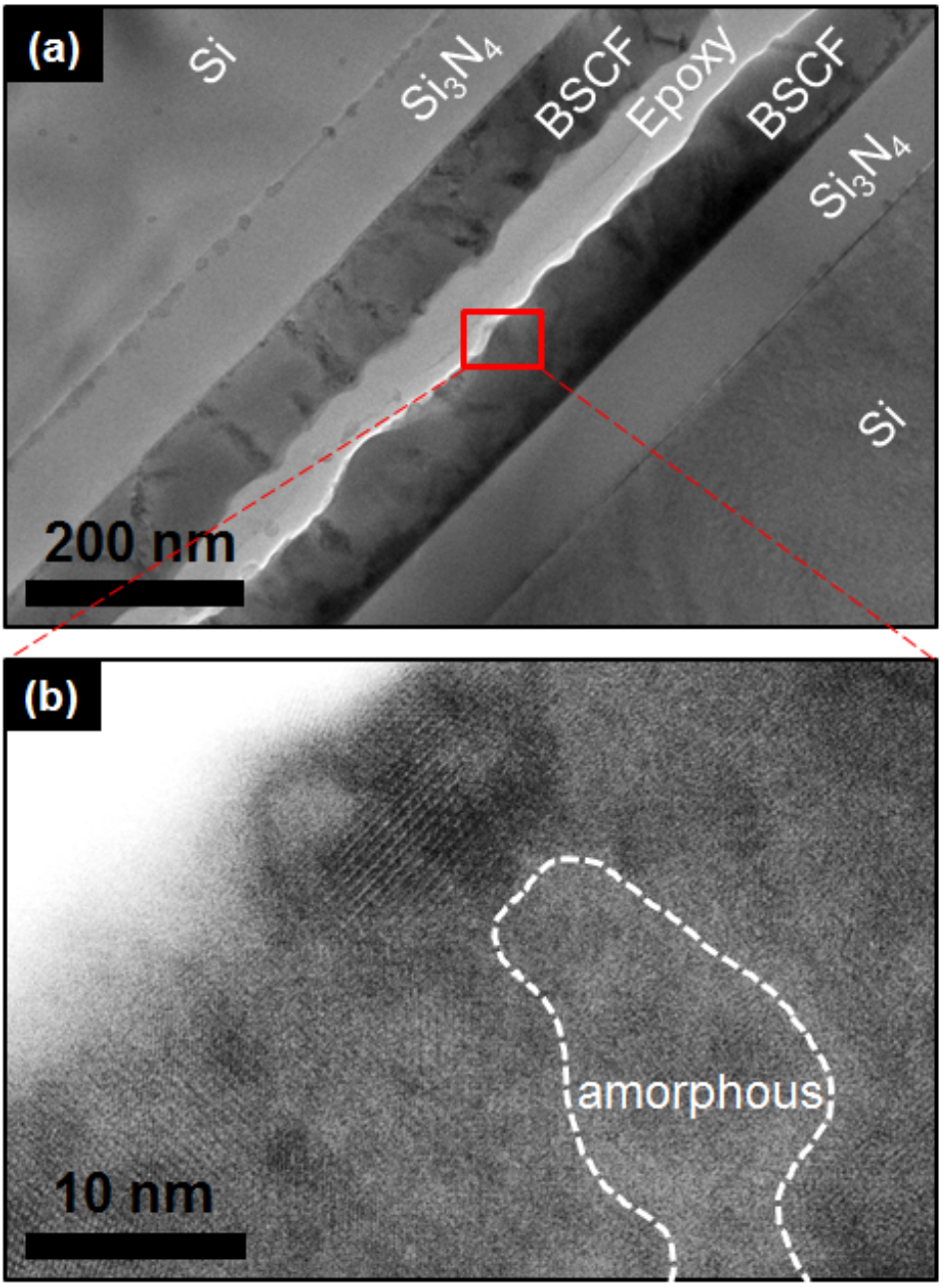

FIGURE 5.3: (a) TEM image of the cross-sectional view of BSCF thin film deposited at oxygen partial pressure of 20 Pa; (b) High-resolution TEM image of BSCF thin film.

5.3.2 Electrochemical Characterization of Dense and Nanostructured BSCF Cathodes

The performance of dense (1 Pa) and nanostructured BSCF (20 Pa) thin films were first characterized as cathodes for fuel cells using bulk YSZ as the electrolyte. The polarization curves of SOFCs using dense and nanostructured BSCF thin film cathode are shown in Figure 5.4a-b. A reference cell using typical sputtered porous Pt cathode was also characterized as shown in Figure 5.4c. The OCV values of both dense and nanostructured BSCF samples were around 0.9 V, which is lower than the theoretical value and cell with sputter Pt cathode, likely due to the not fully activated BSCF cathode after PLD deposition. For the cell using dense BSCF cathode, the maximum power densities were 0.48, 0.76, and 1.64 mW/cm^2 at 400, 450, 500 °C, respectively. For cells using nanostructured BSCF cathode, higher fuel cell performance were obtained with maximum power densities of 0.73, 1.29, and 2.11 mW/cm^2 at 400, 450, 500 °C, respectively. The performance of nanostructured BSCF is comparable with the Pt cathode cell, which shows a peak power density of 1.37 mW/cm^2 at 450 °C.

The typical Nyquist plots for cells with dense BSCF cathode and with nanostructured BSCF cathode tested at 500 °C are shown in Figure 5.4d. The large ohmic resistances of about 40 Ωcm^2 for both cells were mainly from the thick YSZ electrolyte (200 μm). The difference between the real-axis intercepts of the impedance plot represents the electrode polarization resistance (Rp) with two clear semicircles. The larger semi-circle in the frequency range around 1 Hz was deemed as

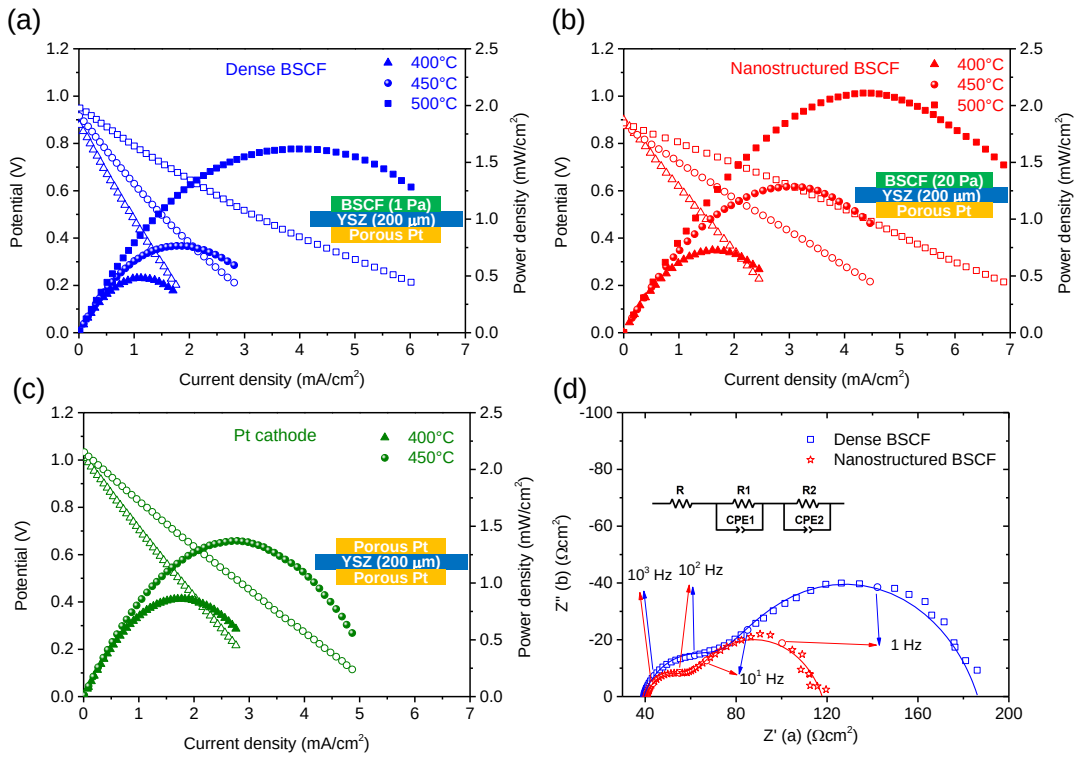

FIGURE 5.4: (a) Cell voltages and power densities as function of current density of YSZ electrolyte supported cells with (a) dense, (b) nanostructured BSCF thin film cathodes and (c). nanoporous Pt cathode; (d) typical Nyquist impedance curves for the dense BSCF and nanostructured BSCF cathodes tested at 500°C.

non-charge transport process including oxygen gas diffusion and surface absorption/dissociation processes [113], while for the smaller semi-circle at high frequency range of $>10^2$ Hz reflected the charge transfer process [114]. The Rp for dense BSCF was almost two times larger than nanostructured BSCF cathode. As these two cells differ only in cathode morphology, it is reasonable to infer the lower Rp was achieved by using the nanostructured BSCF cathode. From the EIS curves, we observed that both the charge transfer process and non-charge transfer processes were improved in nanostructured BSCF cathode over dense BSCF cathode. Yang et al. [115] reported that BSCF with higher surface area exhibited a mass-normalized oxygen evolution reaction (OER) activity which is 5.3 times greater

than that of a non-porous BSCF prepared by conventional synthesis methods. This means the catalytic activity of BSCF is highly dependent on the surface area, and the increased surface area from nanostructured BSCF can provide additional catalytically active sites. Similarly, for ORR in dense BSCF thin films, the majority of the reaction can only take place at the surface that is exposed to gaseous oxygen and therefore the density of effective reaction sites is low since only two-phase (gas/cathode) boundaries are available. On the other hand, nanostructured BSCF thin films allow better gas diffusion through the cathode and increase both the two-phase and three-phase (gas/cathode/electrolyte) regions.

5.3.3 Performance of μ-SOFCs using BSCF Cathodes

In order to test the functionality of BSCF thin film as cathode material for low temperature μ-SOFCs, BSCF thin films are deposited on BZY electrolyte at chamber pressure of 1 Pa and 20 Pa to achieve dense and porous structures. Figure 4 presents the FESEM characterization of the tested μ-SOFCs with columnar BZY electrolyte sandwiched between BSCF cathode and porous Pt anode. As shown in the cross-section image (Figure 5.5a and b), good adhesion between the electrolyte and cathodes are observed. The BSCF thin film deposited at 1 Pa shows conform dense structure while the thin film deposited at 20 Pa have porous structure. No obvious structural degradation of nanostructured BSCF cathode was observed as is typically seen for porous platinum electrodes [10, 41, 80].

Figure 5.6 shows the polarization curves of μ-SOFCs dense and nanostrucutred BSCF cathode thin films tested with dry H_2 fuel at temperature of 425 and 450 °C.

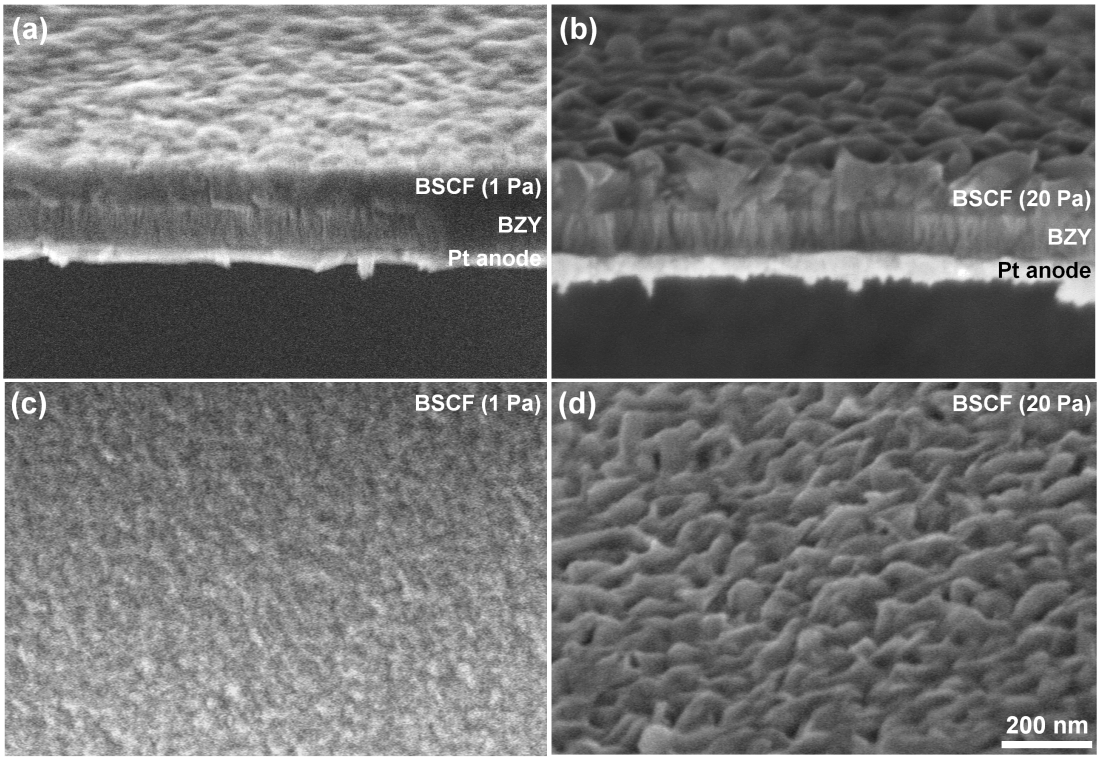

FIGURE 5.5: Cross-sectional FESEM characterizations of μ-SOFC with (a) dense BSCF thin film cathode deposited at 1 Pa and (b) nanostructured BSCF thin film cathode deposited at 20 Pa. (c) and (d) shows the corresponding surface morphologies of BSCF cathode films in (a) and (b) after fuel cell test.

The cell OCVs increased about 100 mV for both cells as the temperature increased from 425 °C to 450 °C, likely due to the BSCF cathode to be activated and reaching equilibrium with increasing temperature. For the dense BSCF cathode, the cell shows a maximum power density of 9.5 and 18.2 mW/cm^2 at 425 and 450 °C. The cell with nanostrucutred BSCF thin film gives maximum power densities of 27.3 and 55.1 mW/cm^2 at 425 and 450 °C, respectively, which is higher than the cell with dense BSCF film and previously sputtered dense films [63]. The enhance fuel cell performance is originated from the enhanced cathode reactions by making the BSCF porous; since the electrolyte and anode were identical in all the experiments. The MIEC cathode extends the active oxygen reduction site from the typical TPB to the entire exposed cathode surface, thus the surface to

volume ratio of the cathode is of great importance to the performance [109]. The increased surface area of nanostrucutred BSCF thin film produced by PLD at higher chamber pressure have increased the reaction sites, and hence improved the sluggish cathode kinetics at such low operating temperature.

5.3.4 Chemical Stability of BSCF Thin Film

The composition and chemical status of nanostructured BSCF thin film before and after fuel cell test were verified by XPS to see the chemical stability under operating conditions. Figure 5.7 shows the XPS spectra of Fe 2p, Sr 3d, Ba 4d, and Co 3p, respectively. Fe 2p spectra shows a broad and asymmetric peak, which consists of a mixture of valence states of Fe^{3+} and Fe^{4+}. Such mixed oxidation states could enhance the electrical conductivity of BSCF thin film through the creation of Fe^{3+}-O-Fe^{4+} bridges [116]. The intensity and position of the peaks in the spectra were nearly unchanged before and after fuel cell test, meaning the chemical status of these elements are stable. This justifies the good chemical stability of nanostrucutred BSCF thin film under the operating conditions of μ-SOFCs.

5.4 Chapter Summary

Nanostructured BSCF thin films were fabricated by controlling the deposition temperature and pressure of PLD. XRD and TEM characterization revealed that partially amorphous BSCF are formed. The structure of BSCF thin film changed

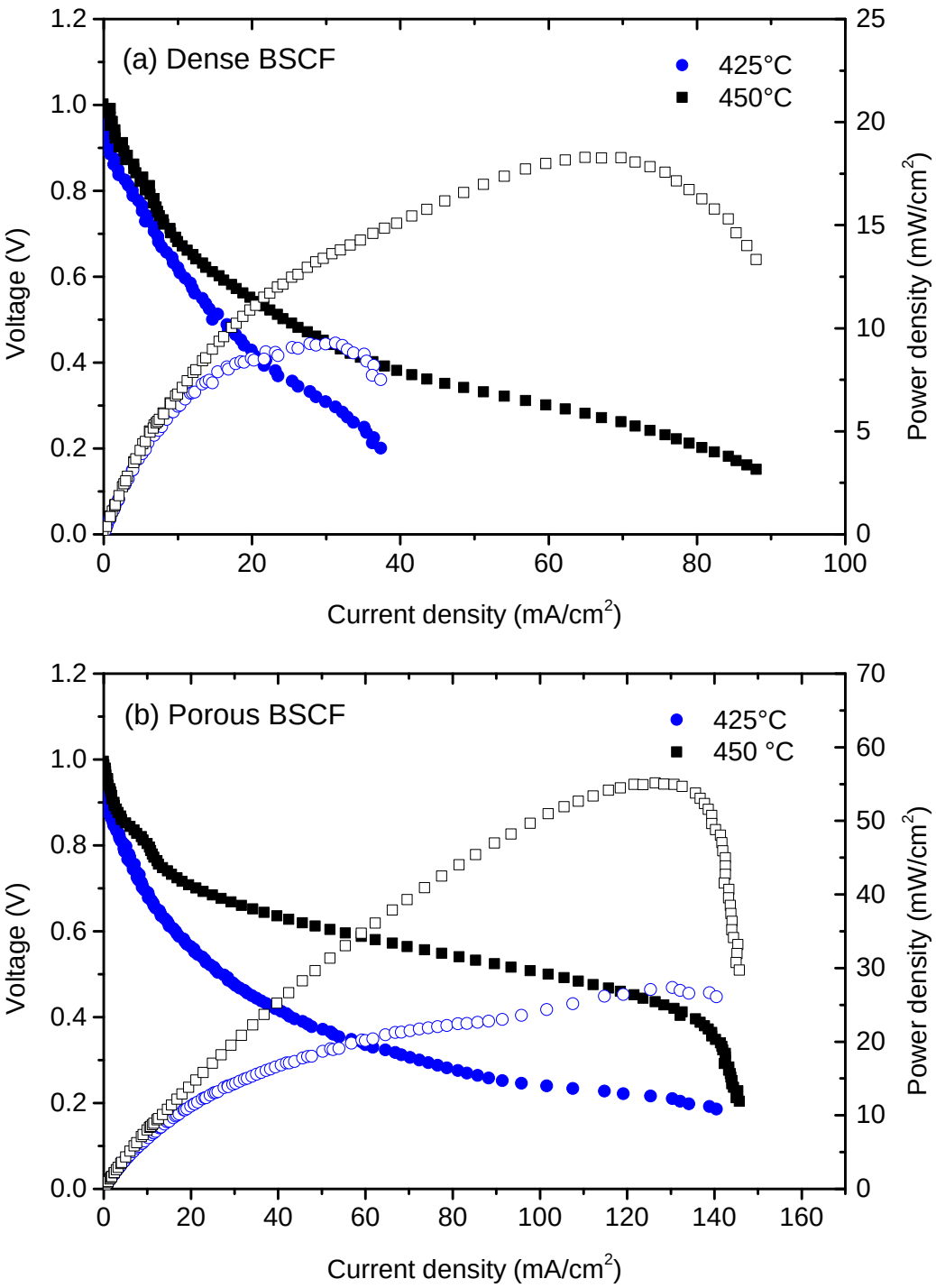

FIGURE 5.6: Cell voltages and power densities as function of current density of free-standing BZY electrolyte supported cells with (a) dense and (b) nanostrucutred BSCF thin film tested with H_2 fuel at temperatures of 425, and 450 °C.

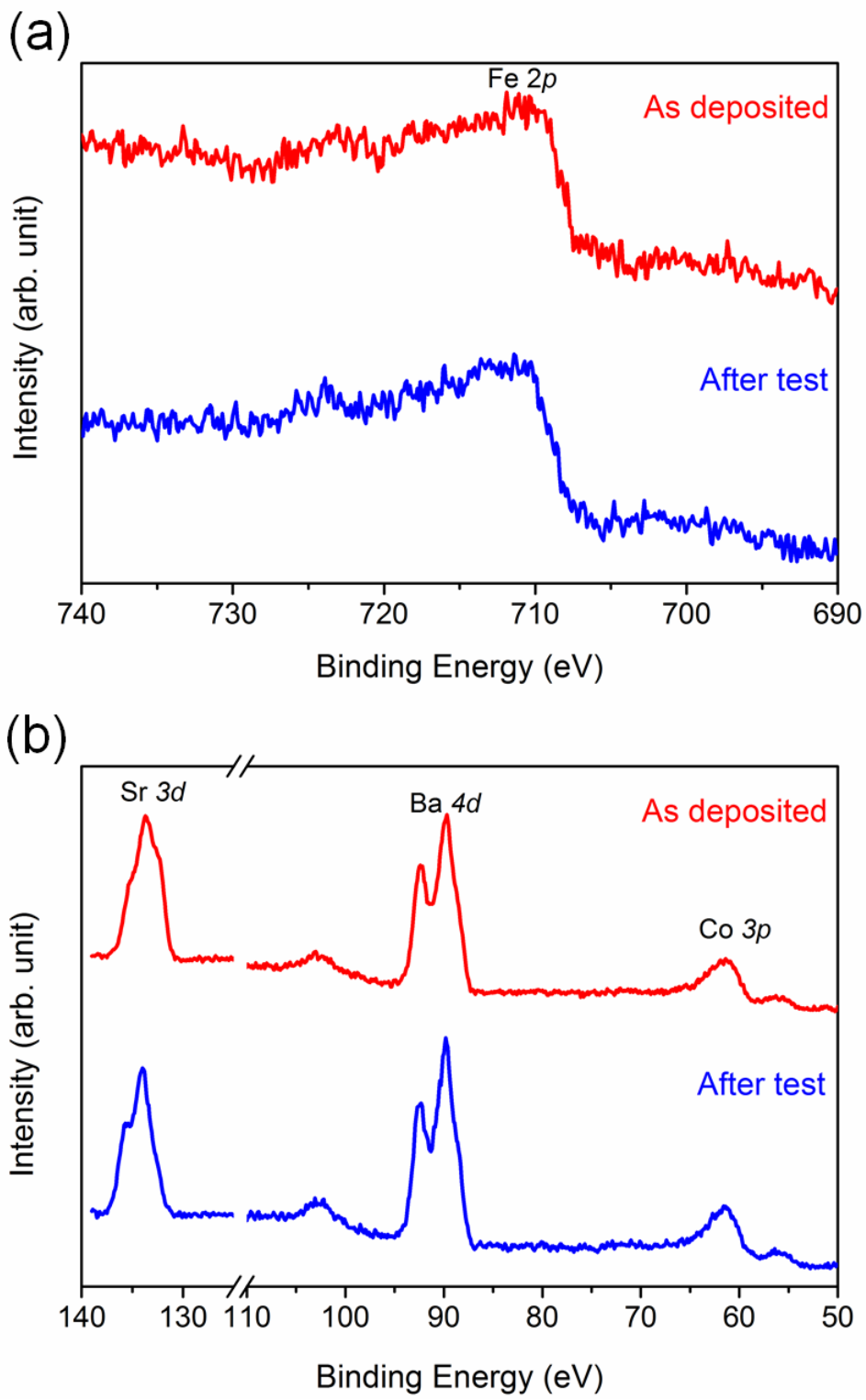

FIGURE 5.7: XPS spectra of (a) Fe 2p and (b) Sr 3d, Ba 4d and Co 3p for the nanostrucutred BSCF thin film cathode before and after fuel cell test.

from dense into nanoporous structure at higher chamber pressure. Both dense and nanostructured BSCF thin films were incorporated into bulk YSZ electrolytes and free-standing μ-SOFCs with proton-conducting BZY electrolytes to test the functionality of BSCF thin films as cathode for low temperature SOFCs. The porosity introduced within BSCF cathode extended the active oxygen/reduction sites, which leads to decreased cathode polarization resistance compared to dense BSCF cathode thin films. μ-SOFCs using nanostrucutred BSCF cathode deposited at 20 Pa achieved a maximum power density of 55 mW/cm^2 at 450 °C, which is the highest value obtained at such low temperature for ceramic cathode and higher than the performance of cells with dense BSCF cathode deposited at 1 Pa. The relative high performance, good thermal and chemical stability of nanostrucutred BSCF thin film indicate the promising prospect of ceramic MIEC cathode for low temperature μ-SOFCs.

Chapter 6

Conclusion

6.1 Summary and Contributions

This work is dedicated to investigate and fabricate high performance μ-SOFC with proton-conducting ceramic electrolyte at temperature lower than 500 °C. Several methods have been proposed to enhance the fuel cell performance.

First, cerium-based proton-conducting SOFCs are fabricated and characterized. BCY-based SOFC shows a maximum power density of 30 mW/cm^2 and an OCV of 0.59 V at 400 °C. The OCV decreases dramatically as testing temperature increases. The low OCV value and poor fuel cell performance were originated from the cracks formed during test. Poor chemical stability of BCY electrolyte was further demonstrated by SEM and XRD characterization. Zr-doped BCY electrolyte is employed to enhance the chemical stability and performance of cerium-based ceramic electrolytes. Both the OCV and fuel cell performance of BCZY-based

SOFC have great improvement compared with BCY-SOFC. The maximum power density has increased to 89 mW/cm^2 at 400 °C, which is nearly 3 times that of BCY-based SOFC. The OCV was maintained at around 1.0 V, showing that BCZY is promising electrolyte candidate with essential ionic conductivity and chemical stability for low temperature SOFC application.

Second, high performance μ-H-SOFC using BZY as electrolyte was obtained by utilizing an 8 nm thin film GDC cathode interlayer. The cathodic polarization resistance was effectively reduced by the additional GDC interlayer between the Pt cathode and BZY electrolyte. A high peak power density of 445 mW/cm^2 was obtained at 425 °C from the μ-H-SOFC with GDC/BZY bi-layer electrolyte. The EIS analysis of cathodic impedance of the fuel cells showed the enhanced cathodic charge transfer process across the cathode/electrolyte interface with the help of GDC interlayer, suggesting the effective promotion of proton and oxygen ion charge transfer as well as ORR and water evolution reaction between Pt cathode and BZY electrolyte through the GDC interlayer. The mixed oxygen and proton conduction in the GDC interlayer has expanded the ORR sites from a 2-dimentional planar interface between Pt and BZY to the entire GDC interlayer.

Third, nanostructured BSCF thin films were fabricated by optimizing PLD deposition parameters. The porosity introduced within BSCF cathode extended the active oxygen/reduction sites, which leads to decreased cathode polarization resistance compared to dense BSCF cathode thin films. μ-SOFC incorporating nanostructured BSCF cathode achieved a maximum power density of 55.1 mW/cm^2 with

OCV of 0.99V at 450 °C. In terms of structural stability, the proposed nanostructured BSCF cathode film can sustain its porosity after fuel cell test, which is superior to nanostructured Pt cathode fabricated by sputtering. The nanostructured BSCF thin film is also chemically stable after fuel cell test as evidenced by XPS result. Therefore, PLD deposited nanostructured BSCF thin film can be a potential choice of cathode for integration in low temperature SOFCs.

6.2 Suggested Future Work

This work has demonstrated several methods to enhance the performance of μ-H-SOFCs at low operating temperature, including fabricating high ionic conducting electrolyte, reducing the thickness of electrolyte, enhancing the cathodic reaction at the electrolyte/cathode interface, and fabricating nanostructured ceramic cathode with high porosity. However, the fuel cell performance of proton-conducting SOFC is still lower than conventional oxygen-ion based SOFC. In order to improve the fuel cell performance of proton-conducting SOFC, the following future works are proposed.

- **Fabricate epitaxial-BZY μ-SOFC**

Epitaxial BZY thin film shows the highest proton conductivity due to the absence of grain boundary resistance. In this work, all the fuel cells were fabricated on Si_3N_4 supporting layer, showing a polycrystalline structure. The high conductivity of BZY electrolyte is still not fully utilized. Thus an epitaxial-BZY μ-SOFC structure is proposed in Figure 6.1. The Si_3N_4 supporting layer will be replaced

by an epitaxial MgO layer, then an epitaxial BZY electrolyte is expected to be grown.

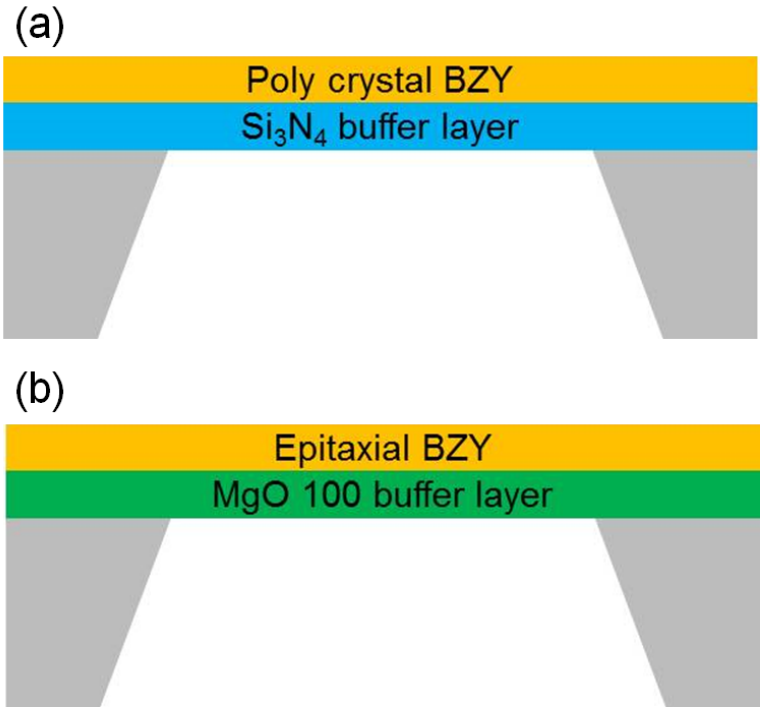

FIGURE 6.1: (a) Current Si_3N_4 supported μ-SOFC structure and (b) proposed epitaxial BZY μ-SOFC.

The first attempt will be focus on the fabrication of epitaxial MgO (100) buffer layer on Si wafer or Si_3N_4 layer. Previous researchers demonstrated that the preferred MgO phase is related to the deposition temperature [117]. By varying the deposition conditions, epitaxial MgO thin film buffer layer can be obtained. Thus, epitaxial BZY thin film may be achieved on these buffered MgO layers.

• Develop compatible electrode materials for proton-conducting SOFCs

It is found that cathode ORR is the most sluggish process for the SOFC, especially at low operating temperature. In this work, we have successfully enhanced the fuel cell performance by incorporating a thin dope-ceria layer to reduce the cathodic resistance. However, the thickness effect of this layer is still unknown. Possible

tripe conducting materials, which possess $O^{2-}/H^{+}/e^{-}$ conduction would be better candidate for this purpose. Thus exploring possible tripe conducting materials as the cathode or cathodic interlayer would be promising.

- **Explore suitable anode catalyst for better alcohol oxidation reaction**

The performance of direct ethanol μ-SOFCs is not high enough as expected. A suitable catalyst anode material should be explored to enhance the ethanol oxidation reaction. Possible candidate materials are alloys of Pt, Ru, Sn, etc. [118]. In the future, co-sputter technique or ALD can be employed to fabricate these novel hydrocarbon oxidation catalysts for low temperature SOFC.

- **Design and fabrication large scale MEMS-based SOFC system**

This work mainly focuses on the material study and single chip test, which is still at the conceptual stage. Future work could focus on the fabrication of the entire μ-SOFC system by integrating the fuel supply, fuel reforming units, and device sealing and packaging into micromaching fabrication process.

Appendix A

μ-SOFC Fabrication and Characterization

A.1 Fuel Cell Fabrication

The fabrication process of free-standing μ-SOFC is illustrated in Figure A.1. The main scheme of μ-SOFC structure is to utilize a free-standing thin film to support the electrolyte layer, as described in previous works [10]. Detailed fabrication sequence is listed below.

(a) Wafer preparation: 4-inch <100> silicon wafer (Bonda Technology, 375 ± 25 μm) was ultrasonic cleaned in acetone, isopropyl alcohol (IPA), deionized water (DI water) sequentially for at least 10 minutes, then dried under blowing N_2 flow.

(b) Si_3N_4 layer deposition: 200 nm thick of low-stress silicon nitride as a blocking layer for silicon etching and supporting layer for electrolyte deposition was

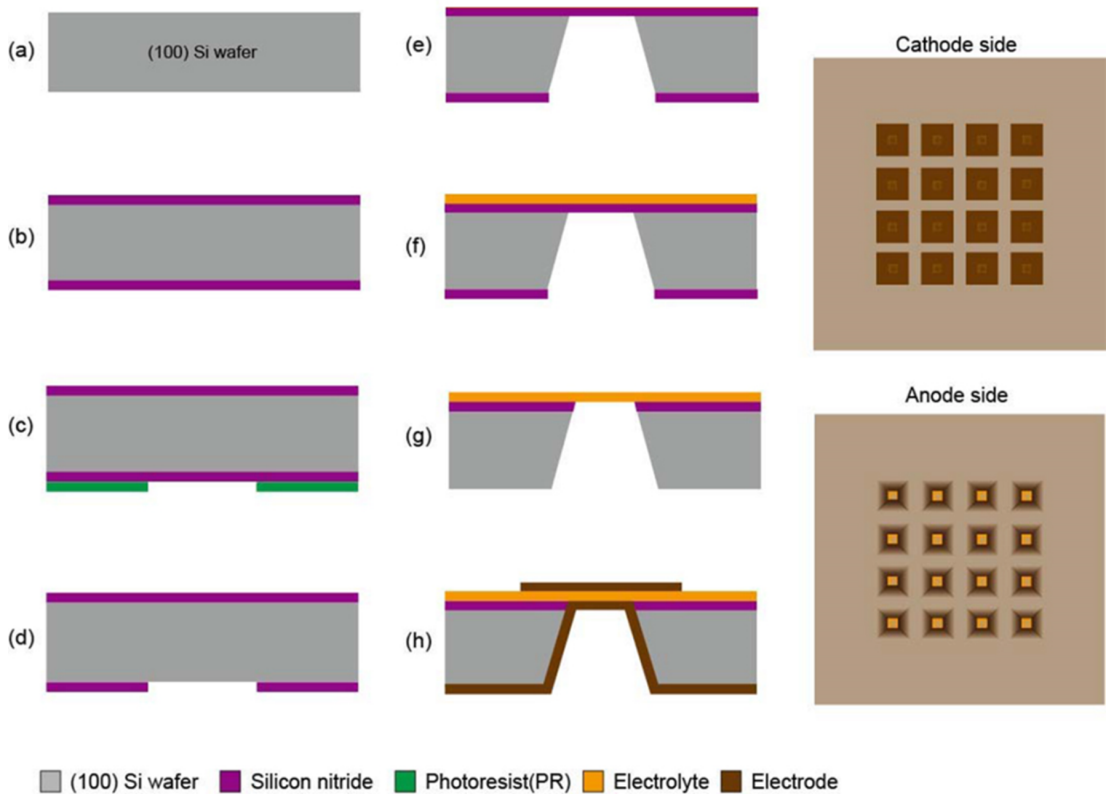

FIGURE A.1: Fabrication flow of thin film free-standing square electrolyte μ-SOFC.

fabricated on both sides of the silicon wafer. The Si_3N_4 layers are fabricated by low pressure chemical vapor deposition (LPCVD) to reduces the difference in the thermal expansion between different components.

(c) Lithography: 6 μm AZ9260 photoresist was spin coated on one side of the wafer. The wafer was exposured under a designed shadow mask to transfer the square pattern and then developed.

(d) Dry etching: the patterned photoresist on the bottom side is utilized as an etching mask for reactive ion etching (RIE) for removal of exposed silicon nitride. After RIE, the remaining photoresist was removed by acetone or piranha etching.

(e) KOH etching: anisotropic Si wafer etching was performed in 30wt% KOH solution at 85 °C for about 5 hours, remaining a square free-standing Si_3N_4 supporting layer.

(f) Electrolyte deposition: BZY thin film electrolyte layer was deposition on top of the free-standing Si_3N_4 layer by PLD technique described before.

(g) RIE etching: the Si_3N_4 underneath the electrolyte layer was removed by RIE to release the free-standing BZY electrolyte.

(h) Electrode deposition: porous Pt electrodes were sputtered on both side as the anode and cathode. The cathode was deposited under a shadow mask to separate each single fuel cell.

The fabricated structure was diced into 1×1 cm^2 and subject to fuel cell performance testing.

A.2 μ-SOFC Characterization

The fuel cell performance was tested with a customized μ-SOFC test station (see Figure A.2). μ-SOFC chip was sealed on a stainless steel custom-designed fuel cell test chamber, which was fixed in a heating controlled furnace. This tube furnace can ensure a uniform temperature distribution for both anode and cathode side. Fuels such are hydrogen and ethanol are supplied to the anode side, and the cathode side is exposed to the ambient. The performance of μ-SOFC is measured by obtaining the current-voltage (I-V) relation at temperatures from 300 °C to 500

°C. For the I-V and impedance data collection, a Solartron 1470E potentiostats system and 1255B Frequency Response Analyzer (FRA) were used. The temperature then evaluated to the desired testing temperature with a heating rate of 10 °C/min. An Au coated tungsten probe, which was placed in a micro-positioner, was contact to the cathode film as a current collector. The substrate and tungsten were connected to the potentiostat and frequency analyzer.

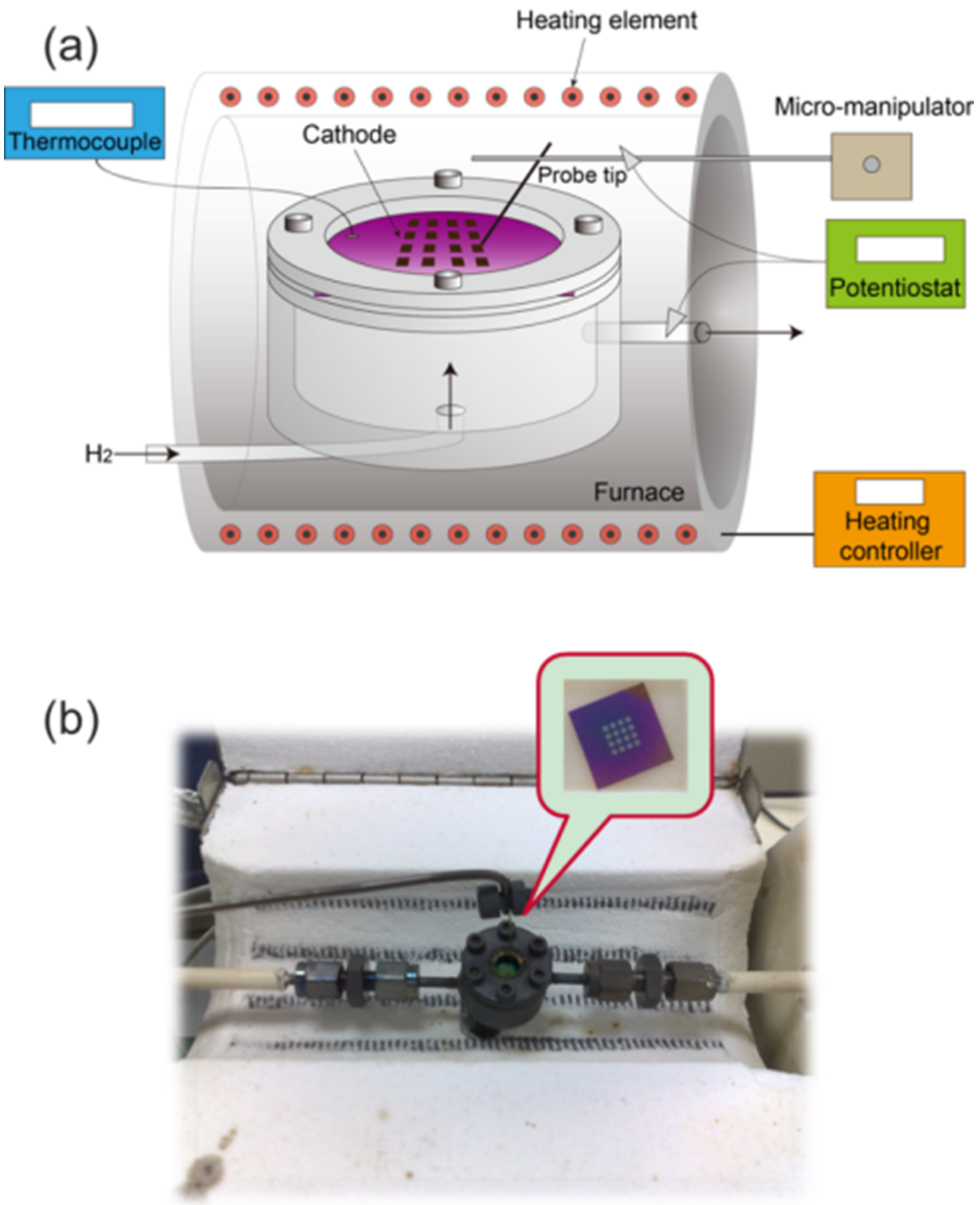

FIGURE A.2: μ-SOFC test station: (a) schematic picture; (b) optical image of customized test setup.

Appendix B

Nanoporous Palladium Anode for Direct Ethanol SOFCs with Nanoscale Proton-conducting Ceramic Electrolyte

B.1 Introduction

Direct ethanol fuel cell (DEFC) is a type of fuel cell which can convert the energy through electrooxidation of ethanol, into electrical energy. DEFCs allow easy handling and storage of high energy density liquid ethanol; therefore provide a promising alternative to hydrogen fuel cells in portable applications [119, 120]. Currently, most DEFCs are demonstrated with polymer-based electrolyte membranes with

cell operating temperatures limited below 150 °C. Increasing the operating temperature of DEFC is advantageous, not only to fully oxidize the ethanol fuel on anode, but also to enhance the oxygen reduction kinetics on cathode [121, 122]. However, the conductivity of polymer electrolyte membranes decreases drastically with further increased temperature due to the loss of water content in the electrolyte that is strongly associated with effective ion conduction. Another common inconvenience of polymer electrolyte is the fuel crossover from anode to cathode that promotes the adsorption of the fuel and its intermediates onto the cathode surface, which blocks the oxygen reduction reaction (ORR) at cathode side [123, 124].

On the other hand, a proton-conducting ceramic electrolyte can be an alternative for polymer electrolyte operating at temperature above 150 °C. Ceramic electrolyte has no fuel crossover due to a dense structure and doesn't need water management for proton-conduction. Furthermore, fuel cell based ceramic electrolyte is normally ran higher temperatures than current high temperature polymer electrolyte DEFC, which helps to accelerate the electrode reactions kinetics, enhance anode CO tolerance, and avoid to use extremely expensive noble electrode materials. Besides, proton-conducting ceramic electrolyte has smaller activation energy for ionic transportation, allowing fuel cell based on proton-conducting ceramic electrolyte lower operating temperature than the conventional oxygen ionic conducting ceramic electrolyte (600-1000 °C), which means higher voltage efficiency and theoretical energy efficiency [6, 85], and wider cell component, balance of plant

choice, as well as material and system stability. Among all proton conducting electrolytes, BZY is the most chemical stable proton conductor, which has also high proton conductivity over other conventional oxide ion conductors [6, 125]. With thickness in the range of 750 nm to 20 μm, the electrolyte ASR can reach target value of 0.15 Ωcm^2 for high performance operating at the operating temperature range of 200 °C and 450 °C [4]. Therefore, SOFC with nanoscale thin film proton conducting electrolytes with suitable electrode materials would be a potential candidate for the direct ethanol application.

The need for highly active catalysts for the ethanol oxidation reaction (EOR) that takes place at anode at the temperature range of 200-400 °C is the main challenge in the development of DEFCs. Pt-based catalysts are commonly used in low temperature polymer electrolyte DEFCs due to its high catalytic activity towards ethanol. However, the CO poisoning of Pt catalysts arouses performance degradation, leading to lower fuel utilization and cell performance, also it requires for excess of Pt loading for efficient fuel oxidation [126]. Recently, catalysts based on Pd have been explored as alternate anodes because Pd shows excellent catalytic activity towards hydrocarbon fuel oxidation at low temperature [127–130] and Pd is more abundant in nature and less expensive than platinum [131]. However, most the above fuel cell studies are focus on either polymer electrolyte, or ceramic oxide electrolyte at high temperature (>600 °C) while the research on the temperature of 200-500 °C are rare. The only application of Pd thin film anode for μ-SOFC with YSZ was demonstrated by Lai et al. [130] and peak power densities of 75-385 mW/cm^2 at 440-550 °C were achieved with methane fuel.

Actually, Pd would be more suitable for proton-conducting SOFC application due to its high proton diffusivity and electronic conductivity [132]. Thus, the purpose of this study is to demonstrate the direct utilization of ethanol fuel for μ-SOFC with proton-conducting ceramic electrolyte and Pd anode at the temperature range of 300-400 °C. The morphological evolution of Pd anode films under hydrogen and ethanol fuel operation are compared and discussed.

B.2 Experimental Methods

B.2.1 Thin Film Deposition

BZY thin films were fabricated by utilizing PLD technique. A 248 nm KrF excimer laser (Lambda Physik) with laser fluence of 3.0 J/cm^2 per pulse was used to ablate a sintered $BaZr_{0.8}Y_{0.2}O_{3-\delta}$ pellet target (Praxair Inc.). Before the deposition, the main chamber was evacuated to a base pressure of 1.0×10^{-7} Torr. After heating up the substrate to desired temperature of 400-800 °C with a heating rate of 25 °C/min, the vacuum system was maintained at oxygen partial pressure of 1.0 mTorr. Both substrate and target were kept rotating to ensure a uniform film deposition. The distance between the target and the substrate was kept at 80 mm. The repetition rate was 10 Hz and deposition duration was 30 minutes. After deposition, the samples were cooled down to room temperature with a cooling rate of 10 °C/min in the same oxygen environment to avoid crack formation during the severe temperature change of the free-standing membrane.

B.2.2 Fuel Cell Fabrication and Test

A nanoscale thin film micro fuel cell was fabricated on micromachined Si substrate with the help of lithography and etching techniques, as reported before [10, 47]. A patterned 10×10×0.4 mm^3 Si_3N_4 coated Si chip has an array of free-standing Si_3N_4 membranes, which were used as the substrate for PLD deposition of BZY. After the deposition of BZY electrolyte, the Si_3N_4 supporting layer was removed by relative ion etching (RIE) with CF_4 gas, resulting in a free-standing BZY electrolyte. For catalysis and current collection, porous Pt layer was deposited on the cathode side by using radio frequency (RF) sputtering technique with power of 100 W and Ar pressure of 30 mTorr at room temperature. Pd anode thin films were deposited by direct-current (DC) sputtering in Ar pressure of 3 and 80 mTorr for comparison.

After fabrication, fuel cell performance measurements of BZY μ-SOFC were conducted on a custom-designed micro fuel cell test station (Figure B.1). The switchable fuel feeding setup (Figure B.1a) ensures an intermittent fuel feeding of H_2 and ethanol. Ethanol solution droplets were instantly vaporized when dropped into the reaction bulb, which was heated up to 150 °C. Then the vaporized ethanol fuel and water were supplied to the anode side driving by N_2 purge gas with a flow rate of 20 sccm. μ-SOFC chip was sealed on a stainless steel chamber, which was placed in a heating controlled furnace (Figure B.1b). This heating furnace can ensure a uniform temperature distribution for both anode and cathode side. The electrochemical performance of the cells was measured with a multichannel potentiostat (Solarton 1470E) and frequency response analyzer (Solartron FRA 1255B)

in the temperature range of 300-400 °C.

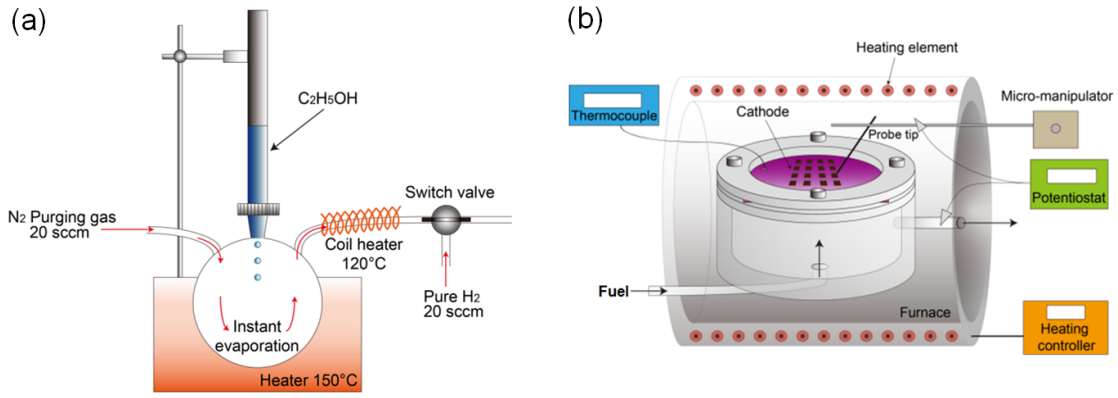

FIGURE B.1: Schematic of (a) switchable ethanol fuel feeding system and (b) custom-designed μ-SOFC test station.

B.2.3 Material Characterization

The crystallinity and structural phase of the deposited films were characterized by GIXRD system equipped with a CuKα X-ray source (PANalytical Empyrean XRD, Netherlands) and operated at a voltage and current of 40 kV and 40 mA with small incident angles of 0.5°. The cross-sectional structures of BZY μ-SOFCs were obtained by field-emission scanning electron microscopy (FESEM, JSM-7600F, JEOL, Ltd., Japan). The composition and chemical states of deposited films before and after fuel cell test were determined using X-ray photoelectron spectroscopy (XPS, Kratos AXIS Ultra) with a monochromatic AlKα (1486.71 eV) X-ray radiation (15 kV / 10 mA).

B.3 Results and Discussion

B.3.1 Thin Film Characterization

The crystallinity of BZY thin films deposited on Si_3N_4 substrates with different deposition temperatures are analyzed by XRD, as shown in Figure B.2. The BZY thin films deposited at temperatures lower than 500 °C show large bump distributed in a wide range with no discernible peaks, which indicates that these films are amorphous without ordered crystal structures. As the deposition temperature increase to 600 °C, the XRD pattern shows gradually increased crystallization and a polycrystalline film is formed. As expected, films show higher crystallized patterns at higher deposition temperature of 800 °C. A strong (110) reflection peak appears to be predominant for the film with a full width at half maximum (FWHM) of 0.43°. High temperature favors crystal growth of BZY thin film on Si_3N_4, while low temperature results in amorphous structures. Thus, substrate temperature is a critical parameter to the crystallinity of BZY thin film deposited by PLD. A higher deposition temperature can ensure better polycrystalline BZY thin film. Previous research has found BZY thin film grown above 400 °C was too fragile to be utilized as the electrolyte for free-standing μ-SOFC due to the crystallization process [41]. However, here we have demonstrated that the film can be survived after deposition at high temperature of 800 °C with controllable cooling process. Thus we chose 800 °C as the electrolyte deposition temperature for the fuel cell fabrication, as highly crystallized BZY thin film possess higher proton conductivity [35].

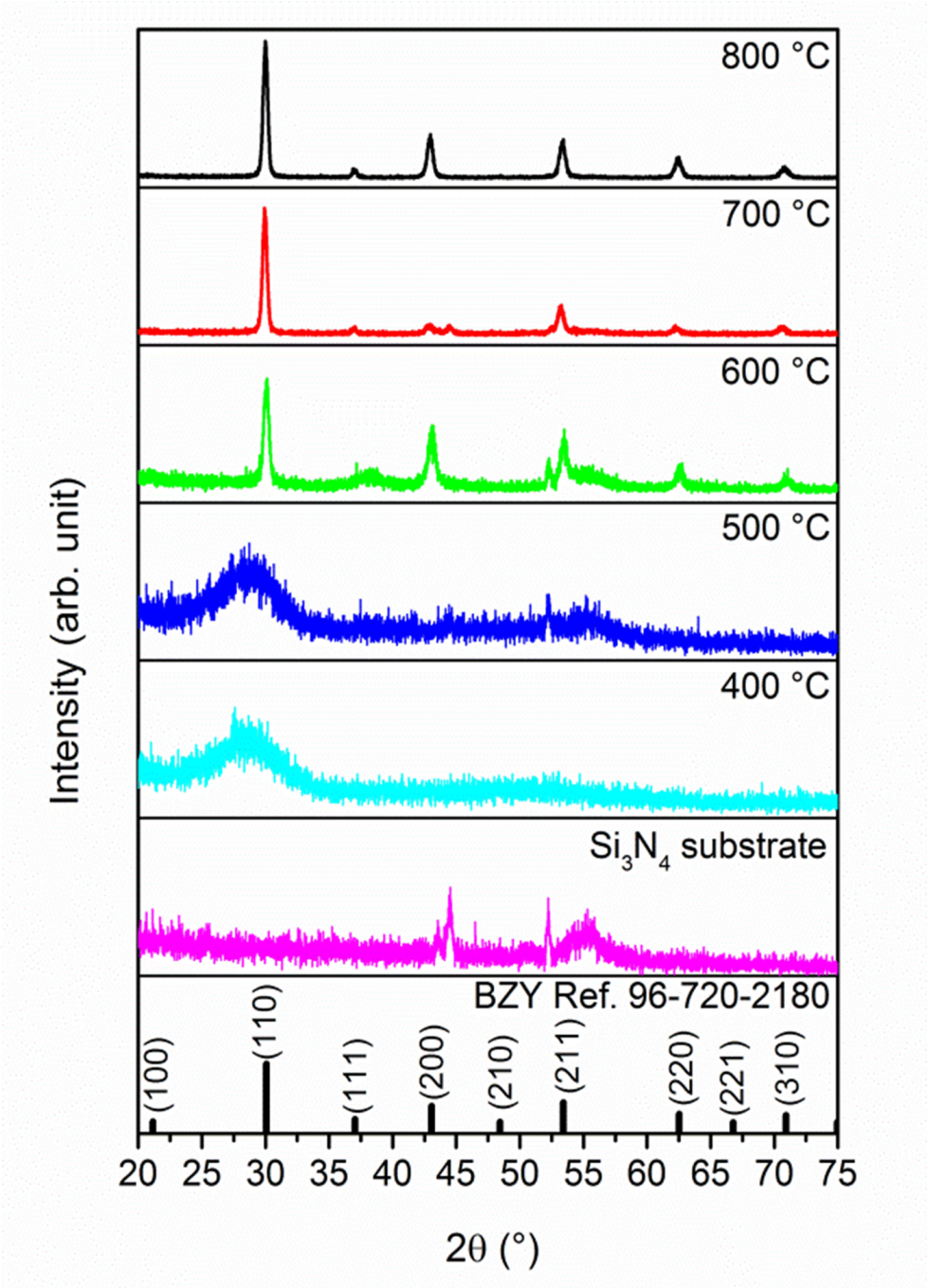

FIGURE B.2: XRD patterns of PLD films deposited at various substrate temperatures. Bare Si_3N_4 substrate together with reference peaks for BZY (PDF No. 96-720-2180) are included for comparison.

The porosity of Pd anode is critical to the anode performance towards ethanol oxidation as porous electrode has better gas diffusion and enhances TPB for the reaction than dense electrode. In order to achieve a porous thin film, the effect of Ar pressure for DC sputtering is compared. Figure B.3 shows Pd thin film deposited at 3 mTorr and 80 mTorr, respectively. The film deposited at lower pressure of 3 mTorr shows uniform and smooth surface. The individual grain with grain size around 20 nm is clearly observed. Nanoporous Pd film is achieved at higher deposition pressure of 80 mTorr. The film shows highly granular clusters and the dimension of each cluster is in the range of 60-150 nm with a pore gap around 8 nm, which is similar to the optimized Pt nanoporous films [110]. The XRD patterns of both dense and porous film shown in Figure B.4 are well indexed to reference Pd diffraction pattern (PDF No. 00-046-1043), indicating well-crystallized films are fabricated at room temperature by sputtering.

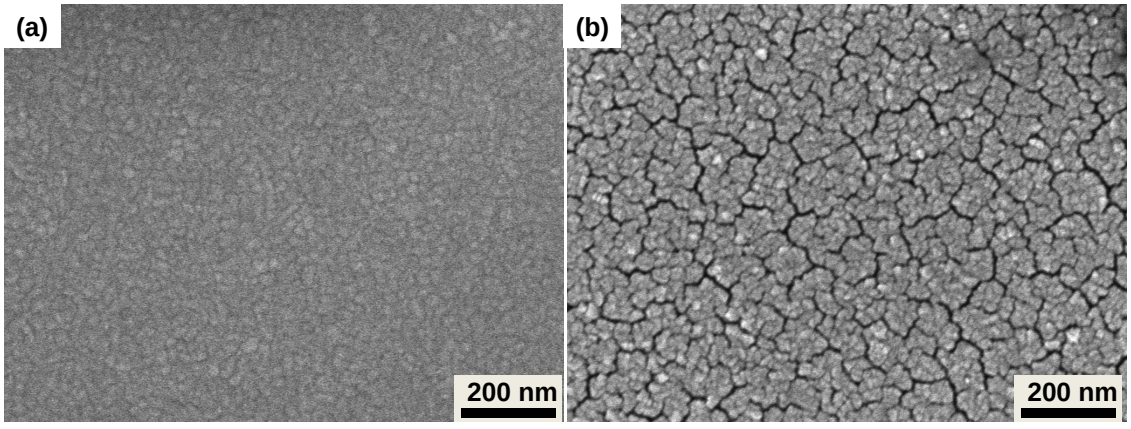

FIGURE B.3: FESEM surface characterization of Pd thin film sputtered at Ar pressure of (a) 3 and (b) 80 mTorr.

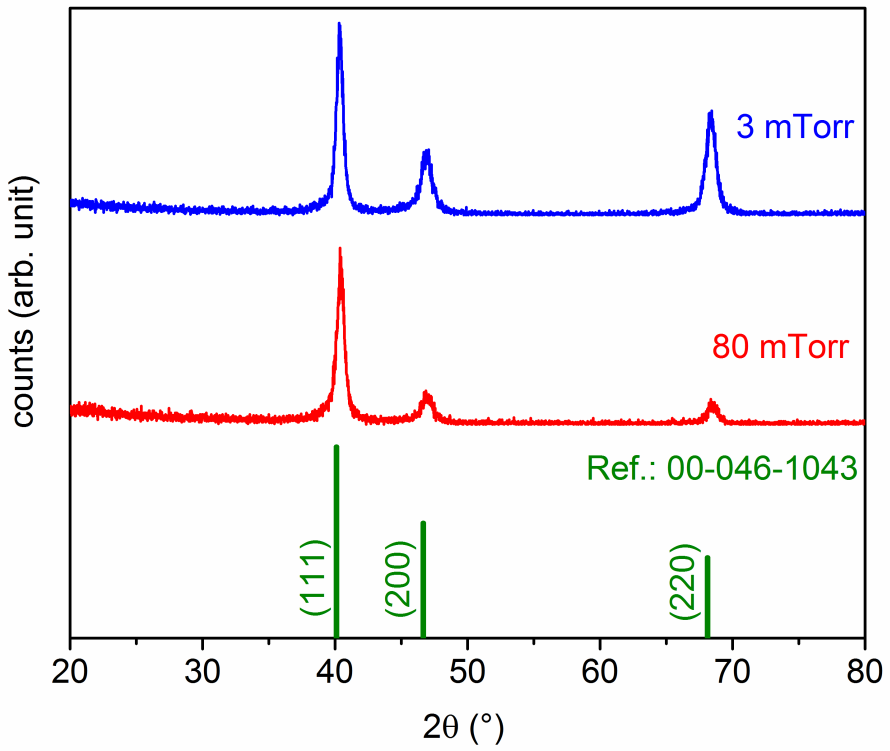

FIGURE B.4: XRD patterns with reference peaks for fcc-Pd (PDF No. 00-046-1043) of Pd thin film deposited at Ar pressure of 3 and 80 mTorr.

B.3.2 Electrochemical Characterization of μ-SOFC with Pd anode

Figure B.5 shows the I-V polarization and power density curves of the proton-conducting μ-SOFC tested with H_2 and ethanol fuels at 350 and 400 °C. By feeding with hydrogen fuel, the fuel cell gained peak power densities of 26.7 and 72.4 mW/cm^2 at 350 and 400 °C, respectively. As expected, the peak power densities have been reduced to 9.8 and 15.3 mW/cm^2 at 350 and 400 °C when fuel supply switched to ethanol fuel (Figure B.5b). The performance drop is originated from the reduced catalytic activity towards ethanol oxidation compared to hydrogen oxidation evolution, as the required energy for bond cleavage of ethanol is higher

than hydrogen fuel. Figure B.5c shows the OCV evolution of BZY SOFC fueled with hydrogen and ethanol fuel during fuel cell test. At 350 °C the OCV for H_2 fuel is steadily maintained around 1V, while for ethanol operation, the OCV fluctuated around 0.75 V, which is relative low compared with H_2. An interesting OCV rise has been observed as the testing temperature increases. The OCV value for ethanol was gradually increased to 0.83 V at 400 °C, which is an acceptable value for ethanol fuel cell at this temperature range. The fluctuation of measured OCV is possible due to the unstable evaporation of liquid ethanol and possible changes of local anodic composition generated by catalytic decomposition of the fuel [133]. The incensement of OCV at evaluated temperature is attributed to the equilibrium electrode kinetics during fuel cell operation. The as-deposited Pd has porous structure, which can ensure gas diffusion while possess degraded electrical conductivity. However, as the increase of testing temperature and duration, there was gradual formation of in-plane current collection paths within the porous electrodes during the temperature ramp as observed in previous work [62]. Thus the OCV value would increase due to better electrical connecting inside the porous electrodes. Another reason ascribed to the incensement is the gradual activation of Pd catalyst toward ethanol oxidation.

The cross-sectional view of Pt/BZY/Pd heterostructure after fuel cell test is shown in Figure B.6a. The 3-layered structure is about 260 nm thick and shows good adhesion between electrolyte and electrodes without detachment or cracks. The columnar-like BZY electrolyte is dense and gas tight, with a thickness of about 130 nm. The microstructure evolutions of porous Pd anode under operation of

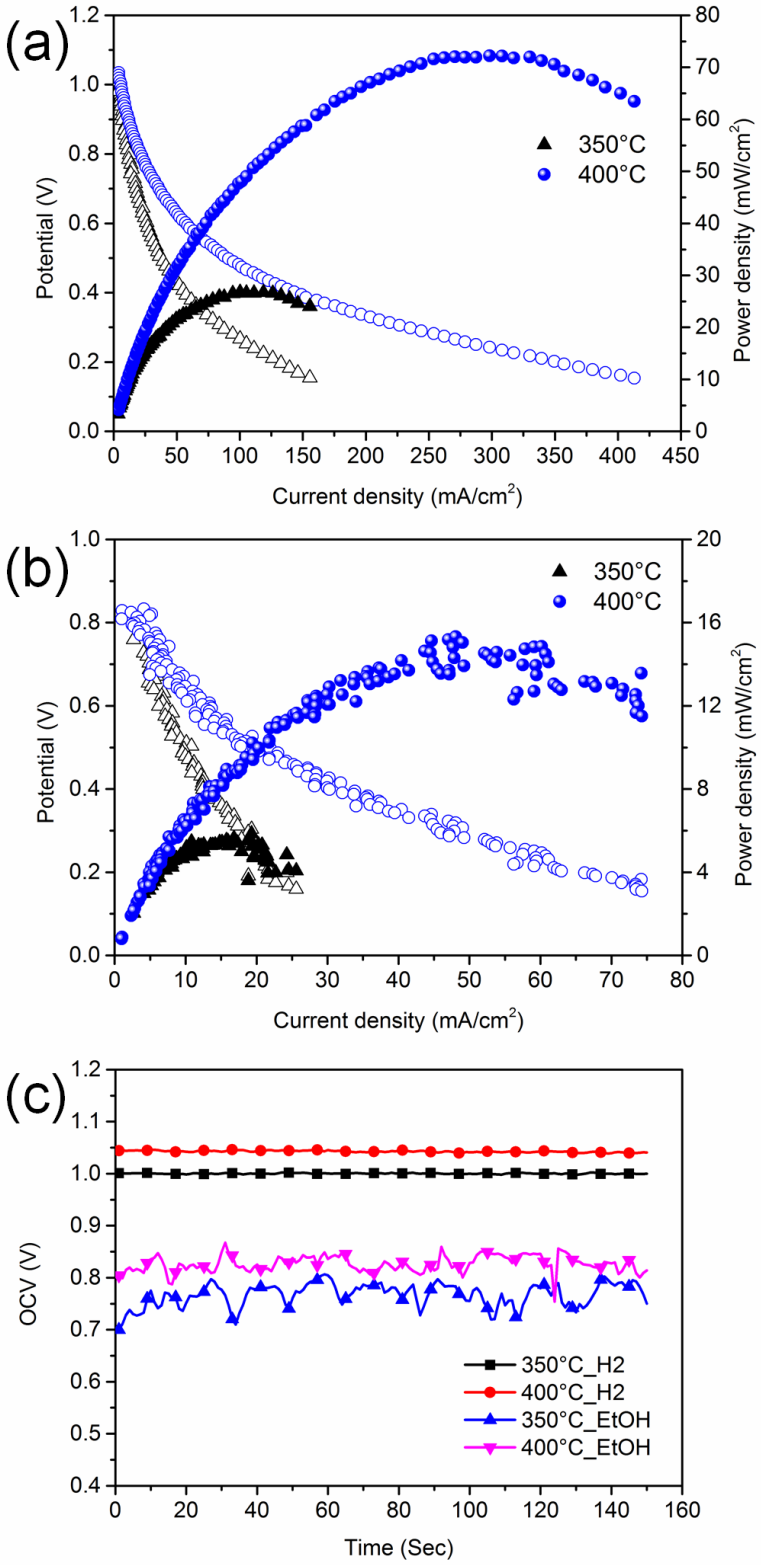

FIGURE B.5: I-V-P performances of μ-SOFC consisting of Pd anode test with (a) dry hydrogen fuel and (b) ethanol fuel at 350 and 400 °C; (c) OCV evolution for dry hydrogen and ethanol fuel testing after temperature stabilization at temperature of 350 and 400 °C;.

hydrogen and ethanol fuel are investigated and shown in Figure B.6b-d. For the anode only operated with hydrogen fuel, the porous Pd cluster emerged together to form large clusters due to the thermal annealing and hydrogen reduction reaction during operation, which is similar to porous Pt film deposited and tested under similar conditions [10]. The cluster size has increased to several hundred nanometers in dimension and the pore gas increased to 20-40 nm, which are often attributed to the Ostwarld ripening process [134]. Figure B.6c,d show the porous Pd anode morphology after 2h fuel cell testing with ethanol fuel. The morphological change is much severe as spreading of Pd particles on BZY surface and droplet-like agglomeration of Pd are observed in addition to cluster mergence. The agglomerated particles are in the dimension of ∼200 nm. The severe spreading and agglomeration of Pd are attributed to the electrochemical reaction taken place in the free-standing membrane area as the porous Pd on the side wall of Si wells, which only plays a role of current conduction, still maintains its porous structure with only thermally agglomeration of the cluster. No visually carbon deposition was detected both on the reaction membrane and side wall Pd, which can also be identified from the high resolution XPS spectra of C 1s, as shown in Figure B.7. The deconvolution revealed that all the samples shows similar carbon component with a small amount of increase at 286.5 eV after fuel cell test with ethanol.

As the first attempt to direct utilize ethanol as a fuel for μ-SOFC with proton-conducting electrolyte, we utilize standard porous Pt films as the cathode and Pd anode for the demonstration. It is reported that metallic binary or ternary catalysts show promising catalytic activity toward ethanol oxidation with respect

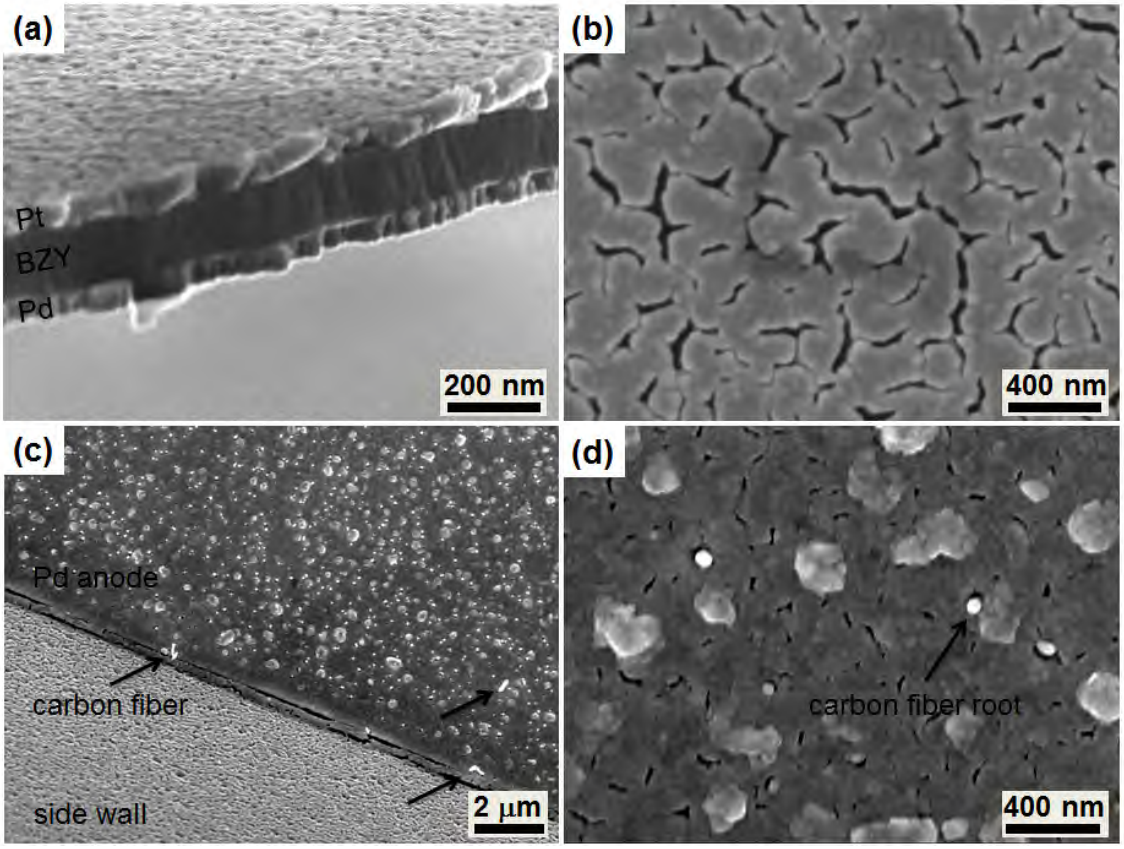

FIGURE B.6: FESEM characterization of Pt/BZY/Pd μ-SOFC after fuel cell test. (a) Cross-sectional view of Pt/BZY/Pd heterostructure after testing with hydrogen; (b) Pd anode morphology after hydrogen fuel test; (c) Pd anode morphology after ethanol fuel test; (d) Enlarged view of Pd anode in the free-standing membrane region of (c)

to metallic anode alone due to the bi-functional effect and the electronic interaction between metal and alloyed metals [119]. We expect an enhanced fuel cell performance by using metallic alloyed anode materials in our future work.

B.4 Summary

Direct ethanol cell with nanoscale proton-conducting ceramic electrolyte has been fabricated and demonstrated. Highly crystallized BZY thin film electrolyte has been achieved with PLD deposition at high temperature of 800 °C. Nanoporous

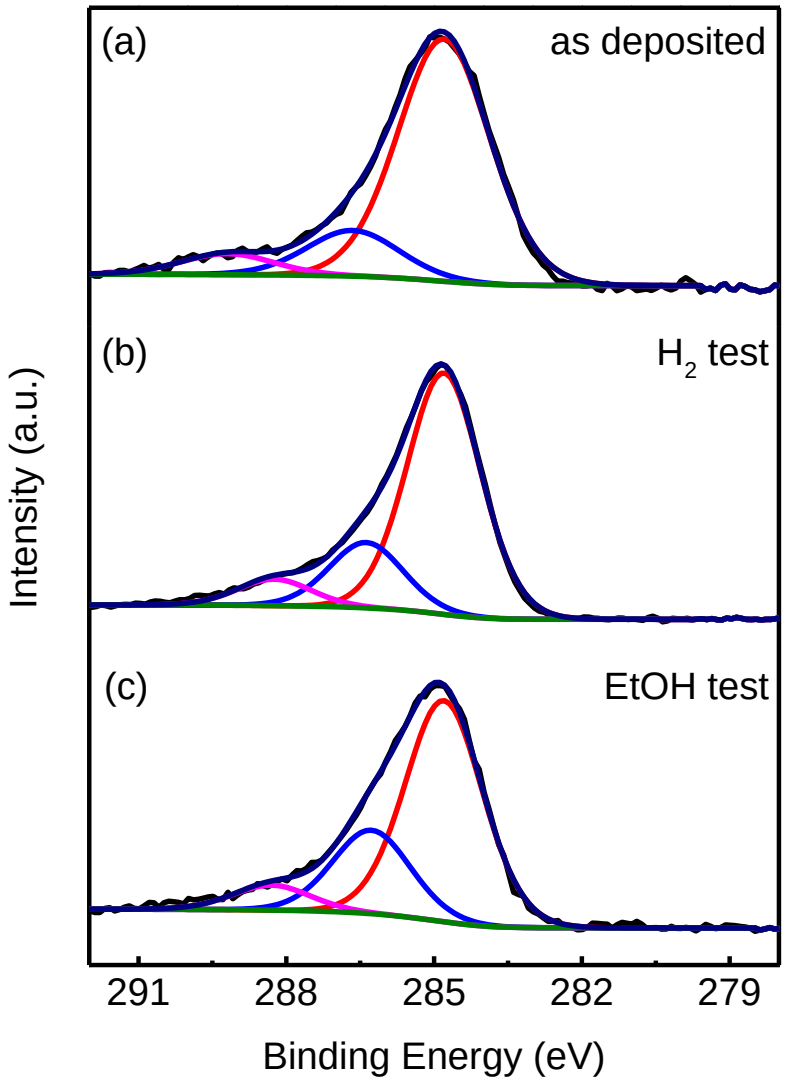

FIGURE B.7: High resolution XPS spectra of C 1s recorded from Pd anode. (a) as deposited; (b) after fuel cell test with H_2 fuel; and (c) after fuel cell test with ethanol fuel.

Pd anode film was synthesized by controlling the DC sputtering pressure to 80 mTorr. The heterostructured proton-conducting μ-SOFC exhibits a peak power density of 72.4 and 15.3 mW/cm^2 with hydrogen and ethanol as the fuel at low operating temperature of 400 °C. The morphology of Pd anodes after hydrogen and ethanol fuel operation showed distinct difference. Due to the complexity of ethanol oxidation, the morphology of Pd anode have experienced sever agglomeration and

carbon deposition. The results presented in this work have demonstrated the feasibility of direct utilization of ethanol fuel for μ-SOFC operation, which could be promising power source for portable electronic devices.

Bibliography

[1] D. W. Ball, *Beginning Chemistry*, 2012.

[2] Wikipedia, "Solid oxide fuel cell," accessed on 28-Dec-2015. [Online]. Available: https://en.wikipedia.org/wiki/Solid_oxide_fuel_cell

[3] A. Evans, A. Bieberle-Htter, J. L. M. Rupp, and L. J. Gauckler, "Review on microfabricated micro-solid oxide fuel cell membranes," *Journal of Power Sources*, vol. 194, no. 1, pp. 119–129, 2009.

[4] K. D. Kreuer, "Proton-conductingoxides," *Annual Review of Materials Research*, vol. 33, no. 1, pp. 333–359, 2003.

[5] T. Hibino, A. Hashimoto, M. Suzuki, and M. Sano, "Proton Conduction at the Surface of Y-Doped $BaCeO_3$," *The Journal of Physical Chemistry B*, vol. 105, no. 46, pp. 11 399–11 401, 2001.

[6] E. Fabbri, L. Bi, D. Pergolesi, and E. Traversa, "Towards the next generation of solid oxide fuel cells operating below 600 °C with chemically stable proton-conducting electrolytes," *Advanced Materials*, vol. 24, no. 2, pp. 195–208, 2011.

[7] K. Wang, *Advances in Graphene Science*. INTECH, 2013, ch. Laser Based Fabrication of Graphene, pp. 79–95.

[8] B. C. Steele and A. Heinzel, "Materials for fuel-cell technologies," *Nature*, vol. 414, no. 6861, pp. 345–352, 2001.

[9] E. Fabbri, D. Pergolesi, and E. Traversa, "Materials challenges toward proton-conducting oxide fuel cells: a critical review," *Chem Soc Rev*, vol. 39, no. 11, pp. 4355–4369, 2010.

[10] H. Huang, M. Nakamura, P. C. Su, R. Fasching, Y. Saito, and F. B. Prinz, "High-performance ultrathin solid oxide fuel cells for low-temperature operation," *Journal of the Electrochemical Society*, vol. 154, no. 1, pp. B20–B24, 2007.

[11] J. An, Y.-B. Kim, J. Park, T. M. Gr, and F. B. Prinz, "Three-Dimensional Nanostructured Bilayer Solid Oxide Fuel Cell with 1.3 W/cm^2 at 450 °C," *Nano Letters*, vol. 13, no. 9, pp. 4551–4555, 2013.

[12] C. Chan, "The state of the art of electric, hybrid, and fuel cell vehicles," *Proceedings of the IEEE*, vol. 95, no. 4, pp. 704–718, 2007.

[13] J. A. Turner, "A realizable renewable energy future," *Science*, vol. 285, no. 5428, pp. 687–689, 1999.

[14] L. Yang, "New materials for intermediate-temperature solid oxide fuel cells to be powered by carbon-and sulfur-containing fuels," Ph.D. dissertation, Georgia Institute of Technology, 2011.

[15] I. EG&G Technical Services, *Fuel Cell Handbook (Seventh Edition).* U.S. Department of Energy, 2004.

[16] V. S. Bagotsky, *Fuel cells: problems and solutions.* John Wiley & Sons, 2012, vol. 56.

[17] A. Atkinson, S. Skinner, and J. Kilner, "Solid oxide fuel cells (sofc)," in *Encyclopedia of Sustainability Science and Technology*, R. Meyers, Ed. Springer New York, 2012, pp. 9885–9904.

[18] J. Larminie, A. Dicks, and M. S. McDonald, *Fuel cell systems explained.* Wiley New York, 2003, vol. 2.

[19] D. J. L. Brett, A. Atkinson, N. P. Brandon, and S. J. Skinner, "Intermediate temperature solid oxide fuel cells," *Chemical Society Reviews*, vol. 37, no. 8, pp. 1568–1578, 2008.

[20] E. V. Tsipis and V. V. Kharton, "Electrode materials and reaction mechanisms in solid oxide fuel cells: A brief review. III. Recent trends and selected methodological aspects," *Journal of Solid State Electrochemistry*, vol. 15, no. 5, pp. 1007–1040, 2011.

[21] B. C. H. Steele, "Ceramic ion conducting membranes," *Current Opinion in Solid State and Materials Science*, vol. 1, no. 5, pp. 684–691, 1996.

[22] K. D. Kreuer, S. Adams, W. Mnch, A. Fuchs, U. Klock, and J. Maier, "Proton conducting alkaline earth zirconates and titanates for high drain electrochemical applications," *Solid State Ionics*, vol. 145, no. 14, pp. 295–306, 2001.

[23] H. Iwahara, "High temperature proton conducting oxides and their applications to solid electrolyte fuel cells and steam electrolyzer for hydrogen production," *Solid State Ionics*, vol. 28, pp. 573–578, 1988.

[24] S. M. Haile, "Fuel cell materials and components," *Acta Materialia*, vol. 51, no. 19, pp. 5981–6000, 2003.

[25] J. W. Fergus, "Electrolytes for solid oxide fuel cells," *Journal of Power Sources*, vol. 162, no. 1, pp. 30–40, 2006.

[26] H. Iwahara, H. Uchida, K. Morimoto, and S. Hosogi, "High-temperature C1-gas fuel cells using proton-conducting solid electrolytes," *Journal of Applied Electrochemistry*, vol. 19, no. 3, pp. 448–452, 1989.

[27] H. Uchida, H. Yoshikawa, T. Esaka, S. Ohtsu, and H. Iwahara, "Formation of protons in $SrCeO_3$-based proton conducting oxides. Part II. Evaluation of proton concentration and mobility in Yb-doped $SrCeO_3$," *Solid State Ionics*, vol. 36, no. 1, pp. 89–95, 1989.

[28] M. Iijima, N. Ito, S. Matsumoto, and S. Iguchi, "Cell Performance Stability of HMFC using $Ba(Ce_{1-x}Zr_x)_{0.8}Y_{0.2}O_3$ Perovskite Type Proton Conductor as Electrolyte," *MRS Proceedings*, vol. 972, 2007.

[29] N. Ito, M. Iijima, K. Kimura, and S. Iguchi, "New intermediate temperature fuel cell with ultra-thin proton conductor electrolyte," *Journal of Power Sources*, vol. 152, pp. 200–203, 2005.

[30] C. W. Tanner and A. V. Virkar, "Instability of $BaCeO_3$ in H_2O-Containing atmospheres," *Journal of the Electrochemical Society*, vol. 143, no. 4, pp. 1386–1389, 1996.

[31] Y. Yamazaki, R. Hernandez-Sanchez, and S. M. Haile, "High Total Proton Conductivity in Large-Grained Yttrium-Doped Barium Zirconate," *Chemistry of Materials*, vol. 21, no. 13, pp. 2755–2762, 2009.

[32] V. Esposito and E. Traversa, "Design of Electroceramics for Solid Oxides Fuel Cell Applications: Playing with Ceria," *Journal of the American Ceramic Society*, vol. 91, no. 4, pp. 1037–1051, 2008.

[33] T. Ishihara, T. Shibayama, M. Honda, H. Nishiguchi, and Y. Takita, "Intermediate temperature solid oxide fuel cells using $LaGaO_3$ electrolyte II. Improvement of oxide ion conductivity and power density by doping Fe for Ga site of $LaGaO_3$," *Journal of the electrochemical society*, vol. 147, no. 4, pp. 1332–1337, 2000.

[34] O. H. Kwon and G. M. Choi, "Electrical conductivity of thick film YSZ," *Solid State Ionics*, vol. 177, no. 3536, pp. 3057–3062, 2006.

[35] Y. B. Kim, T. M. Gur, H. J. Jung, S. Kang, R. Sinclair, and F. B. Prinz, "Effect of crystallinity on proton conductivity in yttrium-doped barium zirconate thin films," *Solid State Ionics*, vol. 198, no. 1, pp. 39–46, 2011.

[36] W. Zajc, D. Rusinek, K. Zheng, and J. Molenda, "Applicability of Gd-doped $BaZrO_3$, $SrZrO_3$, $BaCeO_3$ and $SrCeO_3$ proton conducting perovskites as electrolytes for solid oxide fuel cells," *Central European Journal of Chemistry*, vol. 11, no. 4, pp. 471–484, 2012.

[37] J. H. Shim, T. M. Gur, and F. B. Prinz, "Proton Conduction in Thin Film Yttrium-doped Barium Zirconate," *Applied Physics Letters*, vol. 92, no. 25, p. 253115, 2008.

[38] D. Pergolesi, E. Fabbri, A. DEpifanio, E. Di Bartolomeo, A. Tebano, S. Sanna, S. Licoccia, G. Balestrino, and E. Traversa, "High proton conduction in grain-boundary-free yttrium-doped barium zirconate films grown by pulsed laser deposition," *Nat Mater*, vol. 9, no. 10, pp. 846–852, 2010.

[39] W. Sun, M. Liu, and W. Liu, "Chemically stable yttrium and tin co-doped barium zirconate electrolyte for next generation high performance proton-conducting solid oxide fuel cells," *Advanced Energy Materials*, vol. 3, no. 8, pp. 1041–1050, 2013.

[40] C. Zuo, S. Zha, M. Liu, M. Hatano, and M. Uchiyama, "$Ba(Zr_{0.1}Ce_{0.7}Y_{0.2})O_{3-\delta}$ as an Electrolyte for Low-Temperature Solid-Oxide Fuel Cells," *Advanced Materials*, vol. 18, no. 24, pp. 3318–3320, 2006.

[41] J. H. Shim, J. S. Park, J. An, T. M. Gr, S. Kang, and F. B. Prinz, "Intermediate-Temperature Ceramic Fuel Cells with Thin Film Yttrium-Doped Barium Zirconate Electrolytes," *Chemistry of Materials*, vol. 21, no. 14, pp. 3290–3296, 2009.

[42] I. Chang, P. Heo, and S. W. Cha, "Thin film solid oxide fuel cell using a pinhole-free and dense Y-doped $BaZrO_3$," *Thin Solid Films*, vol. 534, pp. 286–290, 2013.

[43] S. Ji, I. Chang, Y. H. Lee, M. H. Lee, and S. W. Cha, "Performance enhancement of thin-film ceramic electrolyte fuel cell using bi-layered yttrium-doped barium zirconate," *Thin Solid Films*, vol. 539, pp. 117–121, 2013.

[44] P.-C. Su and F. B. Prinz, "Cup-shaped yttria-doped barium zirconate membrane fuel cell array," *Microelectronic Engineering*, vol. 88, no. 8, pp. 2405–2407, 2011.

[45] Y. B. Kim, T. M. Gr, S. Kang, H.-J. Jung, R. Sinclair, and F. B. Prinz, "Crater patterned 3-D proton conducting ceramic fuel cell architecture with ultra thin Y:$BaZrO_3$ electrolyte," *Electrochemistry Communications*, vol. 13, no. 5, pp. 403–406, 2011.

[46] S. Ha, P.-C. Su, S. Ji, and S. W. Cha, "Low temperature solid oxide fuel cells with proton-conducting Y:$BaZrO_3$ electrolyte on porous anodic aluminum oxide substrate," *Thin Solid Films*, vol. 544, pp. 125–128, 2013.

[47] Y. Li, P.-C. Su, L. M. Wong, and S. Wang, "Chemical stability study of nanoscale thin film yttria-doped barium cerate electrolyte for micro solid oxide fuel cells," *Journal of Power Sources*, vol. 268, pp. 804–809, 2014.

[48] K. Bae, D. Y. Jang, H. J. Jung, J. W. Kim, J.-W. Son, and J. H. Shim, "Micro ceramic fuel cells with multilayered yttrium-doped barium cerate and zirconate thin film electrolytes," *Journal of Power Sources*, vol. 248, pp. 1163–1169, 2014.

[49] S. Kang, P. Heo, Y. H. Lee, J. Ha, I. Chang, and S.-W. Cha, "Low intermediate temperature ceramic fuel cell with Y-doped $BaZrO_3$ electrolyte and thin film Pd anode on porous substrate," *Electrochemistry Communications*, vol. 13, no. 4, pp. 374–377, 2011.

[50] J. Park, J. Y. Paek, I. Chang, S. Ji, S. W. Cha, and S. I. Oh, "Pulsed laser deposition of Y-doped $BaZrO_3$ thin film as electrolyte for low temperature solid oxide fuel cells," *CIRP Annals - Manufacturing Technology*, vol. 62, no. 1, pp. 563–566, 2013.

[51] S. Adam and S. Ramanathan, "Proton Conducting Micro-Solid Oxide Fuel Cells with Nanoscale Palladium Interlayers," *ECS Transactions*, vol. 69, no. 16, pp. 23–27, 2015.

[52] R. Kannan, K. Singh, S. Gill, T. Furstenhaupt, and V. Thangadurai, "Chemically Stable Proton Conducting Doped $BaCeO_3$ - No More Fear to SOFC Wastes," *Sci Rep*, vol. 3, p. 2138, 2013.

[53] E. Fabbri, A. Depifanio, E. Dibartolomeo, S. Licoccia, and E. Traversa, "Tailoring the chemical stability of $Ba(Ce_{0.8-x}Zr_x)Y_{0.2}O_{3-\delta}$ protonic conductors for Intermediate Temperature Solid Oxide Fuel Cells (IT-SOFCs)," *Solid State Ionics*, vol. 179, no. 15-16, pp. 558–564, 2008.

[54] S. V. Bhide and A. V. Virkar, "Stability of $BaCeO_3$-Based Proton Conductors in Water Containing Atmospheres," *Journal of the Electrochemical Society*, vol. 146, no. 6, pp. 2038–2044, 1999.

[55] K. Takeuchi, C. K. Loong, J. W. Richardson, J. Guan, S. E. Dorris, and U. Balachandran, "The crystal structures and phase transitions in Y-doped $BaCeO_3$: their dependence on Y concentration and hydrogen doping," *Solid State Ionics*, vol. 138, no. 1-2, pp. 63–77, 2000.

[56] E. Fabbri, D. Pergolesi, A. D'Epifanio, E. Di Bartolomeo, G. Balestrino, S. Licoccia, and E. Traversa, "Design and fabrication of a chemically-stable proton conductor bilayer electrolyte for intermediate temperature solid oxide fuel cells (IT-SOFCs)," *Energy & Environmental Science*, vol. 1, no. 3, p. 355, 2008.

[57] L. Bi, S. Q. Zhang, L. Zhang, Z. T. Tao, H. Q. Wang, and W. Liu, "Indium as an ideal functional dopant for a proton-conducting solid oxide fuel cell," *International Journal of Hydrogen Energy*, vol. 34, no. 5, pp. 2421–2425, 2009.

[58] K. Xie, R. Q. Yan, X. R. Chen, D. H. Dong, S. L. Wang, X. Q. Liu, and G. Y. Meng, "A new stable $BaCeO_3$-based proton conductor for intermediate-temperature solid oxide fuel cells," *Journal of Alloys and Compounds*, vol. 472, no. 1-2, pp. 551–555, 2009.

[59] J. M. Serra and W. A. Meulenberg, "Thin-film proton $BaZr_{0.85}Y_{0.15}O_3$ conducting electrolytes: Toward an intermediate-temperature solid oxide fuel

cell alternative," *Journal of the American Ceramic Society*, vol. 90, no. 7, pp. 2082–2089, 2007.

[60] Z. T. Tao, Z. W. Zhu, H. Q. Wang, and W. Liu, "A stable $BaCeO_3$-based proton conductor for intermediate-temperature solid oxide fuel cells," *Journal of Power Sources*, vol. 195, no. 11, pp. 3481–3484, 2010.

[61] J. Dauter, N. Maffei, S. S. Bhella, and V. Thangadurai, "Studies on chemical stability and electrical properties of proton conducting perovskite-like doped $BaCeO_3$," *Journal of The Electrochemical Society*, vol. 157, no. 10, pp. B1413–B1418, 2010.

[62] Y. Takagi, B. K. Lai, K. Kerman, and S. Ramanathan, "Low temperature thin film solid oxide fuel cells with nanoporous ruthenium anodes for direct methane operation," *Energy & Environmental Science*, vol. 4, no. 9, pp. 3473–3478, 2011.

[63] K. Kerman, B. K. Lai, and S. Ramanathan, "Thin film nanocrystalline $Ba_{0.5}Sr_{0.5}Co_{0.8}Fe_{0.2}O_3$: Synthesis, conductivity, and micro-solid oxide fuel cells," *Journal of Power Sources*, vol. 196, no. 15, pp. 6214–6218, 2011.

[64] Y. Takagi, K. Kerman, C. Ko, and S. Ramanathan, "Operational characteristics of thin film solid oxide fuel cells with ruthenium anode in natural gas," *Journal of Power Sources*, 2013.

[65] L. L. Jiang, X. G. Tang, S. J. Kuang, and H. F. Xiong, "Surface chemical states of barium zirconate titanate thin films prepared by chemical solution deposition," *Applied Surface Science*, vol. 255, no. 21, pp. 8913–8916, 2009.

[66] A. V. Fetisov, G. A. Kozhina, S. K. Estemirova, V. B. Fetisov, V. Y. Mitrofanov, S. A. Uporov, and L. B. Vedmid, "XPS Study of Mechanically Activated $YBa_2Cu_3O_{6+\delta}$ and $NdBa_2Cu_3O_{6+\delta}$," *Journal of Spectroscopy*, vol. 2013, pp. 1–13, 2013.

[67] S. M. Haile, G. Staneff, and K. H. Ryu, "Non-stoichiometry, grain boundary transport and chemical stability of proton conducting perovskites," *Journal of Materials Science*, vol. 36, no. 5, pp. 1149–1160, 2001.

[68] A. Trovarelli, G. Dolcetti, C. Deleitenburg, J. Kaspar, P. Finetti, and A. Santoni, "Rh-CeO_2 Interaction Induced by High-Temperature Reduction - Characterization and Catalytic Behavior in Transient and Continuous Conditions," *Journal of the Chemical Society-Faraday Transactions*, vol. 88, no. 9, pp. 1311–1319, 1992.

[69] J. Li, U. G. Singh, J. W. Bennett, K. Page, J. C. Weaver, J.-P. Zhang, T. Proffen, A. M. Rappe, S. Scott, and R. Seshadri, "$BaCe_{1-x}Pd_xO_{3-\delta}$ ($0 \leq x \leq 0.1$): Redox Controlled Ingress and Egress of Palladium in a Perovskite," *Chemistry of Materials*, vol. 19, no. 6, pp. 1418–1426, 2007.

[70] P. Burroughs, A. Hamnett, A. F. Orchard, and G. Thornton, "Satellite structure in the X-ray photoelectron spectra of some binary and mixed oxides of lanthanum and cerium," *Journal of the Chemical Society, Dalton Transactions*, no. 17, p. 1686, 1976.

[71] E. Bche, P. Charvin, D. Perarnau, S. Abanades, and G. Flamant, "Ce 3d XPS investigation of cerium oxides and mixed cerium oxide (CexTiyOz)," *Surface and Interface Analysis*, vol. 40, no. 3-4, pp. 264–267, 2008.

[72] M. Romeo, K. Bak, J. Elfallah, F. Lenormand, and L. Hilaire, "XPS Study of the Reduction of Cerium Dioxide," *Surface and Interface Analysis*, vol. 20, no. 6, pp. 508–512, 1993.

[73] E. Paparazzo and G. M. Ingo, "On the X-ray induced chemical reduction of CeO_2 as seen with X-ray photoemission spectroscopy," *Journal of Electron Spectroscopy and Related Phenomena*, vol. 95, no. 2-3, pp. 301–304, 1998.

[74] T.-N. Lin, M.-C. Lee, R.-J. Yang, J.-C. Chang, W.-X. Kao, and L.-S. Lee, "Chemical state identification of Ce^{3+}/Ce^{4+} in the $Sm_{0.2}Ce_{0.8}O_{2-\delta}$ electrolyte for an anode-supported solid oxide fuel cell after long-term operation," *Materials Letters*, vol. 81, pp. 185–188, 2012.

[75] H. J. Ko, J. J. Lee, and S.-H. Hyun, "Structural Stability of GDC Electrolyte for Low-Temperature SOFCs Depending on Fuels," *Electrochemical and Solid State Letters*, pp. 1611–1616, 2009.

[76] T. Otake, H. Yugami, H. Naito, K. Kawamura, T. Kawada, and J. Mizusaki, "Ce^{3+} concentration in ZrO_2-$CeO_2Y_2O_3$ system studied by electronic Raman scattering," *Solid State Ionics*, vol. 135, no. 14, pp. 663–667, 2000.

[77] M. Mogensen, N. M. Sammes, and G. A. Tompsett, "Physical, chemical and electrochemical properties of pure and doped ceria," *Solid State Ionics*, vol. 129, no. 1-4, pp. 63–94, 2000.

[78] M. Chen, B. H. Kim, Q. Xu, B. K. Ahn, W. J. Kang, and D. P. Huang, "Synthesis and electrical properties of $Ce_{0.8}Sm_{0.2}O_{1.9}$ ceramics for IT-SOFC electrolytes by urea-combustion technique," *Ceramics International*, vol. 35, no. 4, pp. 1335–1343, 2009.

[79] J. H. Shim, C.-C. Chao, H. Huang, and F. B. Prinz, "Atomic Layer Deposition of Yttria-Stabilized Zirconia for Solid Oxide Fuel Cells," *Chemistry of Materials*, vol. 19, no. 15, pp. 3850–3854, 2007.

[80] P.-C. Su, C.-C. Chao, J. H. Shim, R. Fasching, and F. B. Prinz, "Solid oxide fuel cell with corrugated thin film electrolyte," *Nano Letters*, vol. 8, no. 8, pp. 2289–2292, 2008.

[81] J. D. Baek, Y.-J. Yoon, W. Lee, and P.-C. Su, "A circular membrane for nano thin film micro solid oxide fuel cells with enhanced mechanical stability," *Energy Environ. Sci.*, vol. 8, no. 11, pp. 3374–3380, 2015.

[82] L. Fan and P. C. Su, "Layer-Structured $LiNi_{0.8}Co_{0.2}O_2$: A New Triple ($H^+/O^{2-}/e^-$) Conducting Cathode for Low Temperature Proton Conducting Solid Oxide Fuel Cells," *Journal of Power Sources*, vol. 306, p. 369, 2016.

[83] J. Kim, S. Sengodan, G. Kwon, D. Ding, J. Shin, M. Liu, and G. Kim, "Triple-conducting layered perovskites as cathode materials for proton-conducting solid oxide fuel cells," *ChemSusChem*, vol. 7, no. 10, pp. 2811–5, 2014.

[84] W. Sun, S. Fang, L. Yan, and W. Liu, "Proton-blocking composite cathode for proton-conducting solid oxide fuel cell," *Journal of The Electrochemical Society*, vol. 158, no. 11, p. B1432, 2011.

[85] C. C. Duan, J. H. Tong, M. Shang, S. Nikodemski, M. Sanders, S. Ricote, A. Almansoori, and R. O'Hayre, "Readily processed protonic ceramic fuel cells with high performance at low temperatures," *Science*, vol. 349, no. 6254, pp. 1321–1326, 2015.

[86] R. Peng, T. Wu, W. Liu, X. Liu, and G. Meng, "Cathode processes and materials for solid oxide fuel cells with proton conductors as electrolytes," *Journal of Materials Chemistry*, vol. 20, no. 30, p. 6218, 2010.

[87] Z. Fan, J. W. An, A. Iancu, and F. B. Prinz, "Thickness effects of yttria-doped ceria interlayers on solid oxide fuel cells," *Journal of Power Sources*, vol. 218, pp. 187–191, 2012.

[88] A. Marizy, P. Roussel, A. Ringued, and M. Cassir, "Atomic layer deposition of epitaxial CeO_2 thin layers for faster surface hydrogen oxidation and faster bulk ceria reduction/reoxidation," *J. Mater. Chem. A*, vol. 3, no. 19, pp. 10 498–10 503, 2015.

[89] B. C. H. Steele, "Interfacial reactions associated with ceramic ion-transport membranes," *Solid State Ionics*, vol. 75, pp. 157–165, 1995.

[90] T. Tsai and S. A. Barnett, "Increased solid-oxide fuel cell power density using interfacial ceria layers," *Solid State Ionics*, vol. 98, no. 3-4, pp. 191–196, 1997.

[91] Y. B. Kim, T. P. Holme, T. M. Gur, and F. B. Prinz, "Surface-Modified Low-Temperature Solid Oxide Fuel Cell," *Advanced Functional Materials*, vol. 21, no. 24, pp. 4684–4690, 2011.

[92] D. Prez-Coll, D. Marrero-Lpez, P. Nez, S. Piol, and J. R. Frade, "Grain boundary conductivity of $Ce_{0.8}Ln_{0.2}O_{2-\delta}$ ceramics (Ln=Y, La, Gd, Sm) with and without Co-doping," *Electrochimica Acta*, vol. 51, no. 28, pp. 6463–6469, 2006.

[93] T. S. Oh, D. A. Boyd, D. G. Goodwin, and S. M. Haile, "Proton conductivity of columnar ceria thin-films grown by chemical vapor deposition," *Phys Chem Chem Phys*, vol. 15, no. 7, pp. 2466–72, 2013.

[94] M. Shirpour, G. Gregori, R. Merkle, and J. Maier, "On the proton conductivity in pure and gadolinium doped nanocrystalline cerium oxide," *Phys Chem Chem Phys*, vol. 13, no. 3, pp. 937–40, 2011.

[95] B. Zhu, I. Albinsson, and B. E. Mellander, "Electrical properties and proton conduction of gadolinium doped ceria," *Ionics*, vol. 4, no. 3-4, pp. 261–266, 1998.

[96] B. Zhu, I. Albinsson, and B.-E. Mellander, "Impedance spectroscopy study of gadolinia-doped ceria," *Ionics*, vol. 5, no. 3-4, pp. 286–291, 1999.

[97] A. Yan, V. Maragou, A. Arico, M. Cheng, and P. Tsiakaras, "Investigation of a $Ba_{0.5}Sr_{0.5}Co_{0.8}Fe_{0.2}O_{3-\delta}$ based cathode SOFC: II. The effect of CO_2 on the chemical stability," *Applied Catalysis B: Environmental*, vol. 76, no. 34, pp. 320–327, 2007.

[98] Y. J. Leng, S. H. Chan, K. A. Khor, and S. P. Jiang, "Performance evaluation of anode-supported solid oxide fuel cells with thin film YSZ electrolyte," *International Journal of Hydrogen Energy*, vol. 29, no. 10, pp. 1025–1033, 2004.

[99] T. Park, Y. H. Lee, G. Y. Cho, S. Ji, J. Park, I. Chang, and S. W. Cha, "Effect of the thickness of sputtered gadolinia-doped ceria as a cathodic interlayer in solid oxide fuel cells," *Thin Solid Films*, vol. 584, pp. 120–124, 2015.

[100] S. Ji, Y. H. Lee, T. Park, G. Y. Cho, S. Noh, Y. Lee, M. Kim, S. Ha, J. An, and S. W. Cha, "Doped ceria anode interlayer for low-temperature solid oxide fuel cells with nanothin electrolyte," *Thin Solid Films*, vol. 591, pp. 250–254, 2015.

[101] W. Lee, H. J. Jung, M. H. Lee, Y.-B. Kim, J. S. Park, R. Sinclair, and F. B. Prinz, "Oxygen surface exchange at grain boundaries of oxide ion conductors," *Advanced Functional Materials*, vol. 22, no. 5, pp. 965–971, 2012.

[102] E. Fabbri, A. Magras, and D. Pergolesi, "Low-temperature solid-oxide fuel cells based on proton-conducting electrolytes," *MRS Bulletin*, vol. 39, pp. 792–797, 9 2014.

[103] K. Kerman, B.-K. Lai, and S. Ramanathan, "Pt/$Y_{0.16}Zr_{0.84}O_{1.92}$/Pt thin film solid oxide fuel cells: Electrode microstructure and stability considerations," *Journal of Power Sources*, vol. 196, no. 5, pp. 2608–2614, 2011.

[104] M. Tsuchiya, B. K. Lai, and S. Ramanathan, "Scalable nanostructured membranes for solid-oxide fuel cells," *Nat Nanotechnol*, vol. 6, no. 5, pp. 282–6, 2011.

[105] S. Ha, P.-C. Su, and S.-W. Cha, "Combinatorial deposition of a dense nanothin film ysz electrolyte for low temperature solid oxide fuel cells," *Journal of Materials Chemistry A*, vol. 1, no. 34, p. 9645, 2013.

[106] H. Jung, K. Bae, D. Y. Jang, Y. H. Lee, S.-W. Cha, and J. H. Shim, "Evaluation of porous platinum, nickel, and lanthanum strontium cobaltite as electrode materials for low-temperature solid oxide fuel cells," *International Journal of Hydrogen Energy*, vol. 39, no. 31, pp. 17 828–17 835, 2014.

[107] Y. Matsuzaki, "Electrochemical properties of reduced-temperature SOFCs with mixed ionicelectronic conductors in electrodes and/or interlayers," *Solid State Ionics*, vol. 152-153, pp. 463–468, 2002.

[108] Q. L. Liu, K. A. Khor, and S. H. Chan, "High-performance low-temperature solid oxide fuel cell with novel BSCF cathode," *Journal of Power Sources*, vol. 161, no. 1, pp. 123–128, 2006.

[109] W. Zhou, R. Ran, and Z. Shao, "Progress in understanding and development of $Ba_{0.5}Sr_{0.5}Co_{0.8}Fe_{0.2}O_{3-\delta}$-based cathodes for intermediate-temperature solid-oxide fuel cells: A review," *Journal of Power Sources*, vol. 192, no. 2, pp. 231–246, 2009.

[110] C. C. Yu, S. Kim, J. D. Baek, Y. Li, P. C. Su, and T. S. Kim, "Direct observation of nanoscale pt electrode agglomeration at the triple phase boundary," *ACS Appl Mater Interfaces*, vol. 7, no. 11, pp. 6036–40, 2015.

[111] J. H. Noh, J. H. Park, H. S. Han, D. H. Kim, B. S. Han, S. Lee, J. Y. Kim, H. S. Jung, and K. S. Hong, "Aligned photoelectrodes with large surface area prepared by pulsed laser deposition," *The Journal of Physical Chemistry C*, vol. 116, no. 14, pp. 8102–8110, 2012.

[112] A. Evans, J. Martynczuk, D. Stender, C. W. Schneider, T. Lippert, and M. Prestat, "Low-Temperature Micro-Solid Oxide Fuel Cells with Partially Amorphous $La_{0.6}Sr_{0.4}CoO_{3-\delta}$ Cathodes," *Advanced Energy Materials*, vol. 5, no. 1, p. 1400747, 2015.

[113] S. Lee, N. Miller, M. Staruch, K. Gerdes, M. Jain, and A. Manivannan, "$Pr_{0.6}Sr_{0.4}CoO_{3-\delta}$ electrocatalyst for solid oxide fuel cell cathode introduced via infiltration," *Electrochimica Acta*, vol. 56, no. 27, pp. 9904–9909, 2011.

[114] C. Fu, K. Sun, N. Zhang, X. Chen, and D. Zhou, "Electrochemical characteristics of LSCF-SDC composite cathode for intermediate temperature SOFC," *Electrochimica Acta*, vol. 52, no. 13, pp. 4589–4594, 2007.

[115] Y. Yang, W. Zhou, R. Liu, M. Li, T. E. Rufford, and Z. Zhu, "In Situ Tetraethoxysilane-Templated Porous $Ba_{0.5}Sr_{0.5}Co_{0.8}Fe_{0.2}O_{3-\delta}$Perovskite for the Oxygen Evolution Reaction," *ChemElectroChem*, vol. 2, no. 2, pp. 200–203, 2015.

[116] T. Montini, M. Bevilacqua, E. Fonda, M. F. Casula, S. Lee, C. Tavagnacco, R. J. Gorte, and P. Fornasiero, "Relationship between Electrical Behavior and Structural Characteristics in Sr-Doped $LaNi_{0.6}Fe_{0.4}O_{3-\delta}$ Mixed Oxides," *Chemistry of Materials*, vol. 21, no. 8, pp. 1768–1774, 2009.

[117] M. Ning, Y. Y. Mi, C. K. Ong, P. C. Lim, and S. J. Wang, "Growth studies of (220), (200) and (111) oriented MgO films on Si (001) without buffer layer," *Journal of Physics D: Applied Physics*, vol. 40, no. 12, pp. 3678–3682, 2007.

[118] J. W. Schwank and A. R. Tadd, "Catalytic reforming of liquid hydrocarbons for on-board solid oxide fuel cell auxiliary power units," *Catalysis*, vol. 22, pp. 56–93, 2010.

[119] E. Antolini, "Catalysts for direct ethanol fuel cells," *Journal of Power Sources*, vol. 170, no. 1, pp. 1–12, 2007.

[120] M. Z. F. Kamarudin, S. K. Kamarudin, M. S. Masdar, and W. R. W. Daud, "Review: Direct ethanol fuel cells," *International Journal of Hydrogen Energy*, vol. 38, no. 22, pp. 9438–9453, 2013.

[121] J. J. Linares, T. A. Rocha, S. Zignani, V. A. Paganin, and E. R. Gonzalez, "Different anode catalyst for high temperature polybenzimidazole-based direct ethanol fuel cells," *International Journal of Hydrogen Energy*, vol. 38, no. 1, pp. 620–630, 2013.

[122] J. Lobato, P. Caizares, D. Ubeda, F. J. Pinar, and M. A. Rodrigo, "Testing PtRu/CNF catalysts for a high temperature polybenzimidazole-based direct ethanol fuel cell. Effect of metal content," *Applied Catalysis B: Environmental*, 2011.

[123] D. D. James and P. G. Pickup, "Effects of crossover on product yields measured for direct ethanol fuel cells," *Electrochimica Acta*, vol. 55, no. 11, pp. 3824–3829, 2010.

[124] S. Kontou, V. Stergiopoulos, S. Song, and P. Tsiakaras, "Ethanol/water mixture permeation through a nafion based membrane electrode assembly," *Journal of Power Sources*, vol. 171, no. 1, pp. 1–7, 2007.

[125] E. D. Wachsman and K. T. Lee, "Lowering the temperature of solid oxide fuel cells," *Science*, vol. 334, no. 6058, pp. 935–939, 2011.

[126] C. Bianchini and P. K. Shen, "Palladium-based electrocatalysts for alcohol oxidation in half cells and in direct alcohol fuel cells," *Chem Rev*, vol. 109, no. 9, pp. 4183–206, 2009.

[127] L. Adijanto, A. Sampath, A. S. Yu, M. Cargnello, P. Fornasiero, R. J. Gorte, and J. M. Vohs, "Synthesis and Stability of Pd@CeO_2 CoreShell Catalyst Films in Solid Oxide Fuel Cell Anodes," *ACS Catalysis*, vol. 3, no. 8, pp. 1801–1809, 2013.

[128] A. Babaei, L. Zhang, E. Liu, and S. P. Jiang, "Performance and Carbon Deposition over Pd Nanoparticle Catalyst Promoted Ni/GDC Anode of SOFCs in Methane, Methanol and Ethanol Fuels," *International Journal of Hydrogen Energy*, vol. 37, no. 20, pp. 15 301–15 310, 2012.

[129] S. P. S. Badwal, S. Giddey, A. Kulkarni, J. Goel, and S. Basu, "Direct ethanol fuel cells for transport and stationary applications a comprehensive review," *Applied Energy*, vol. 145, pp. 80–103, 2015.

[130] B.-K. Lai, K. Kerman, and S. Ramanathan, "Methane-fueled thin film micro-solid oxide fuel cells with nanoporous palladium anodes," *Journal of Power Sources*, vol. 196, no. 15, pp. 6299–6304, 2011.

[131] Anon., "Platinum 2008 Interim Review," *Platinum Metals Review*, vol. 53, no. 1, pp. 48–49, 2009.

[132] J. S. Park, Y. B. Kim, J. H. Shim, S. Kang, T. M. Gr, and F. B. Prinz, "Evidence of Proton Transport in Atomic Layer Deposited Yttria-Stabilized Zirconia Films," *Chemistry of Materials*, vol. 22, no. 18, pp. 5366–5370, 2010.

[133] M. Cimenti and J. M. Hill, "Direct utilization of ethanol on ceria-based anodes for solid oxide fuel cells," *Asia-Pacific Journal of Chemical Engineering*, vol. 4, no. 1, pp. 45–54, 2009.

[134] X. H. Wang, H. Huang, T. Holme, X. Tian, and F. B. Prinz, "Thermal stabilities of nanoporous metallic electrodes at elevated temperatures," *Journal of Power Sources*, vol. 175, no. 1, pp. 75–81, 2008.

Publication List

Journal Papers

1. **Li Y**, Wang S-J, Su P-C, Proton-conducting micro solid oxide fuel cells with improved cathode reactions by a nanoscale thin film gadolinium-doped ceria interlayer. ***Scientific Reports***. 2016;6:22369

2. Yu C-C, Kim S, Baek JD, **Li Y**, Su P-C, Kim T-S. Direct Observation of Nanoscale Pt Electrode Agglomeration at the Triple Phase Boundary. ***ACS Applied Materials & Interfaces***. 2015;7(11):6036-40.

3. **Li Y**, Su P-C, Wong LM, Wang S. Chemical stability study of nanoscale thin film yttria-doped barium cerate electrolyte for micro solid oxide fuel cells. ***Journal of Power Sources***. 2014;268:804-9.

4. **Li Y**, Wong LM, Yu C-C, Wang S-J, Su P-C, Nanostructured $Ba_{0.5}Sr_{0.5}Co_{0.8}Fe_{0.2}O_{3-\delta}$ Thin Film Cathode for Low Temperature Solid Oxide Fuel Cells (under review)

5. **Li Y**, Su, P-C, Direct Ethanol Solid Oxide Fuel Cells with Nanoscale Proton-conducting Ceramic Electrolyte (in preparation)

Conference Presentations

1. **Li Y**, Su P-C, Wang SJ, Proton-conducting micro solid oxide fuel cells with cerium based ceramic electrolytes, Scientific Advances in Fuel Cells 2014, 3-4 April,

2014, Amsterdam, The Netherlands

2. **Li Y**, Su P-C, Wong LM, Wang SJ, High performance proton-conducting micro solid oxide fuel cells, 3rd Asia-Korea Conference on Science and Technology, Nov 21-23, 2013, Singapore

3. **Li Y**, Su P-C, Wong LM, Wang SJ, Crystallinity Dependent Proton Conductivity in Y-BaZrO3 Thin Film for Low-Temperature Solid Oxide Fuel Cell, ICMAT 2013, 30 Jun - 5 July, 2013, Singapore

4. Ha S, **Li Y**, Baek JD, Su P-C, Direct Ethanol Fuel Cells with Nanoscale Proton-conducting Ceramic Electrolyte, 2012 MRS Fall Meeting & Exhibit, Nov 25-30, 2012, Boston, Massachusetts